MAGNETOHYDRODYNAMICS OF MAGNETARS' HIGH-ENERGY AND RADIO EMISSIONS: A SIMULATION STUDY

by

Riddhi Mehta

A Dissertation

Submitted to the Faculty of Purdue University

In Partial Fulfillment of the Requirements for the degree of

Doctor of Philosophy

Department of Physics and Astronomy

West Lafayette, Indiana

May 2021

THE PURDUE UNIVERSITY GRADUATE SCHOOL
STATEMENT OF COMMITTEE APPROVAL

Dr. Maxim Lyutikov, Chair

Department of Physics and Astronomy

Dr. Andrew Hirsch

Department of Physics and Astronomy

Dr. Dimitrios Giannios

Department of Physics and Astronomy

Dr. Danny Milisavljevic

Department of Physics and Astronomy

Approved by:

Dr. John Finley

TABLE OF CONTENTS

LIST OF FIGURES

ABSTRACT

This article-based dissertation provides a review on the broad subject of magnetars - their characteristics, giant flares (GFs) and associated observations of X-ray, γ-ray, and radio emissions and their proposed physical mechanisms. The primary purpose of this dissertation is to provide an extensive description of the two research projects I undertook during my tenure as a Graduate Research Assistant, under the guidance of my advisor. Broadly, my research was focused on building analytical models and running three-dimensional (3-D), high-resolution magnetohydrodynamic (MHD) simulations using the astrophysical *PLUTO* code to investigate the physical mechanisms behind high-energy (X-ray and γ-ray) and radio emissions associated with magnetar GFs using observational constraints. This, in turn, aided in either validating or disfavoring existing theories behind such energetic explosions.

Chapter 1 provides a review on magnetars, their GFs and associated high-energy and radio emissions, largely based on excellent reviews by [1]–[5]. I summarize interesting observational features of magnetars, specifically those of soft gamma-ray repeaters (SGRs) and anomalous X-ray pulsars (AXPs), along with known aspects of their X-ray and γ-ray activity. I focus on the December 27, 2004 GF emitted by SGR 1806-20, the most energetic GF out of the three that occurred to date, describe its energetics and summarize existing theories behind the physical mechanisms that give rise to two emission characteristics associated with the GF - (i) quasi-periodic oscillations (QPOs) seen in the tail, and (ii) a radio afterglow detected a week after the GF. Lastly, I describe the methods I used to hypothesize the physical mechanisms behind QPOs and the radio emission and compare and contrast them with those suggested previously.

In chapter 2, I present a version of the research article in preparation and pending publication in the *Monthly Notices of the Royal Astronomical Society*. The work titled *"Radio afterglow of magnetars' giant flares"*, undertaken under the supervision of Dr. Maxim Lyutikov and in collaboration with Dr. Maxim Barkov, explores the possible physical mechanisms behind the radio afterglow associated with the SGR 1806-20 GF using high-resolution 3-D MHD simulations.

In chapter 3, I present a version of the research article previously published by the *Journal of Plasma Physics*. The work titled *"Tilting instability of magnetically confined spheromaks"*, undertaken under the supervision of Dr. Maxim Lyutikov, in collaboration with Dr. Lorenzo Sironi and Dr. Maxim Barkov, investigates the tilting instability of a magnetically confined spheromak using 3-D MHD and relativistic particle-in-cell (PIC) simulations with an application to astrophysical plasmas, specifically to explain the QPOs arising in the tail of the SGR 1806-20 GF.

I summarize the main results and conclusions of the two research projects and describe future prospects in chapter 4, followed by appendices A and B which describe additional theoretical concepts and simulation results for a better understanding of the nature of radio afterglows associated with GFs, and structure of spheromaks. References are compiled after the appendices in order that they are first cited, followed by a brief autobiographical sketch, and a list of publications.

1. INTRODUCTION

In this chapter, I give an overview of some of the distinguishing features of magnetars and their X-ray and γ-ray emissions as well as the radio afterglow associated with the most energetic GF to date, emitted by SGR 1806-20. Reviews on magnetars and their emissions by [1]–[5] immensely aided in compiling this chapter.

1.1 A brief review on magnetars and their high-energy (X-ray and γ-ray) emissions

Magnetars are young ($\sim 10^3 - 10^4$ years) and highly magnetized (surface magnetic fields $\sim 10^{14} - 10^{15}$ G) neutron stars and serve to be unique laboratories to probe current physical theories like General Relativity owing to the combination of extreme magnetic fields, gravity, and density. Their dramatic X-ray and γ-ray activity ranging from few millisecond bursts to major month-long outbursts, GFs and QPOs is explained by the magnetar model which attributes the powering of high-energy emission to the dissipation and decay of ultra-strong surface magnetic fields and even higher internal fields ($\approx 10^{16}$ G) and hence the term magnetar [6]–[8].

Historically, magnetars were classified under the names of soft gamma repeaters (SGRs) and anomalous X-ray pulsars (AXPs). SGRs were first associated with classical gamma-ray bursts (GRBs) because of detection of short, intense bursts in the hard X-/soft gamma-ray range; however, these SGR bursts were soon recognized to repeat with a softer spectra than those of GRBs, setting the two phenomena apart. On the other hand, AXPs were identified as X-ray pulsars in the soft X-ray range (< 10 keV) and were dubbed 'anomalous' because their high X-ray luminosity ($\sim 10^{34} - 10^{36}\,\mathrm{erg\,s^{-1}}$) cannot be easily reconciled in terms of the conventional processes which apply to other classes of pulsars, i.e. accretion from a binary companion or injection of rotational energy in the pulsar wind/magnetosphere. A crucial suggestion made by [8] that AXPs may be related to SGRs was unambiguously confirmed six years later by the discovery of SGR-like bursts from two AXPs. The main observational characteristics of SGRs and AXPs, apart from their dramatic and frequent X-ray and γ-ray bursting activity (to a lesser extent in AXPs), are: (a) lack of evidence

of binary companions; (b) persistent (i.e. non-bursting), often variable X-ray luminosity in the range $\sim 10^{33} - 10^{36}\,\mathrm{erg\,s^{-1}}$, emitted in the soft (0.5 - 10 keV) and hard (20 - 100 keV) X-ray range; (c) pulsations at relatively long spin periods, clustered in the range $\sim 2 - 12$ s, and (d) large secular spin-down rate $\dot{P} \sim 10^{-13} - 10^{-11}\,\mathrm{s\,s^{-1}}$, which if interpreted in terms of electromagnetic losses from a rotating dipole in vacuo, leads to huge magnetic fields $\sim 10^{14} - 10^{15}$ G [4].

1.2 Magnetars' transient high-energy radiative behavior: bursts, outbursts, giant flares and quasi-periodic oscillations

According to the classification given by [5], the term "bursts" refers to the short, few-millisecond to second events, some of which are followed by longer-lived "tails", an afterglow. The term "outburst" describes sudden but much longer-lived (weeks to months) flux enhancements, which typically involve many of the shorter bursts, and a long (many months) tail or afterglow. The term "giant flares" is reserved exclusively for catastrophic events involving the sudden release of over 10^{44} ergs of energy. QPOs at the spin period of the magnetar have been seen in the tails of some GFs.

Bursts are the most common magnetar radiative events detected from both SGRs and AXPs, with typical duration of $\sim 0.1 - 1$ s, peak X-ray luminosities $\sim 10^{36} - 10^{41}\,\mathrm{erg\,s^{-1}}$ for short bursts and $\sim 1 - 40$ s, peak X-ray luminosities $\sim 10^{41} - 10^{43}\,\mathrm{erg\,s^{-1}}$ for intermediate bursts [4]. [5] describe a GF as the queen of magnetar radiative outbursts with a total energy output $\sim 10^{44} - 10^{47}\,\mathrm{erg\,s^{-1}}$ and the one phenomenon that could in principle distinguish SGRs from AXPs. Three GFs have been recorded to date, all from SGRs alone and one GRB is a possible fourth candidate: March 5, 1979 (SGR 0526-66), August 27, 1998 (SGR 1900+14), December 27, 2004 (SGR 1806-20), and April 15, 2020 (GRB 200415A). All three GFs start with an initial very short and spectrally hard main spike lasting ~ 0.5 s, followed by several minutes long extended softer tail highly modulated at the neutron star's spin period which are called quasi-periodic oscillations (QPOs) and believed to be seismic vibrations of the neutron star. I next discuss the specific case of SGR 1806-20 GF, the most energetic magnetar event to date, the QPOs in its tail, and the radio afterglow recorded seven days after the GF.

1.3 The giant γ-ray flare from SGR 1806-20

I discuss the GF of SGR 1806-20 that occurred on December 27, 2004 [9], [10] and its accompanying QPOs which were first reported by [11]. The total light curve of the flare is shown in figure 1.1, details of which can be studied in [10]. As seen, the bright, main spike lasts ~ 0.5 s and is followed by a ~ 380 s pulsating tail, that is, ~ 50 cycles of high-amplitude pulsations at the SGR's known rotation period of 7.56 s [9]. For a distance to SGR 1806-20 of $15d_{15}$ kpc ($0.8 < d_{15} < 1$ as suggested by [12]), an isotropic equivalent energy release of $2 \times 10^{46} d_{15}^2$ erg in the initial spike and $5 \times 10^{43} d_{15}^2$ erg in the tail is reported by [9]. This isotropic equivalent energy in the initial spike is about two orders of magnitude larger than that in the other two GFs, while the energy in the tail is comparable, an observation attributable to the fact that the tail energies are limited by the storage capacity of the magnetic field and should be as constant from source to source as the field energy, whereas the extent of magnetic reconnection governs the prompt energy release during the main spike which can vary greatly from one event to the next, even within the same source [9].

1.3.1 QPOs in the GF tail

In the context of the magnetar model [7], [10], [11], essentially all the energy release occurs during the initial main ~ 0.2 s transient phase of the GF when a fireball of pair-dominated plasma expands at relativistic speeds, while fraction of the energy deposited in the magnetosphere can form a "trapped fireball" that remains confined to the star's closed magnetic field lines. The long pulsating tails of GFs are believed to arise from the cooling of plasma that remains confined in such a trapped fireball [13]. The magnetic field strength limits the amount of energy that can be confined and the fact that this quantity is similar in the three GFs, despite the much higher total energy release of SGR 1806-20, is consistent with a magnetic field of the same order in the three magnetars. QPOs have also been explained as torsional modes supported by a tangled magnetic field and a model that supports this hypothesis for SGR 1900+14 is suggested by [14] who emphasize that field tangling has important effects that cannot be ignored in the QPO problem.

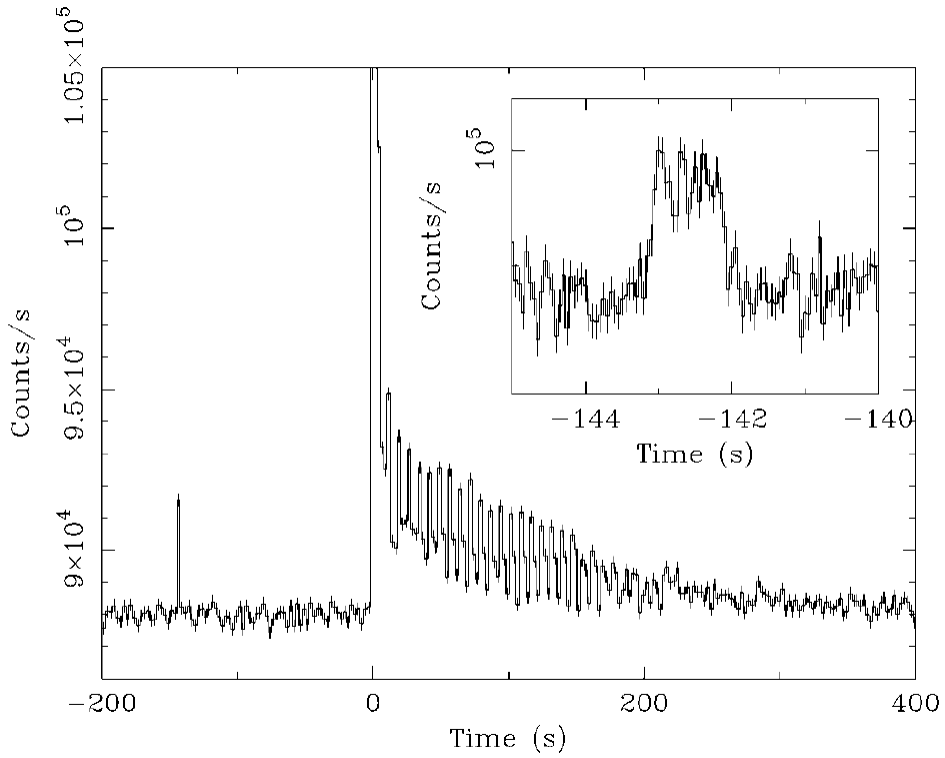

Figure 1.1. Light curve of the whole GF of SGR 1806-20 taken from [10]

The purpose of my first research project was to investigate a possible physical mechanism that could explain these QPOs in the tail of GFs. In chapter 3, I present a version of the published work, describing a model similar to the "trapped plasma fireball" model to explain these QPOs: a magnetically confined spheromak in the magnetar magnetosphere. Through 3-D MHD and PIC simulations, tilting instability of a magnetically confined spheromak is studied and numerical results are applied to astrophysical plasmas like those found in magnetar magnetospheres. Consequently, a disruption timescale of such a spheromak is estimated using the energy constraints of SGR 1806-20 which reveal whether such spheromaks confined in magnetar magnetospheres can be responsible for the tremendous energy release in QPOs over a period of ~ 400 s. Additional details about the structure of spheromaks, their formation and stability will be presented in appendix B.

1.3.2 Radio afterglow associated with the GF

Analysis of a Very Large Array (VLA) observation of SGR 1806-20 about a week after the GF, led to the discovery of a bright radio afterglow as shown in figure 1.2 [15], [16]. Follow-up observations determined that the radio nebula was evolving on short time scales and provided data on the temporal evolution of its size and shape, polarization, and flux. The light curve of the radio emission behaved identically at all observed frequencies [16] and its flux went through multiple phases as shown in figure 1.3, details of which can be referred to in [17]. An interesting feature is seen in the radio light curve starting at $\sim$ 25 days and peaking at $\sim$ 33 days - a rebrightening by a factor of two, followed by a slower decay, $\sim t^{-1.1}$ marking the transition of the radio emission from free expansion to the self-similar Sedov-Taylor phase of its evolution after sweeping up sufficient mass of the ambient medium [18], [19].

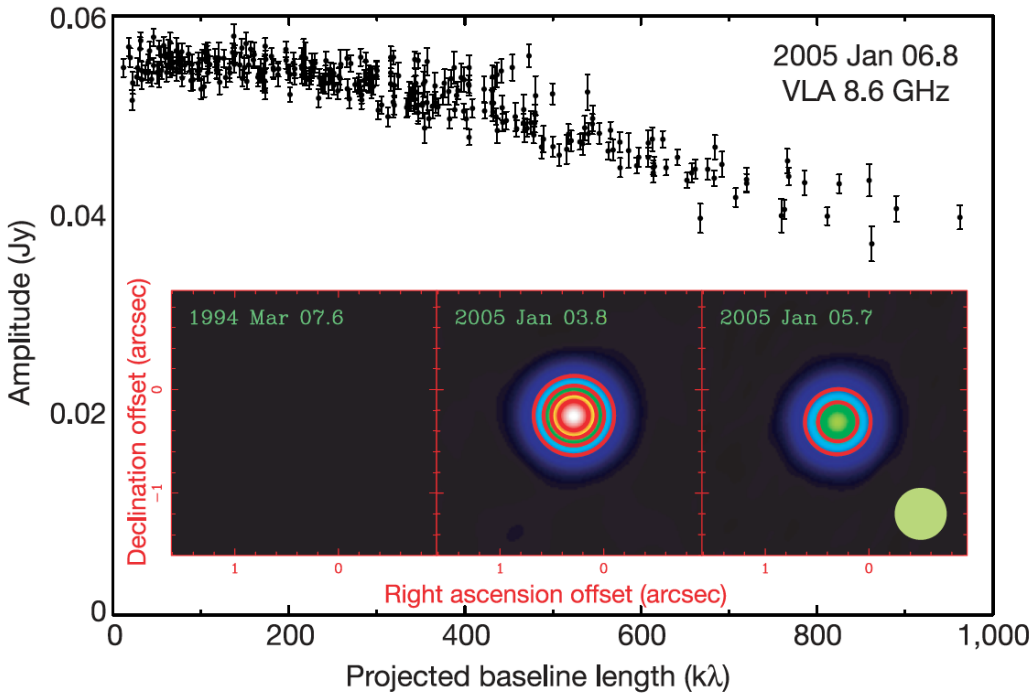

Figure 1.2. Radio emission associated with SGR 1806-20 GF from VLA observation at 8.5 GHz taken from [16]

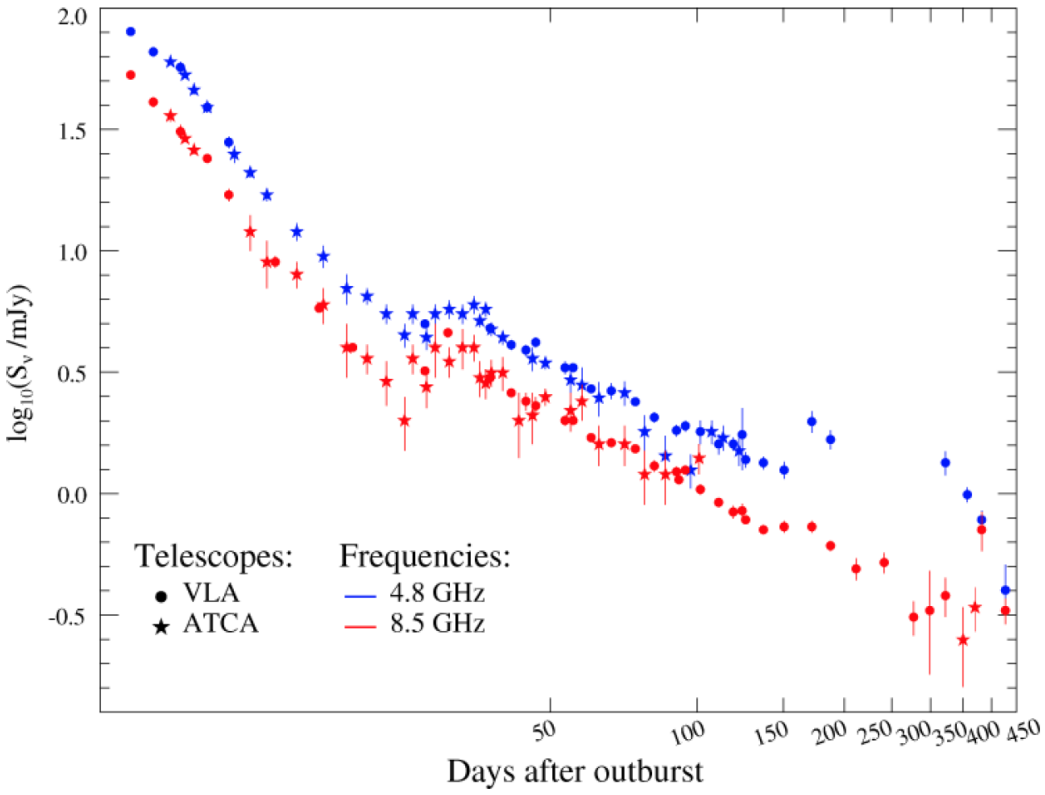

Figure 1.3. Light curve of the radio nebula produced by SGR 1806-20 GF, spanning from 7 to 450 days after the GF taken from [17]

The purpose of my second research project was to investigate a possible physical mechanism for the origin of this radio emission during the GF and a factor-of-two increase in its flux between 25 to 33 days after the GF. In chapter 2, I present a version of the ongoing work, detailing a model for the interaction of the outflow ejected during the SGR 1806-20 GF with its surroundings and deriving synthetic synchrotron emissivity maps through 3-D MHD simulations in order to describe the observed radio emission. Our model considers a light outflow consisting primarily of magnetic fields unlike previous suggestions of a heavy baryon-rich outflow. In particular, we model the outflow as a magnetically confined spheromak-like configuration, an analogue of a Solar Coronal Mass Ejection (CME), details of which will be presented in appendix A.1.

A previously suggested cause for the increase in radio flux is the impact of $\sim 10^{46}$ erg of energy from the SGR's GF on a pre-existing shell surrounding an evacuated cavity, possibly

formed by the interaction of the SGR's quiescent wind with the external medium, and the SGR's supersonic motion relative to the external medium, details of which can be referred to in [18], [19]. A schematic of the model is shown in figure 1.4. Our model, unlike these suggestions, disfavors the requirement of a pre-existing shell to explain the rebrightening in the radio light curve. Details of numerical analysis with a pre-existing shell will be presented in appendix A.2.

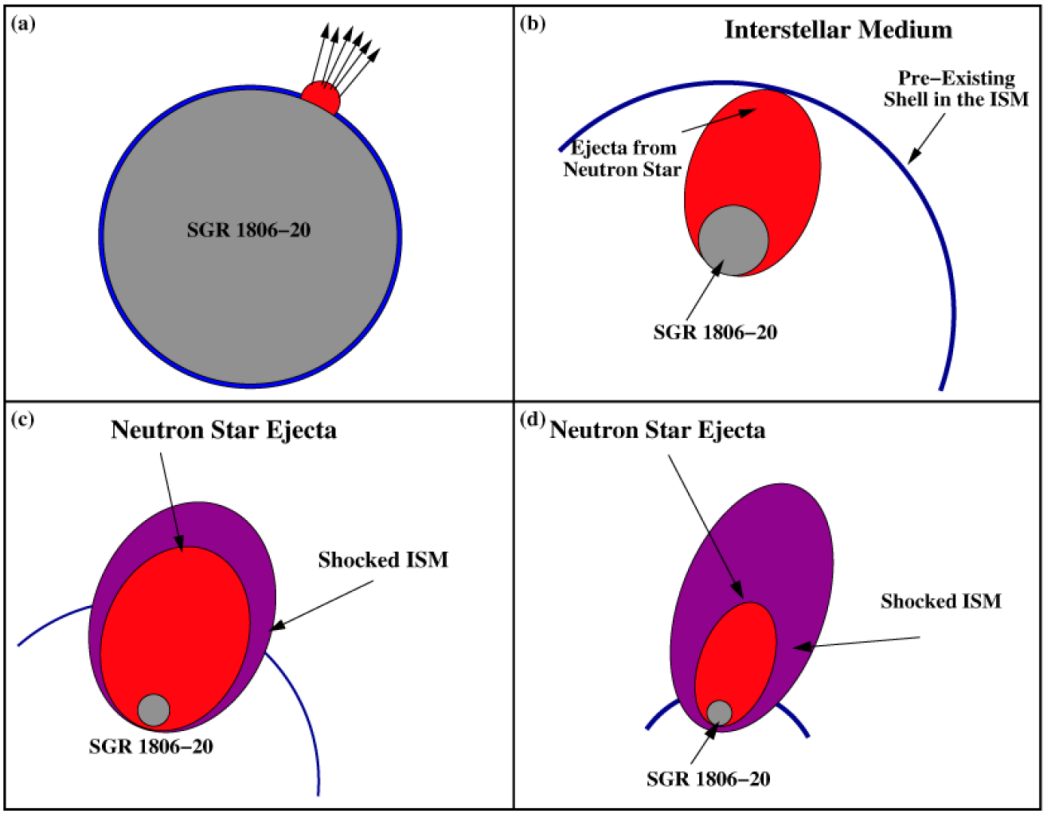

Figure 1.4. Schematic of the dynamical model with a pre-existing shell to explain the observed rebrightening of radio emission associated with the GF from SGR 1806-20 taken from [17]. (a) The ejected baryon-rich material initially expands freely. (b) It then collides with a pre-existing shell in the ISM surrounding the SGR. (c) After collision, the merged shell of shocked ejecta and shocked swept-up external shell continue to expand, sweeping up ISM material. (d) Finally, sufficient mass of the ambient medium is swept up and a spherical self-similar Sedov-Taylor solution is attained.

2. RADIO AFTERGLOW OF MAGNETARS' GIANT FLARES

A version of this chapter is in preparation and pending publication, to be submitted to the *Monthly Notices of the Royal Astronomical Society*. This work is authored by **Mehta, R.** and co-authored by **Barkov, M., & Lyutikov, M.**

This work had been supported by **NASA grants 80NSSC17K0757 and 80NSSC20K0910, NSF grants 10001562 and 10001521**.

We develop a model for the radio afterglow of the giant flare of SGR 1806-20 arising due to the interaction of magnetically dominated cloud ejected from the magnetar, an analogue of Solar Coronal Mass Ejections (CMEs), with the interstellar medium (ISM). The CME is modeled as a spheromak-like configuration. The CME is first advected with the magnetar's wind and later interacts with the ISM, creating a strong forward shock and complicated backwards exhaust flow. Using three-dimensional magnetohydrodynamic simulations, we study various relative configurations of the magnetic field of the CME with respect to the ISM's magnetic field. We show that the dynamics of the forward shock mostly follows the Sedov-Taylor blastwave, while the internal structure of the shocked medium is considerably modified by the back flow, creating a multiple shock configuration. We calculate synthetic synchrotron emissivity maps and light curves using two assumptions: (i) magnetic field compression; (ii) amplification of the magnetic field at the shock. We find that models with magnetic field amplification account better for the observed radio emission.

Key words: magnetohydrodynamics (MHD), stars: magnetars, ISM: supernova remnants

2.1 Introduction

Soft gamma repeaters (SGRs) are a type of slowly spinning neutron stars exhibiting X-ray and γ-ray bursts. Together with Anomalous X-ray pulsars they constitute a class of magnetars [20]. Their emission is powered by the dissipation of magnetic field, that may reach $B \approx 10^{15}$ G. Occasionally, SGRs produce giant flares (GFs); GF from SGR 1806-20 on 27 December 2004 is the most notorious [9], [12]. GFs consist of bright, short initial spike peaking in soft γ-rays (with luminosities reaching 10^{47} ergs/s and duration $\sim$ 100 milli sec), followed by a longer and dimmer tail peaking in hard X-rays modulated by the SGR's rotational period and having luminosities upwards of 10^{44} ergs/s.

A week after the GF of SGR 1806-20, a bright radio afterglow was discovered [15], [16]. The sudden energy release of more than 10^{46} ergs in γ-rays is believed to have ejected a mass of $> 10^{24}$ grams from the neutron star in the form of baryonic material and some magnetic fields [9], [18], [19], [21] and the interaction of this outflow with the external medium is said to have powered the expanding radio nebula. The study of the evolution of the size of the radio nebula and the motion of the flux centroid by [21] reports that it is decelerating and is a one-sided mildly collimated outflow with an initial expansion velocity of $\approx 0.7c$ [19]. Follow-up observations determined that the radio nebula was evolving on short time scales and provided data on the temporal evolution of its size and shape, polarization, and flux. The light curve of the radio emission behaved identically at all observed frequencies [16] and its flux went through multiple phases. The radio flux exhibited a moderate decay, $\sim t^{-1.5}$ to $\sim t^{-2}$ before 9 days after the GF [16] after which it underwent an achromatic steepening, $\sim t^{-2.7}$ between $\sim$ 9 and $\sim$ 25 days [16], [18]. Starting at $\sim$ 25 days and peaking at $\sim$ 33 days, a rebrightening in the radio light curve was observed [18], followed by a slower decay, $\sim t^{-1.1}$.

A possible cause for the increase in radio flux suggested by [16], [17], [19] is the impact of $\sim 10^{46}$ ergs of energy from the SGR's GF on a pre-existing shell surrounding an evacuated cavity. Two possible scenarios have been suggested for the formation of such a shell surrounding a pre-existing cavity. It possibly formed by the interaction of the SGR's quiescent wind with the external medium, and the SGR's supersonic motion relative to the external

medium. Alternatively, it could also have formed from a prior, initially faster mass ejection from the GF, eventually decelerating and causing the two shells to collide. The underlying dynamical model for the one-sided radio emission and its rebrightening proposed by [17], [19] is the following: material from the neutron star was expelled in one preferred direction during the GF and initially expanded freely inside a low-density cavity surrounding the SGR. This ejecta collided with a pre-existing shell in the ISM, after which it continued to expand, sweeping up and shocking the ISM. Eventually, the swept-up material decelerates the ejecta, consequently dominating both the dynamics and emission from the radio nebula. Our model, unlike these suggestions, disfavors the requirement of a pre-existing shell to explain the rebrightening in the radio light curve. Although the existence of a shell produces a break in the light curve, it fails to reproduce any flux increase seen in observations (see appendix A.2).

The afterglow arises due to the interaction of an ejected blob (analogue of a Solar Coronal Mass Ejection, CME) with the surrounding medium. Two contrasting suggestions of the composition of a CME were proposed: matter versus magnetic field-dominated ejections. In the former, the GF was accompanied by an ejection of $> 10^{24}$ grams of baryonic material (about the mass of the Earth; this requires slicing off several meters from the whole surface of a NS) with mildly relativistic velocities [9], [18], [19], [21]. In the latter model ([22], [23], "Solar flare paradigm"), the GF was suggested to have consisted mostly of magnetic fields and some left-over pair plasma, with little baryon loading (so it is not a "mass" ejection in a proper sense). In the "Solar flare paradigm", GFs are magnetospheric events, hence no large baryonic loading is expected.

In this paper, we perform MHD simulations of the interaction of the ejected *magnetically-dominated* CME with the surrounding medium. We outline the numerical set-up in section 2.3, describe results of the MHD simulations in section 2.4, and derive integrated synthetic synchrotron emissivity maps and light curves in section 2.5. Discussion of results and conclusions are presented in section 2.6.

2.2 Magnetar's ejection as an expanding spheromak

2.2.1 Ejected magnetic blob in magnetar wind

In this paper, we perform numerical calculations of radio afterglows of magnetar giant flares, modeled as relativistic magnetized explosions [22]. According to the "The Solar model of magnetars", the explosions are magnetospheric-driven (not crustal driven [20]) events (see also [23], [24]). In the case of magnetospheric release of energy, one does not expect substantial baryonic loading of the expelled fireball. As the magnetic cloud expands, its pair density falls by many orders of magnitude forming light, magnetically dominated blob. Initially, the magnetic cloud is topologically connected to the star, but reconnection at the footprints disconnects it. We expect the blob material to be slightly different from the wind due to pair freeze-out.

Initially, the blob is over-pressurized and has linear momentum implanted during the ejection. The blob propagates in a wind. The pre-explosion wind is expected to accelerate linearly, $\Gamma_w \propto r/R_{LC}$. The over-pressurized blob is also expected to accelerate linearly (similar to fireball model of GRBs [25]). Thus, radial expansion of the blob and the wind are very similar - they virtually do not interact.

The implanted linear momentum changes this picture only slightly: due to relativistic freeze-out in radially accelerated flow, the relative velocity of the blob with respect to the wind quickly becomes non-relativistic. Pressure balance is then established: the blob is frozen into the wind.

The internal structure of the blob frozen into the wind may be approximated as a spheromak: a spherical force-free configuration of linked poloidal and toroidal magnetic fields. As the wind expands and its rest-frame magnetic field decreases, the trapped blob will adjust to the changing confining pressure: the spheromak will expand (in fact, in accelerating flow the spheromak may even become causally disconnected internally). [26] discuss the structure of expanding force-free structures. Expanding spheromak develops internal velocity and currents to compensate for different scalings of toroidal and poloidal components of the magnetic field.

Thus, we expect that by the time the wind starts interacting with the external medium (*e.g.* at the bow-shock [27]), the ejected blob would have expanded to the size of the fraction of the radius. Before interacting with the ISM, the wind passes through the reverse shock. We assume that the blob identity is not destroyed (we *do* see an ejection!). A slightly denser blob will then start interacting with the ISM. Our simulations begin here - figure 2.1.

2.2.2 Magnetic blob - magnetized ISM interaction

We model the interaction of a magnetic blob with the ISM as shown in figure 2.1. Magnetic blob is modeled as a spheromak-like configuration. Spheromaks are simply connected magnetically confined spherical structures which are spontaneously created due to plasma relaxation [28]. A confined classical spheromak requires surface current. In order to avoid complication with internal resistive effects as the spheromak enters the ISM, we use a slightly modified magnetic field structure of [29] with vanishing toroidal and poloidal magnetic fields on the boundary; such a configuration is slightly non-force-free (see appendix A.1).

In our simulations, a spheromak-like magnetic blob (light grey in figure 2.1), embedded within low-density SGR wind, impacts on the ISM (dark grey). Internal magnetic field within the blob may have three generic orientations with respect to the orientation of ISM's uniform magnetic field $B_{\rm ISM}$. The blob's magnetic moment $\mu_{\rm blob}$ can be (i) parallel (ii) anti-parallel (iii) perpendicular to the external field (panel 2.1a). These three configurations are expected to produce somewhat different magnetic interactions between the ISM's and the blob's magnetic fields (see section 2.4.3).

2.3 Three-dimensional MHD Simulations

2.3.1 Numerical set-up

We perform 3-D MHD simulations to study the interaction of the aforementioned magnetic blob moving along with the low-density SGR wind, with an external ISM and consequently describe the radio nebula associated with the 2004 GF. Our aim is to simulate a strong shock (Mach number $\sim 10 - 20$) that would result from the interaction of the fast-moving blob and wind (in the ISM's reference frame) with the ISM with low sound speed.

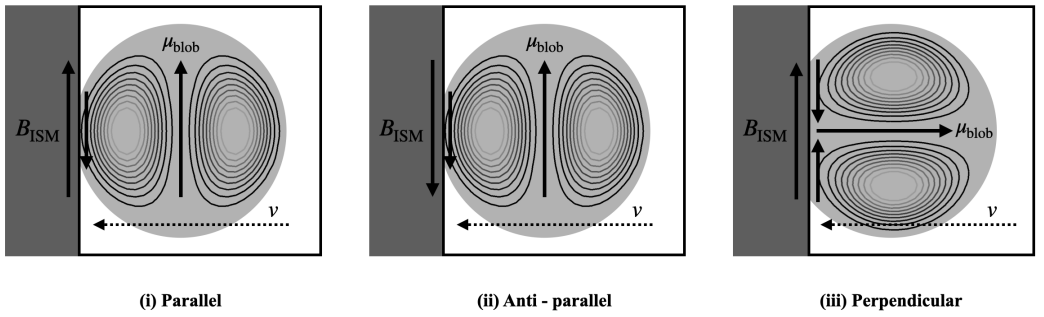

(a)

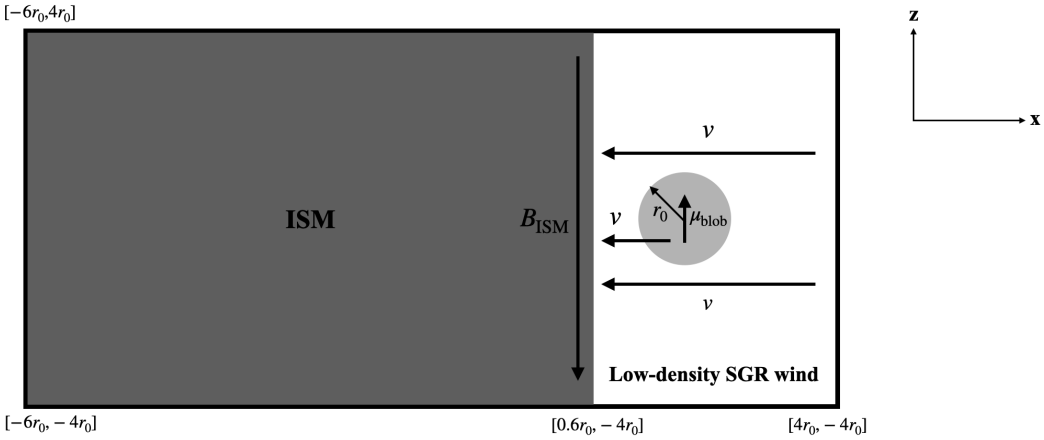

(b)

Figure 2.1. (a) Schematic representation of the set-ups used to analyze interaction of the blob with the ISM with three different orientations. The blob is enlarged to show the concentric flux surfaces that define the magnetic field structure within it. (b) Schematic representation of the anti-parallel set-up used to assess shock properties after the blob-ISM interaction with minimum effects of magnetic reconnection. v is the velocity of the blob and SGR wind moving towards the ISM (see section 2.3.2 for details).

A very strong shock is expected when material and magnetic fields ejected from the SGR's flare hit the ISM with velocity $\sim 0.3c$ as observations suggest. It is the synchrotron emission from this shock that we hypothesize to have been observed as the radio emission and whose properties we wish to analyze for comparison with the observed spectrum.

The simulations are performed using a 3-D Cartesian geometry using the *PLUTO* code[1] [30]. *PLUTO* is a modular Godunov-type code entirely written in C, intended mainly for

[1]↑http://plutocode.ph.unito.it/index.html

astrophysical applications and high Mach number flows in multiple spatial dimensions and designed to integrate a general system of conservation laws

$$\frac{\partial \boldsymbol{U}}{\partial t} = -\nabla.\boldsymbol{T}(\boldsymbol{U}) + \boldsymbol{S}(\boldsymbol{U}) \tag{2.1}$$

$\boldsymbol{U}$ is the vector of conservative variables and $\boldsymbol{T}(\boldsymbol{U})$ is the matrix of fluxes associated with those variables. Our ideal MHD set-up does not use any source terms and $\boldsymbol{U}$ and $\boldsymbol{T}$ are

$$\boldsymbol{U} = \begin{pmatrix} \rho \\ \boldsymbol{m} \\ \boldsymbol{B} \\ E \end{pmatrix}, \boldsymbol{T}(\boldsymbol{U}) = \begin{bmatrix} \rho\boldsymbol{v} \\ \boldsymbol{m}\boldsymbol{v} - \boldsymbol{B}\boldsymbol{B} + p_t\boldsymbol{I} \\ \boldsymbol{v}\boldsymbol{B} - \boldsymbol{B}\boldsymbol{v} \\ (E + p_t)\boldsymbol{v} - (\boldsymbol{v}.\boldsymbol{B})\boldsymbol{B} \end{bmatrix}^{\mathrm{T}} \tag{2.2}$$

$\rho, \boldsymbol{v}$ and p are density, velocity and thermal pressure. $\boldsymbol{m} = \rho\boldsymbol{v}$, $\boldsymbol{B}$ is the magnetic field and $p_t = p + |\boldsymbol{B}|^2/2$ is the total (thermal + magnetic) pressure, respectively. Magnetic field evolution is complemented by the additional constraint $\nabla.\boldsymbol{B} = 0$. Total energy density E

$$E = \frac{p}{\Gamma - 1} + \frac{1}{2}\left(\frac{|\boldsymbol{m}|^2}{\rho} + |\boldsymbol{B}|^2\right) \tag{2.3}$$

along with an isothermal equation of state $p = c_s^2\rho$ provides the closure. Γ and c_s are the polytropic index and isothermal sound speed, respectively. The plasma is approximated as an ideal, non-relativistic adiabatic gas, one particle species with polytropic index of 5/3. *PARABOLIC* interpolation, a third-order Runge-Kutta approximation in time, and a Harten-Lax-Van Leer approximate Riemann solver [31] are used to solve the above ideal MHD equations. Outflow boundary conditions are applied in all three directions.

2.3.2 Physical set-up

We performed a short, low-resolution simulation to resolve the magnetic field structure at early times and assess the effects of current sheet formation and magnetic reconnection when the magnetic blob and low-density SGR wind interact with the ISM with different magnetic field orientations with respect to the blob's magnetic moment μ_{blob}. Panel 2.1a shows a

schematic of the physical set-up with parallel, anti-parallel and perpendicular orientations of $B_{\rm ISM}$ with respect to $\mu_{\rm blob}$. Specifically, we run the parallel and anti-parallel cases to analyze effects of reconnection and expect that the anti-parallel case, where $B_{\rm ISM}$ and magnetic field at the blob's left edge are aligned, would be favorable to minimize reconnection effects and analyze the shock properties to explain the GF's radio emission.

The size of the domain is $x \in [-2.4r_0, 4r_0]$, $y \in [-2.4r_0, 2.4r_0]$ and $z \in [-2.4r_0, 2.4r_0]$ where r_0 is the radius of the blob. Uniform resolution is used throughout the computational domain with total number of cells $N_{\rm X} = N_{\rm Y} = N_{\rm Z} = 256$. The blob's initial magnetic field is defined by A.8, A.9 and A.10. We prefer low plasma-β (high magnetization) of the blob so that effect of magnetic field is captured. These requirements make the following choice of initial parameters justified: an initial velocity of the blob and SGR wind in the negative x direction $\boldsymbol{v} = -100\hat{x}$, ISM pressure $p_{\rm ISM} = 0.5$ and ISM density $\rho_{\rm ISM} = 0.25$ giving the ISM sound speed c_s= 1.82, uniform ISM magnetic field $\boldsymbol{B}_{\rm ISM} = -0.25\hat{z}$, wind pressure $p_{\rm wind} = 0.5$, wind density $\rho_{\rm wind} = 3\times10^{-5}$, $r_0 = 50, \beta = 2$ and blob density $\rho_{\rm blob} = 0.1\rho_{\rm ISM}$. All quantities are given in code units which are normalized *cgs* values

$$\rho = \frac{\rho_{cgs}}{\rho_n}, v = \frac{v_{cgs}}{v_n}, p = \frac{p_{cgs}}{\rho_n v_n^2}, B = \frac{B_{cgs}}{\sqrt{4\pi\rho_n v_n^2}} \tag{2.4}$$

ρ, v, p and B are density, velocity, pressure, and magnetic field. Time is given in units of $t_n = L_n/v_n$. The normalization values used are $\rho_n = 1.67 \times 10^{-24}$gr/cm^3, $L_n = 1.5 \times 10^{13}$ cm and $v_n = 10^5$ cm/s. We describe results of this analysis later in section 2.4.3.

To model the radio emission from the GF, we choose the anti-parallel orientation ((ii) of panel 2.1a), with the ISM magnetic field aligned with the magnetic field at the blob's left edge and capture the shock dynamics arising from the interaction of magnetized blob and low-density SGR wind with external ISM in high resolution for longer times. Cases (i) and (ii) of panel 2.1a evolve almost identically which will be shown in section 2.4.3. A 2-D (xz plane) schematic of the anti-parallel set-up is shown in panel 2.1b. The size of the domain is $x \in [-6r_0, 4r_0]$, $y \in [-4r_0, 4r_0]$ and $z \in [-4r_0, 4r_0]$. Uniform resolution is used throughout the computational domain with total number of cells $N_{\rm X} = N_{\rm Y} = N_{\rm Z} = 780$. The ISM extends from $-6r_0$ to $0.6r_0$ and the low-density cavity extends from $0.6r_0$ to $4r_0$

along the x direction. We center the blob at $[2r_0, 0, 0]$ oriented such that $\mu_{\rm blob}$ and $B_{\rm ISM}$ are anti-parallel. The blob (light grey) is embedded within the SGR's low-density wind and both move towards the stationary ISM (dark grey) with velocity v. The initial parameters of the blob, ISM, and SGR wind and the normalizing values are the same as described above.

2.3.3 Theoretical expectations

The key physical inputs are: a blob (projectile) creates a bulk moving and over-pressurized region (implanted momentum and energy). Both, the implanted momentum and the implanted energy "push" the forward shock (FS). But in contrast to the spherical Sedov explosion (where opposite parts of the flow "push" against each other, thus not conserving the absolute value of momentum), in the case of projectile hitting the ground, energy and momentum can be lost to the backward flow. This energy/momentum loss is complicated: parts of the post-shock flow close to the FS move with nearly the velocity of the FS (3/4 of the shock velocity), and thus with supersonic velocities in the frame of the shell. Further downstream, bulk velocities decrease, become subsonic, and start to "feel" the absence of the back confinement - the resulting high pressure accelerates the flow backwards, toward the wind, forming complicated exhaust flows. Because of high initial pressure, the exhaust flows become supersonic and form a series of shocks.

The implanted momentum and the pressure loss through backward exhaust flow act in the opposite way: implanted momentum increases the FS velocity, while the pressure loss from the bulk drains the energy, and hence leads to the slowing down of the shock.

For the dynamics of the FS, the problem under consideration is somewhat similar to the classical problem of projectile hitting the ground [32], [33]: energy and momentum are implanted. As [32] discuss, the resulting shock dynamics is limited between the two cases of energy and momentum conservation. For pure energy injection with E_0, we expect that the scaling of the shock's radius follows the Sedov solution [34]

$$R_E \sim \left(\frac{E_0 t^2}{\rho}\right)^{1/5} \tag{2.5}$$

For pure momentum injection with $P_0 \sim \sqrt{M_0 E_0}$ (M_0 is the mass of the blob/projectile), we expect that the scaling of the shock's radius follows the Kompaneets solution [35]

$$R_P \sim \left(\frac{P_0 t}{\rho}\right)^{1/4} \tag{2.6}$$

(We stress that the resulting dynamics is not self-similar, but is "bracketed" between these two self-similar solutions). Closeness to any of the above solution depends on the non-dimensionless parameter E_0/P_0, and hence cannot be easily quantified.

Defining Sedov radius and time as

$$R_S = \left(\frac{M_0}{\rho}\right)^{1/3} \tag{2.7}$$

$$t_S = \frac{M_0^{5/6}}{E_0^{1/2}\rho^{1/3}} \tag{2.8}$$

the momentum injection dominates the FS dynamics at times and radii $\leq t_S$, R_S,

$$\frac{R_E}{R_P} = \left(\frac{t}{t_S}\right)^{3/20} \tag{2.9}$$

Though the overall dynamics is not self-similar, we may use the self-similar scalings $p \sim M^{-n} \sim R^{-3n}$ where p is the shock pressure, M is the mass encompassed by the shock wave and R is the shock radius, with an exponent n that may vary in time. Using the time dependences of shock pressure and radius (deduced in section 2.4.1 and figure 2.7), we find $n \approx 1.05$. This exponent value of shock attenuation is in excellent agreement to the proposed range $1 < n < 1.275$ for a self-similar concentrated impact for $\gamma = 5/3$. The lower limit corresponds to an energy conserving shock and the upper limit corresponds to momentum conservation. Thus, the FS's self-similarity is intermediate between energy conserving and momentum conserving regimes. It is important to further note that the concentrated impact is closer to a point explosion in an infinite medium.

2.4 Results

We performed a number of simulations with different resolutions - low (256^3) and high (780^3). In this section, we discuss various, quite complicated aspects of the resulting flow. The salient features are highlighted in figure 2.2, where we plot the z (vertical) component of the velocity at late times, $t = 20$ in code units.

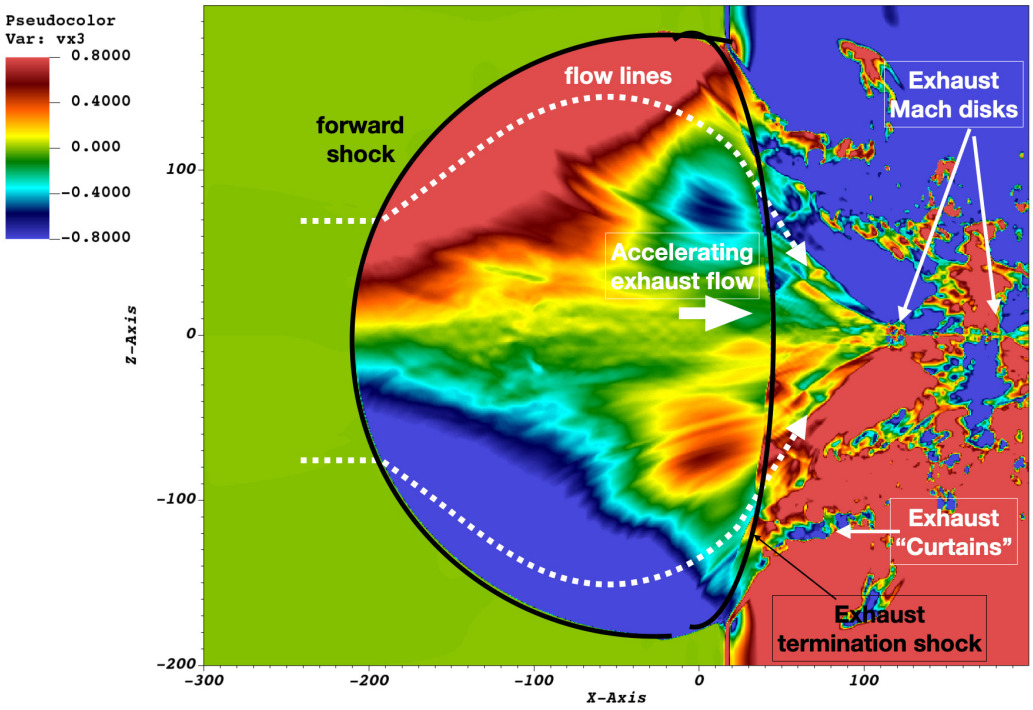

Figure 2.2. Key features of the flow annotated. Plotted is the z (vertical) component of velocity at a fairly advanced time of $t = 20$. Upstream plasma (green color) is stationary. The forward shock (thick black line on the left) is, generally, oblique, inducing post-shock z flow up/down in the upper/lower parts. In the bulk of the shocked material, soon after the FS, the rarefaction wave induces "exhaust flow" towards the back end (large white arrow). The exhaust flow becomes supersonic and terminates at the "exhaust termination shock" (thick black line near $x = 0$). The post-exhaust termination shock flow, collimated towards the symmetry axis, experiences further shocks at "exhaust Mach disks". Near the regions where the forward shock intersects with the boundary, high post-shock pressure launches "exhaust curtains" back in the wind.

The flow is first shocked at the forward shock. This creates a region of high pressure. For spherical explosion, this region of high pressure has only one way to expand - by driving

the FS. In the impact case, there is a second exit: forming a back flow. As a result, the high post-FS pressure is released both, through driving the FS, and through generation of the backward flow.

The overall dynamics of the FS is fairly simple: in the strong shock limit, it approximately follows a self-similar solution, though with not well-defined parameters, bounded by the limits of energy and momentum conservation (section 2.3.3). The back flow is more complicated. As the high post-FS pressure is converted into backward motion, the flow becomes supersonic. As a result, a termination shock forms (back black curve in figure 2.2). At this termination shock the flow is deflected toward the symmetry axis; it overshoots the pressure balance and forms repetitive Mach disks, similar to when a jet air plane flows at low altitudes (when the post-nozzle pressure does not match the ambient pressure).

Additional features appear at the intersection of the FS and the boundary. High post-shock pressure drives an expansion curtain back into the wind, in a way similar to charged explosions hitting the ground, and asteroid impacts [36].

In addition to the hydrodynamically complicated flow, discussed in detail in sections 2.4.1 and 2.4.2, the presence of magnetic field in the blob, and its interaction with the external magnetic field adds few complications to the classical problem of charged projectile impact (section 2.3.3).

In the following discussion, we describe the high-resolution numerical results of the model described in section 2.3.2 and panel 2.1b, namely 2-D slices of pressure, magnetic field, and x component of velocity at $t = 5, 10, 15$ and 20, pressure and velocity profiles of the shock along $z = 0$ at $t = 5, 10, 15$ and 20, as well as, time evolution of pressure and radius of the FS.

2.4.1 Pressure, velocity, and radius of the shock

At $t = 0$, the blob and low-density wind start moving to the left and hit the ISM boundary. This interface between the ISM and cavity wind is where the shock originates and the FS continues to propagate towards the left. We capture the FS until $t = 20$ after which it begins to exit the domain. Figures 2.3-2.6 depict the shock's pressure and x component of velocity

denoted by $vx1$. Figures 2.3 and 2.5 are pressure and $vx1$ projected in 2-D (xz plane) at $t = 5, 10, 15$ and 20 where significant changes to the shock's morphology can be observed. Figures 2.4 and 2.6 are pressure and $vx1$ profiles plotted along $z = 0$ at the same four time instants.

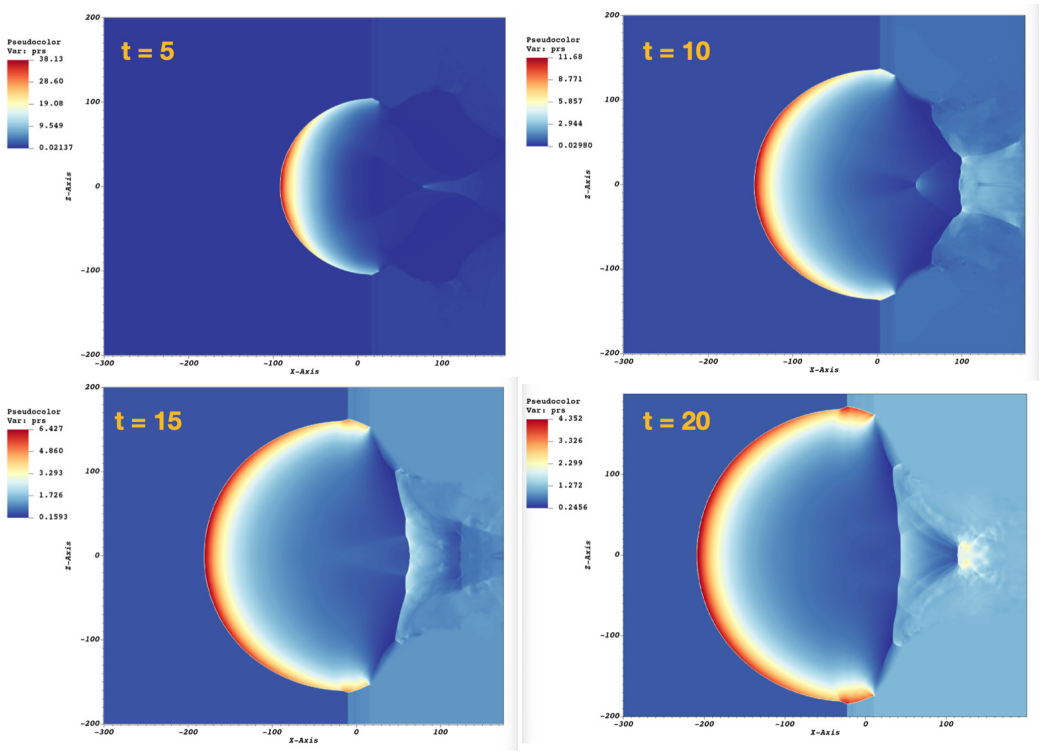

Figure 2.3. Slices in the xz plane of the high-resolution MHD simulation of the interaction of radio blob with external ISM captured at $t = 5, 10, 15$ and 20 in code units. Colors indicate pressure.

At $t = 5$, after initial numerical fluctuations settle, a spherical FS is seen traveling to the left. At the same time, two wing-shaped low-pressure regions develop to the right of the FS into the cavity penetrated by a weak pressure peak just beginning to form. This is the recollimation shock being ejected out of the blob. The pressure depressions can be understood by noticing that at $t = 5$, material behind the FS is being blown to the right with much greater speeds than that of the material moving to the left.

At $t = 10$, as the FS penetrates deeper into the ISM, the recollimation shock is followed by a third pressure bump developing at the edge of the domain. This last shock is a result of

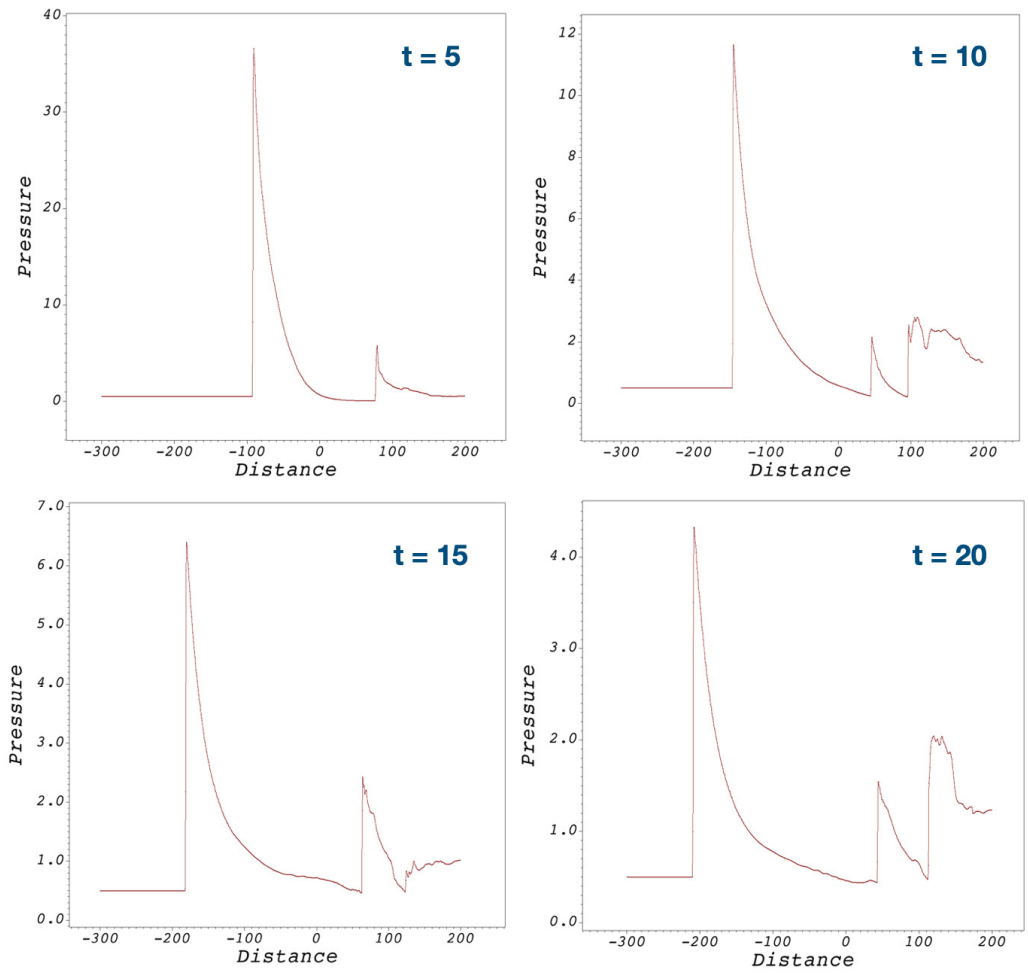

Figure 2.4. Pressure profiles along $z = 0$ plotted at the same four time instants as figure 2.3. At $t = 20$, forward shock to the left, recollimation shock in the middle and "wind" shock to the right are clearly visible. The final stages of shock are dominated by "exhaust flows", weakening the shock by almost 1/9.

external pressure in the wind zone as it thrashes against the recollimation shock and ISM. By this time, the FS is weakened by almost a third due to the strong "exhaust flows" described previously. Direction of moving material within the domain can be seen from its velocity map and profile - FS moving to the left is followed by material moving right. This is followed by a weak recollimation shock and a powerful wind shock moving left at speed greater than the rest of the material.

Final stages of the shock at $t = 15$ and $t = 20$ are dominated by "exhaust" moving to the right at the edge of the domain caused due to reflected pressure waves. The recollimation and

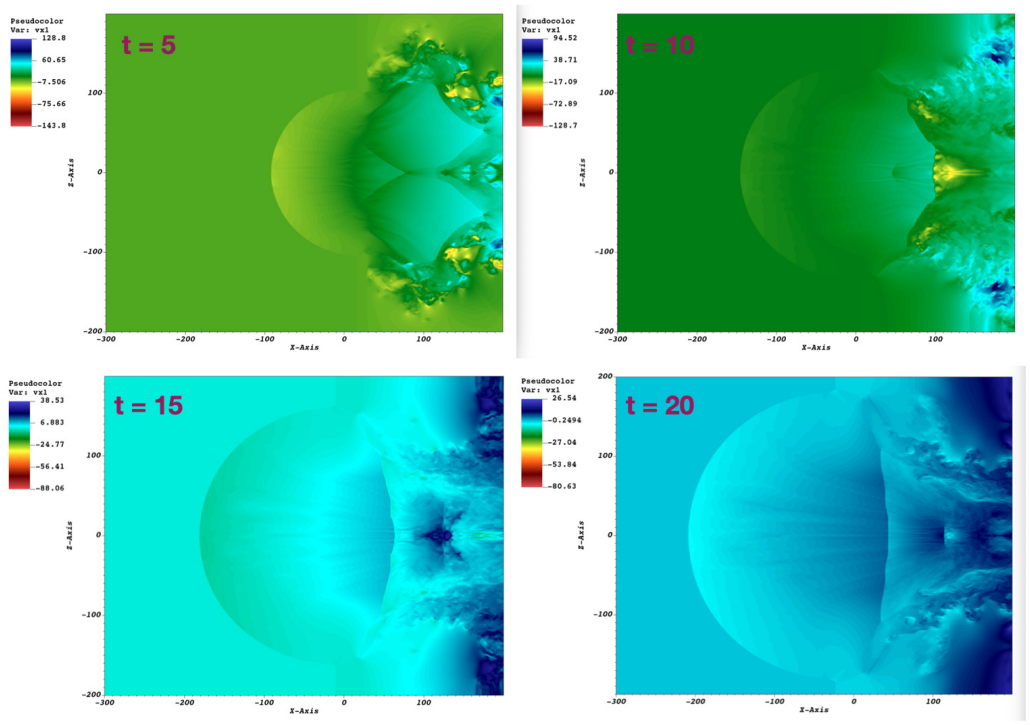

Figure 2.5. Same as figure 2.3 but colors indicate x component of velocity.

wind shocks are stronger but the FS is weakened nine-fold. The concave boundary prominent just to the right of the ISM-cavity interface is formed because material propagating to the right just behind the FS intercepts the wind propagating to the left at greater pressure than the wind's pressure. This exhaust carries away pressure, hence energy from the bulk, thus slowing down the FS (by $\sim 1/2$ from $t = 5$ to $t = 20$) as evident from the $vx1$ map and profile.

Time evolution of pressure and radius of the FS are depicted in figure 2.7. We plot the peak pressure along $z = 0$ and radius of the shock, that is, distance traveled by the point where pressure peaks along $z = 0$, from $t = 5$ to $t = 20$ in steps of 0.5 in log-log scale. A linear fit to the plots gives power laws for both, pressure and radius of the shock: $p(t) \propto t^{-1.52}$ and $R(t) \propto t^{0.48}$.

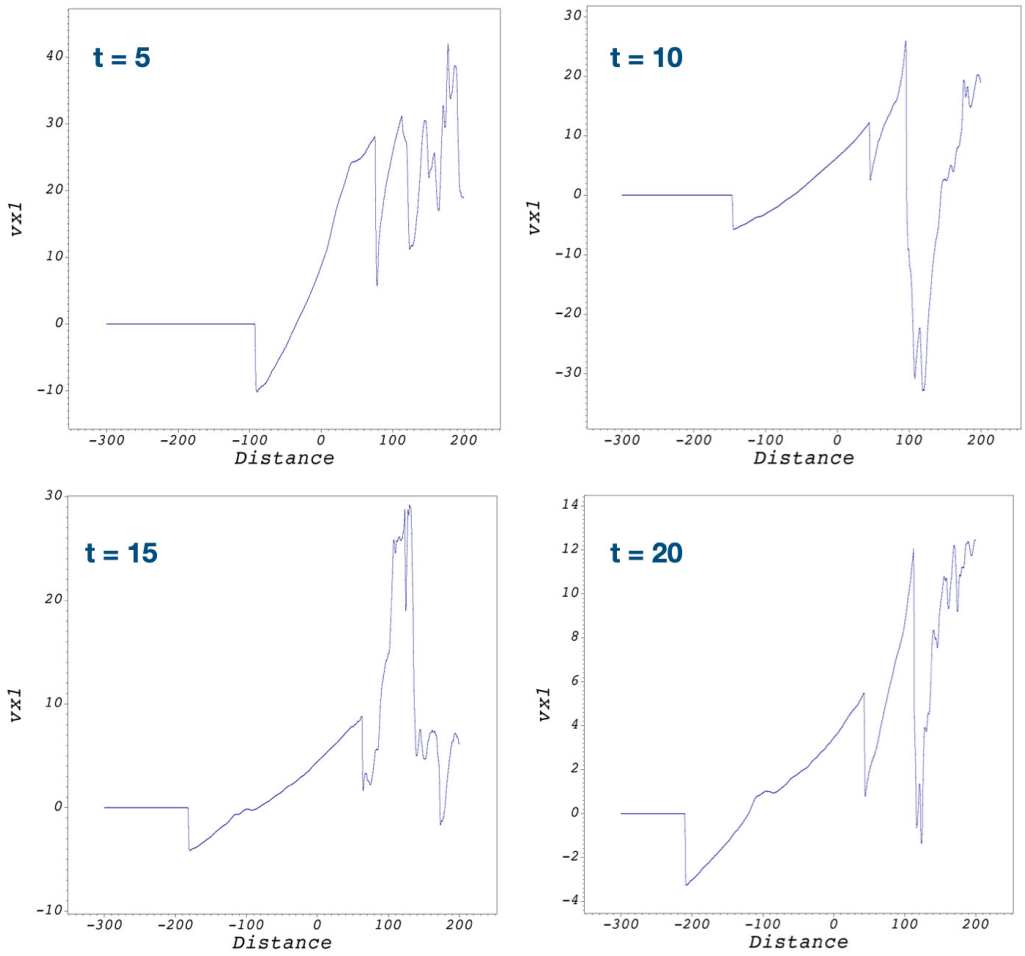

Figure 2.6. $vx1$ profiles plotted along $z = 0$ at the same four time instants as figure 2.3. A significant back flow of material is seen at $t = 5$. At $t = 10$ the "wind" shock moving left pressurizes the recollimation shock. The final stages of shock are dominated by "exhaust flows" exiting the domain.

2.4.2 Properties of the forward shock

Below we show that although the radial dynamics of the FS is approximately self-similar (see figure 2.7), the lateral structure and the internal structures are not.

Using the pressure and magnetic field maps (figures 2.3 and 2.8), we plot the angular variation of pressure and magnetic field of the FS at $t = 10$ and 20 as shown in figure 2.9. θ is the angle in radians, between the x axis and the line joining the center of the shock and the point of peak pressure/magnetic field along the FS when seen along several $z = 0$ cuts in the xz plane. Because the ISM-cavity interface moves with time, the shock center shifts

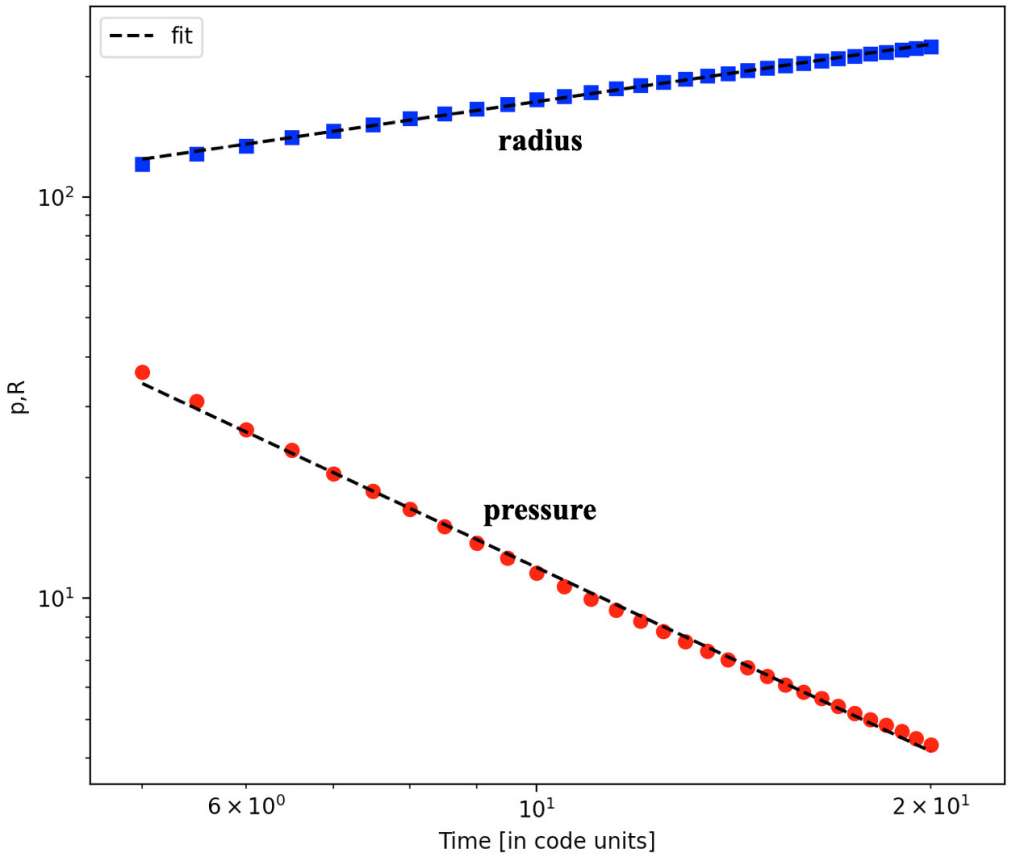

Figure 2.7. Time evolution of shock pressure p (red circles) and radius R (blue squares) in log-log scale. A linear fit (black dashed lines) through the data gives $p(t) \propto t^{-1.52}$ and $R(t) \propto t^{0.48}$.

slightly at the two time instances which has been accounted for while plotting the angular variation. We quantify the shape of the shock at late times to describe its self-similarity by fitting a polynomial to the numerical pressure and magnetic field data as shown by black dashed lines. As seen, pressure of the FS does not retain a self-similar shape over time in line with the discussion of section 2.3.3. The lateral dependance of the magnetic field is consistent with $\propto \cos\theta$ scaling, as expected from a point explosion in constant magnetic field. On the other hand, the scaling of pressure evolves with time, becoming flatter (more spherically symmetric). This indicates that the structure of the shocked medium with time evolves towards becoming more spherical, Sedov-Taylor-like solution.

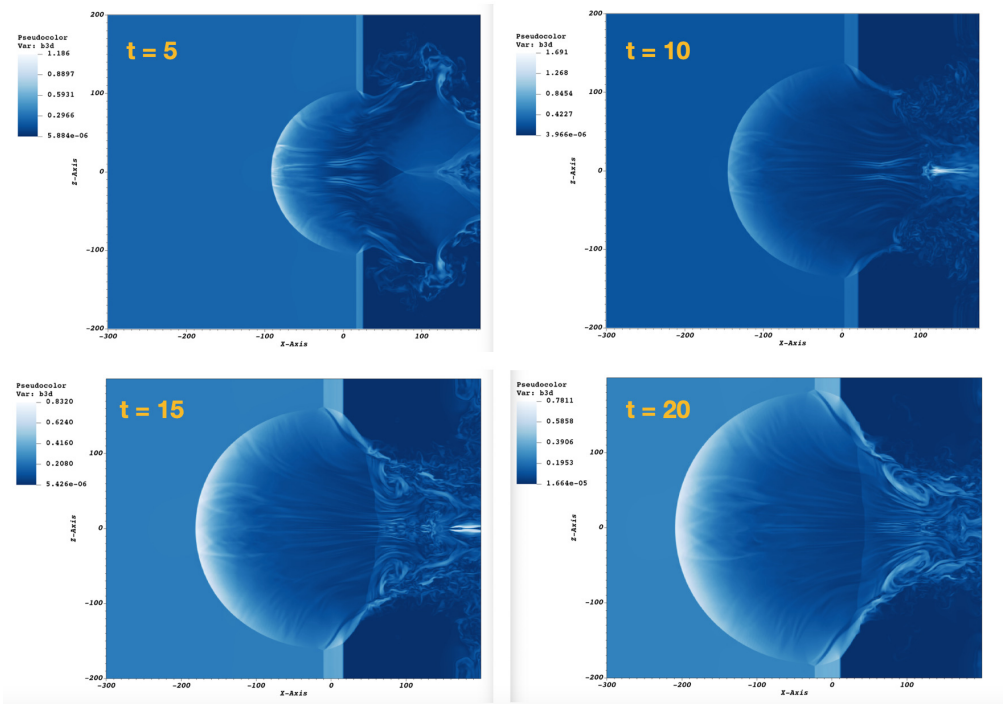

Figure 2.8. Same as figure 2.3 but colors indicate net magnetic field.

Another measure to demonstrate the FS's deviation from being self-similar is to compare its pressure (in units of the immediate post-shock value) versus radius (normalized by the shock radius) to the numerical and analytical Sedov solutions for a spherical blastwave as shown in figure 2.10. To make this comparison, we run low-resolution simulations ($N_{\rm X} = N_{\rm Y} = N_{\rm Z} = 256$) of the radio blob and spherical Sedov blastwave. For brevity, we call the former "Impact" case and the latter "Sedov" case. We compare the radius dependence of pressure using the pressure map similar to figure 2.3 to the numerical Sedov solution as well as the analytical Sedov solution reproduced from [37] (figure 17.3) at $t = 5, 10, 15$ and 20. In the case of the analytical Sedov solution (dashed black line in panel (b) of figure 2.10), pressure p reaches a limiting value of 0.306 (for $\gamma = 5/3$) as $r/R \to 0$. Numerical Sedov blastwave solutions approach this analytical value at later times as expected. For the impact case, due to the "exhaust" as discussed in section 2.4, pressure drops more rapidly and approaches a much lower limiting value (~ 0) than the Sedov limiting value. This again validates the discussion of section 2.3.3 that overall dynamics is not self-similar.

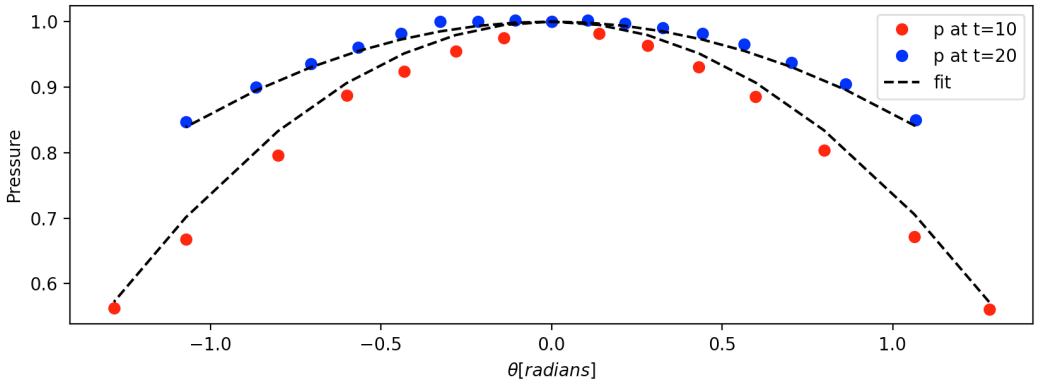

(a)

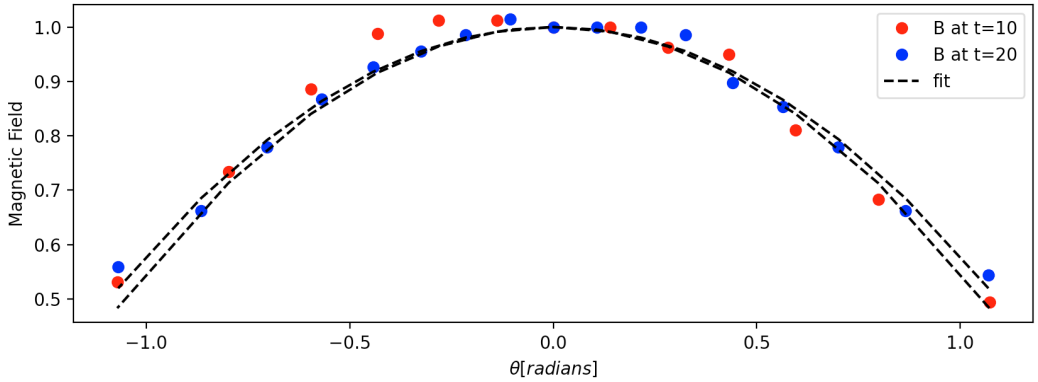

(b)

Figure 2.9. Angular variation of pressure and magnetic field at $t = 10$ (red circles) and 20 (blue circles) to describe self-similarity of the forward shock. θ is the angle between the x-axis and the line joining the center of the shock and the point of peak pressure/magnetic field along the FS when seen along several $z = 0$ cuts in the xz plane. (a) The fitting equations of pressure are $p(\theta)_{t=10} = 1 - 0.27\theta^2$ and $p(\theta)_{t=20} = 1 - 0.14\theta^2$. (b) The fitting equations of magnetic field are $B(\theta)_{t=10} = 1 - 0.45\theta^2$ and $B(\theta)_{t=20} = 1 - 0.42\theta^2$. The pressure profile does not retain a self-similar shape over time as discussed in section 2.3.3.

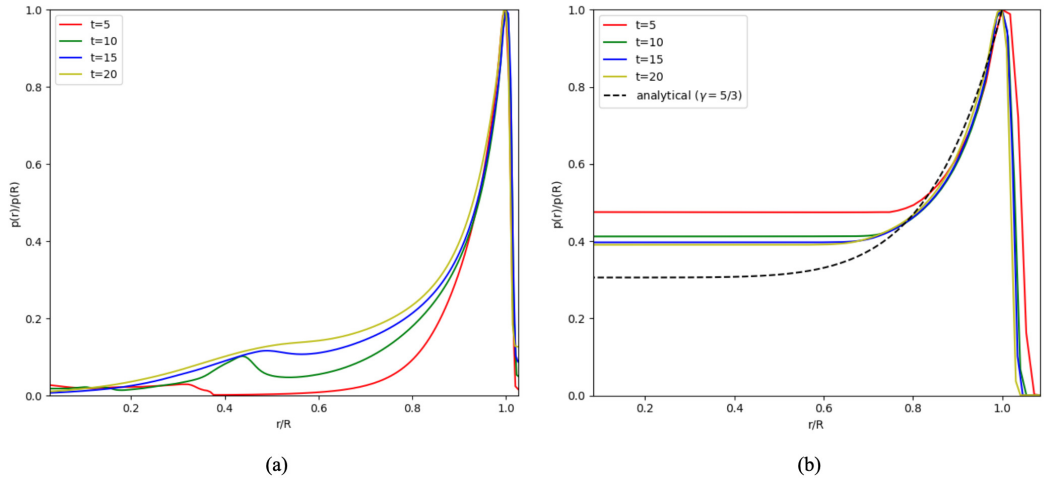

Figure 2.10. Internal structure of the shocked ISM compared to the Sedov-Taylor case. Plotted are normalized pressure versus radius of the FS of the "Impact" case (panel a) and Sedov-Taylor (panel b). In the impact case, the pressure in the bulk of the flow drops rapidly due to back flow of material and reaches a much lower limiting value than that of a Sedov-Taylor blastwave.

Finally, the intermediate self-similarity of FS between momentum and energy conserving regimes is established according to the discussion of section 2.3.3 where $n \approx 1.05$ - an excellent agreement between theory and numerical results.

2.4.3 Effects of reconnection between ejecta and ISM

We describe results of the low-resolution simulation related to the physical set-up of section 2.3.2, in figures 2.11 and 2.12, which will determine the effects of magnetic reconnection. Upper panels of 2.11a and 2.11b depict the y component of current J_y, where $\boldsymbol{J} = \nabla \times \boldsymbol{B}$ for the parallel and anti-parallel cases respectively, projected in 2-D (xz plane) at $t = 1.5$ and 3. Lower panels are profiles of J_y plotted along $z = 0$ at the same two time instants. Figure 2.12 is a schematic to understand current formation and magnetic reconnection.

At $t = 1.5$, going from left to right, magnetic field compression at the forward shock (shown by congregated arrows in figure 2.12) is accompanied by equal magnitudes of current for parallel and anti-parallel cases. However, for the parallel case, field compression is followed by a strong current sheet near the contact discontinuity (CD) as seen from the relative

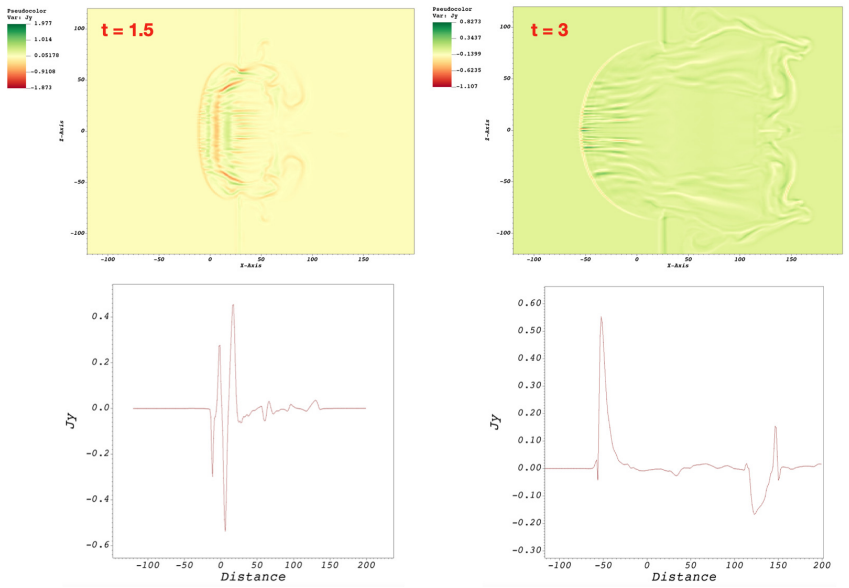

(a)

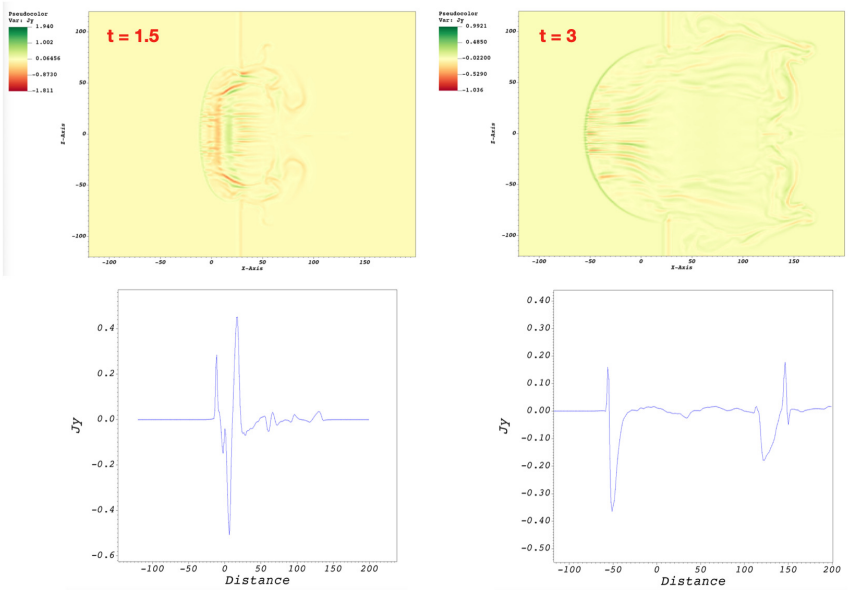

(b)

Figure 2.11. Analysis of magnetic reconnection in terms of currents plotted in 2-D and 1-D for the (a) parallel and (b) anti-parallel set-ups. In both, upper two panels are slices in the xz plane of the low-resolution MHD simulation of the interaction of radio blob with a parallel ISM magnetic field captured at $t = 1.5$ and 3. Colors indicate y component of current J_y. Lower two panels are J_y profiles plotted along $z = 0$ at the same two time instants. Magnetic field compression at the forward shock is identical in both cases but with opposite orientations, whereas the current sheet following it is much weaker in the anti-parallel case than the parallel case at both time instances.

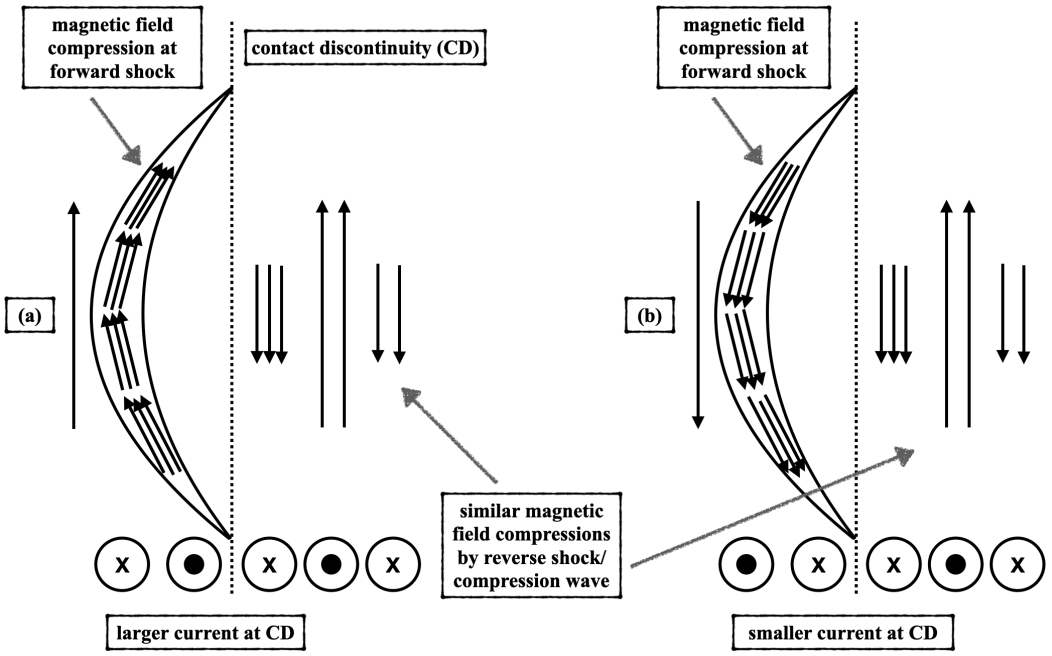

Figure 2.12. Qualitative picture of magnetic field compression at the forward shock and current sheet formation at the contact discontinuity followed by similar field compressions in the blob by the reverse shock/compression wave in the (a) parallel and (b) anti-parallel orientations. Arrows depict magnetic field vectors in the xz plane and current J_y is shown going into or out of the page.

magnitudes of J_y for the two cases at a distance of ~ -10. These current peaks are then followed by current in the blob material, evolving identically in both cases. In other words, both the parallel and anti-parallel orientations exhibit similar magnetic field compressions by the reverse shock passing through the blob material. At $t = 3$, the same pattern follows except that the field compressions at the FS get significantly weaker for both cases compared to their earlier time counterparts, whereas current sheet at the CD becomes stronger.

Our results do not show any significant effects of magnetic reconnection as we do not see a considerable difference in the magnetic field structure between the parallel and anti-parallel orientations. Magnetic reconnection at the CD in the parallel case plays only a mild role and field evolution is mostly dominated by MHD-type dynamics. For the analysis of shock properties and describing the radio emission, we perform a high-resolution simulation of the

blob-ISM interaction with the anti-parallel orientation to minimize the effects of magnetic reconnection, albeit a weak influence (see section 2.3.2 and panel 2.1b).

2.5 Emissivity maps and light curves

2.5.1 Synthetic synchrotron emissivity

To analyze the radio emission from the 2004 GF, we create integrated synthetic synchrotron emissivity maps using models of [38] and [39] which estimate the evolution of synchrotron radio emission from supernova remnants (SNRs). Recall that our 3-D numerical results of pressure and radius are qualitatively similar to the evolution of a Sedov-Taylor blastwave, namely that the hydrodynamic evolution is approximately self-similar and $R \propto t^m$.

We briefly describe the model of [38] referred to as the standard model. If absorption effects are neglected, the synchrotron luminosity of a radio SNR is

$$L_\nu \propto 4\pi R^2 \Delta R K B^{\frac{\gamma+1}{2}} \nu^{-\frac{\gamma-1}{2}} \tag{2.10}$$

Thus, the synchrotron volume emissivity is

$$\mathrm{j}_\nu \propto K B^{\frac{\gamma+1}{2}} \tag{2.11}$$

The power-law energy distribution of emitting electrons is $N(E) = KE^{-\gamma}$, where E is energy and K is a constant. The value of γ is determined from observations. Observations of radio emission of the 2004 GF report the emission spectrum to be characterized by an unbroken power law with $\gamma = 2.5$ [16].

Under the standard model, we create two emissivity maps (map1 and map2) based on assumptions about the efficiency of shock acceleration and magnetic field amplification as described by [40]. Turbulent magnetic field amplification is a prominent mechanism for synchrotron emission in SNRs. [41]–[43] discuss that to account for the observed radio synchrotron emission on average, magnetic field inside SNRs must be much higher than typical ISM values, $B_{\mathrm{ISM}} \approx 5\mu$G. A possible mechanism of magnetic field amplification in

SNRs considered by [42], [44], [45] is that of Rayleigh-Taylor instability of the CD, separating ejecta from the swept-up ISM. On the other hand, a very efficiently accelerated nuclear cosmic ray (CR) component can cause nonlinear magnetic field amplification near the shock [46]. Observational evidence of such a mechanism is presented by analyzing the synchrotron spectrum of SN 1006 [47], Cassiopeia A [48] and Tycho's SNR [49].

Map1 is based on the assumption of magnetic field amplification where the shock puts constant fractions of post-shock pressure $p = \rho_0 V_s^2$ (ρ_0 is the ISM density, V_s is the shock speed) into the magnetic field energy [50] and electron energy. Thus, $K \propto p$ and $B^2 \propto p$ giving $\mathrm{j}_\nu \propto p^{\frac{\gamma+5}{4}}$. Map2 is based on the assumption that instead of being amplified, magnetic field is simply compressed from a uniform upstream value. In this case, $\mathrm{j}_\nu \propto pB^{\frac{\gamma+1}{2}}$. With $\gamma = 2.5$, the two synthetic synchrotron maps are defined by the following scalings

$$\mathrm{j}_{\nu,\mathrm{map1}} \propto p^{1.875} \tag{2.12}$$

$$\mathrm{j}_{\nu,\mathrm{map2}} \propto pB^{1.75} \tag{2.13}$$

2.5.2 Emissivity maps

Figure 2.13 shows 2-D $y = 0$ slices of the two synchrotron emissivity maps scaled as $p^{1.875}$ and $pB^{1.75}$ at late times, $t = 20$. Panel (a) mimics the pressure map of figure 2.3, just with a different scaling. It is seen that the shock front (apex at $x \sim -200$), which is the site for electron acceleration, is where all the emission originates. A slight rebrightening appearing at $x \sim 110$ is insignificant compared to the emission at the FS and does not contribute to the temporal evolution of luminosity. FS emission in case of magnetic field compression (panel (b)) is weaker than that with magnetic field amplification, presumably due to dissipation of magnetic field because of the interaction between the magnetized ISM and blob.

Figure 2.14 depicts numerical 2-D (yz plane) maps obtained by integrating late-time ($t = 20$) synthetic emissivities along lines-of-sight at varying angles from x-axis, namely $\theta = 0, \pi/6, \pi/4$ and $\pi/3$. Panel 2.14a are the integrated emissivities for the prescription $p^{1.875}$ and panel 2.14b are the integrated emissivities for the prescription $pB^{1.75}$. The latter

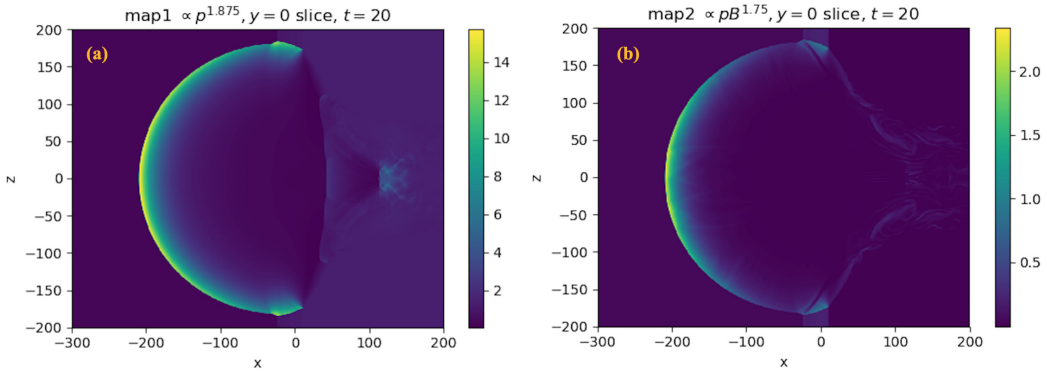

Figure 2.13. Slices in the xz plane ($y = 0$) depicting synthetic synchrotron emissivity at late times, $t = 20$, created from the high-resolution MHD simulation of the interaction of radio blob with external ISM. (a) Color bar indicates $\mathrm{j}_{\nu,\mathrm{map1}} \propto p^{1.875}$. (b) Color bar indicates $\mathrm{j}_{\nu,\mathrm{map2}} \propto pB^{1.75}$.

has a weaker integrated emission than the former due to magnetic field interactions. It is seen from both maps that emission from the limb (outer boundary of the spherical emission) is bright and dominates over the apex (in the vicinity of $z = 0$) emission along all oblique ($\theta > 0$) lines-of-sight.

In an effort to understand the results of the simulations, we constructed semi-analytical emission maps shown in figure 2.15. We approximate the emitting volume as a half-sphere $z > 0$ with surface brightness given by the normalized pressure fit $p(\theta)_{t=20} = (1 - 0.14\theta^2)$ (at time 20) as described in section 2.4.2. The observer is located at angle θ_v. We assume that emission is generated in a thin shell near the surface of the bubble. (As described previously, the post-shock pressure is released through back flow, leading to fast decrease of emissivity). We then calculate the observed emissivity map according to the prescription $p^{1.875}/(\cos\theta_{r-v} + c_1)$, where θ_{r-v} is the local angle between the line-of-sight and the radial direction in the emitting bubble. Parameter $c_1 = 0.1$ is introduced to avoid unphysical values of emissivity when the line-of-sight is tangential to the surface.

Our semi-analytical results reproduce qualitatively the numerics of figure 2.14. Emissivity shows strong limb brightening due to longer path through emitting volume. On the other hand, effects of pressure (and thus emissivity) variations along the shock produce only mild variations of intensity.

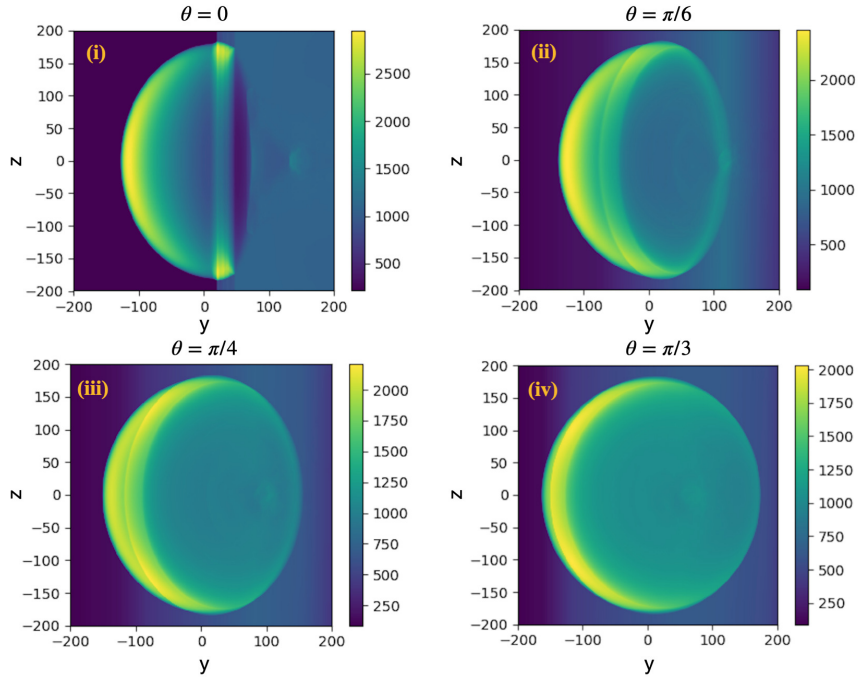

(a)

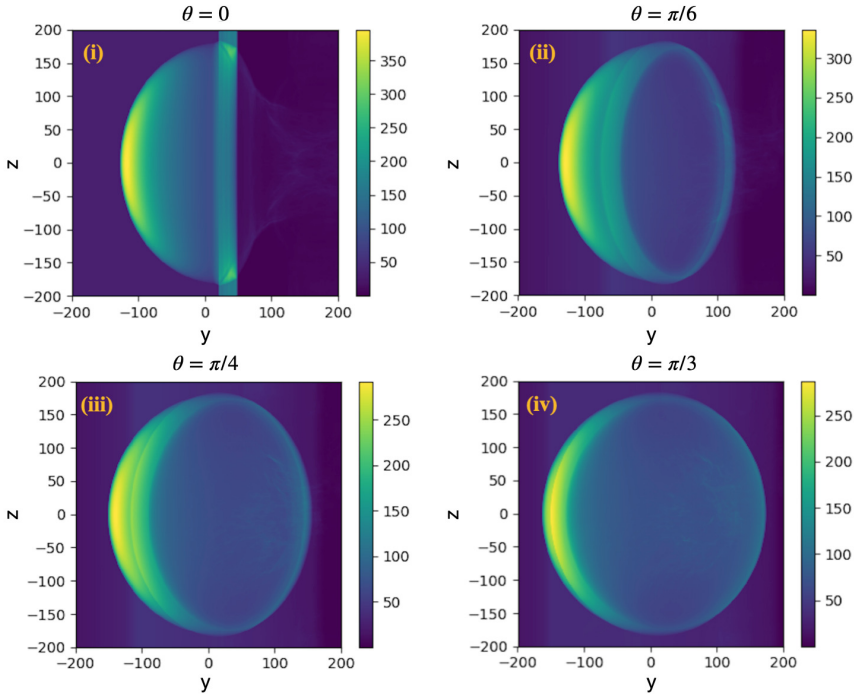

(b)

Figure 2.14. Integrated 2-D emissivity maps for the two prescriptions of figure 2.13, (a) $p^{1.875}$ and (b) $pB^{1.75}$, along various lines-of-sight, namely $\theta = 0, \pi/6, \pi/4$ and $\pi/3$, at late times, $t = 20$. Emission from the limb dominates the apex emission at all oblique lines-of-sight.

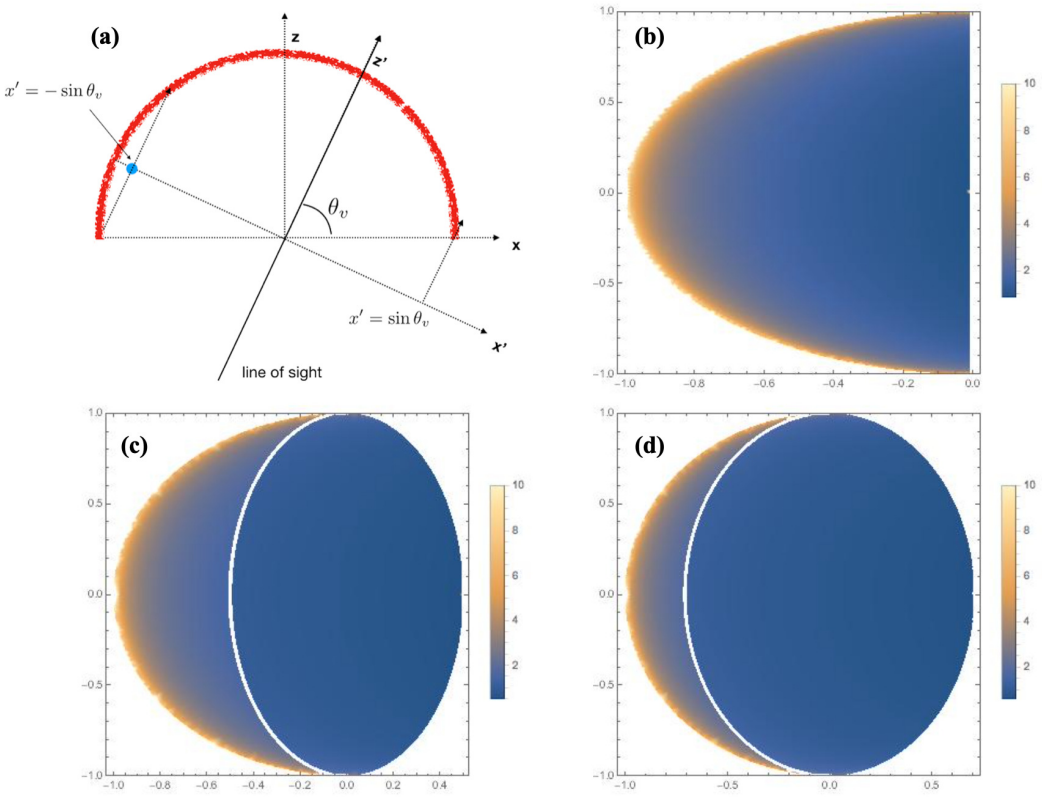

Figure 2.15. Towards an analytical model of emissivity. (a) Illustration of the model: an emitting semi-sphere is viewed at angle θ_v. (b) $\theta_v = 0$, (c) $\theta_v = \pi/6$, and (d) $\theta_v = \pi/4$. The scales are normalized to the radius of the cavity. The maps are mostly dominated by the line-of-sight effects, not the fact that pressure/emissivity are higher at the apex point.

2.5.3 Light curves

In figure 2.16, we show the temporal evolution of normalized luminosities obtained by summing the two scalings described by 2.12 and 2.13 over the entire computational box. Synthetic light curves are plotted from $t = 5$ to $t = 20$ in steps of 0.5 in log-log scale. A linear fit to the plots gives power laws for synchrotron luminosities: $L_{\nu,\mathrm{map1}} \propto t^{-0.7}$ and $L_{\nu,\mathrm{map2}} \propto t^{-0.1}$. As reported in observations, the radio light curve evolves as $\sim t^{-1}$ after undergoing rebrightening, which marks the self-similar Sedov-Taylor evolution phase of the radio nebula. Our synthetic emissivity map based on the assumption of magnetic field amplification is able to account for this observed temporal evolution more closely. In addition, temporal evolution of numerical emissivity deviates from that of an ideal Sedov remnant with magnetic field

amplification, characterized by $R(t) \propto t^m$ and $m = 0.4$. For such a case, the shock puts constant fractions of the post-shock pressure into electron energy and magnetic-field energy, that is, $K = B^2 \propto \rho_0 V_s^2$. Since integrated luminosity $L_\nu \propto R^3 K B^{1+\alpha}$ and $V_s \propto t^{m-1}$, $L_\nu \propto t^{m(6+\alpha)-(3+\alpha)}$ [40], where $\alpha = \frac{\gamma-1}{2} = 0.75$ based on observations. Thus, $L_\nu \propto t^{-1.05}$. This discrepancy between numerics and an ideal Sedov remnant is expected because of the faster pressure drop due to considerable "exhaust flow" in the impact case. On the other hand, if we use the values of exponents from the simulated radius and pressure evolution, that is, $R(t) \propto t^{m_1}$ and $p(t) \propto t^{m_2}$ (section 2.4.1), unlike the ideal Sedov case where pressure and radius are mutually dependent, integrated luminosity $\mathrm{L}_\nu \propto R^3 p^{(3+\alpha)/2} \propto t^{[6m_1+m_2(3+\alpha)]/2}$. This gives a semi-analytical estimate of luminosity $L_\nu \propto t^{-1.4}$ where the exponent is twice that of the purely numerical emissivity.

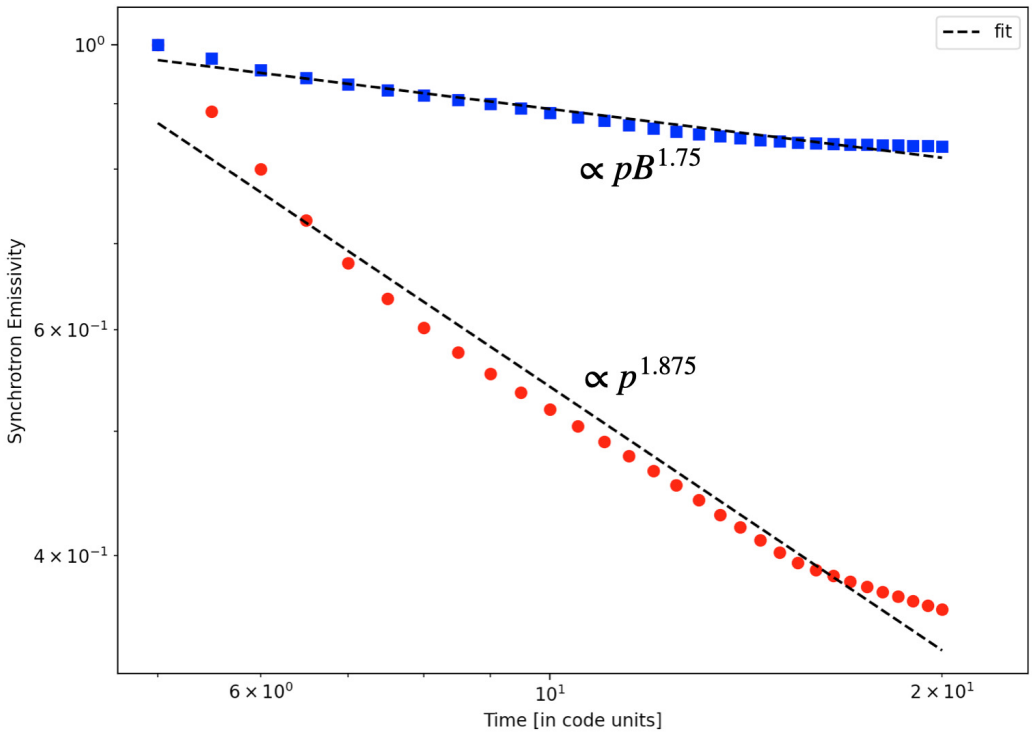

Figure 2.16. Temporal evolution of total synchrotron emissivity normalized by maximum values. Fits (black dashed lines) through the linear part of the light curves give $L_{\nu,\mathrm{map1}} \propto t^{-0.7}$ and $L_{\nu,\mathrm{map2}} \propto t^{-0.1}$.

To compare with observations of radio emission from SNRs, we define a secular decline rate $-d = L_\nu^{-1} dL_\nu/dt$. [51] report such a decline rate of 0.92yr^{-1} for Tycho Brahe's SNR radio emission which is frequency-independent. Within the frequency range of 86-5000 MHz, the weighted mean value of the decline rate is 0.41yr^{-1}. A list of values for the decline rate for the radio emission from CasA at different frequencies is tabulated by [52]. The secular decline rate has values ranging from $0.3 - 1\text{yr}^{-1}$. Another estimate of Tycho's flux decrease rate is quoted by [53] who report that the luminosity at 1667 MHz is weakening with an annual mean rate of 0.47%. A corresponding rate for Kepler's SNR is 0.2%. Lastly, [54] present the evolution of secular decrease rate from their extensive observations of the radio emission from SN 1993J in the frequency range 85-110 GHz. The flux decline rate steepens from ~ 0.7 to ~ -2.7 at ~ 3100 days after the shock breakout, which they describe as an exponential decay, rather than a power-law decline. From MHD simulations, $-d = 0.7$ (per unit time) for the case with magnetic field amplification and $-d = 0.1$ (per unit time) for the case without amplification. Considering the simplicity of our MHD model and overall uncertainties and errors reported in observations, these secular decline rates are reasonably consistent with those of popular radio SNRs.

2.6 Discussion and conclusions

In this work we model the radio afterglow emission from the 27 December, 2004 giant flare from SGR 1806-20. We consider the interaction of light, magnetically dominated cloud (CME) ejected during the magnetar flare with the surrounding ISM. We identify the observed emission features with the forward shock created by the impact. The magnetic blob is first advected with the magnetar wind, and later impacts on the ISM. The impact creates a forward shock, and a complicated backward flow.

Since the CME implants both energy and momentum into the ISM, the flow is not self-similar. Yet, we find that the dynamics of the forward shock (*e.g.* motion of the apex point) closely follows the Sedov-Taylor (energy conserving) prescription. We also find that the lateral structure of the shock quickly becomes self-similar, so that pressure at the forward shock can be parametrized as $p(t, \theta) = p_0(t) f(\theta)$. On the other hand, the internal structure

of the shocked material is strongly modified by the backward exhaust flow: the pressure in the bulk decreases much faster than in Sedov-Taylor case.

We identify a number of magnetohydrodynamic features of the interaction that can contribute to particle acceleration and the production of radio emission: (i) reconnection between the CME's and ISM's magnetic field; (ii) forward shock generated in the ISM; (iii) reverse shock in the CME, and (iv) shocks in the exhaust flow of the ISM.

Relative importance of these contributions is expected to depend mostly on the parameters of the CME. We adopt a magnetically-dominated paradigm for the ejected CME (if a flare was a magnetospheric event, large baryonic loading is not expected). The CME is then "light and fast": it carries a lot of energy, but not much mass or momentum. As a result of this assumption, the contribution from the reverse shock in the ejecta is insignificant. We also find that for our parameters, the reconnection between internal and ISM magnetic fields does not contribute considerably: it is the forward shock and the shocks in the exhaust flow that dominate the pressure.

To compare with observations we employ two prescriptions to connect MHD properties with radio emissivity: pure compression of the magnetic field, as well as turbulent amplification. This is, naturally, the weakest point of the model. Accounting for radio emission, that carries a tiny fraction of luminosity and total energetics, is a notoriously difficult problem in the study of SNRs [40], [55], [56]. However, the mechanism of magnetic field amplification is often invoked to explain synchrotron emission in SNRs [41]–[43].

Observations [15], [16] are similarly complicated, showing somewhat different evolution at different frequencies and changing temporal behavior. However, considering the simplicity of the MHD model and the complications involved in quantifying radio synchrotron emission, our analysis with field amplification produces a light curve ($\sim t^{-0.7}$) closer to the observed temporal evolution of the SGR 1806-20 radio nebula ($\sim t^{-1.1}$) in the self-similar phase, as well as consistent with observations of radio emission from other SNRs. This, in turn, could mean that field amplification might indeed play a significant role in radio afterglows from magnetar giant flares.

An interesting feature of the observed radio light curve is rebrightening at $\sim$ 25 days when the radio flux increases by a factor of $\sim$ 2 [18]. A scenario with a pre-existing shell

around the SGR is invoked to explain this flux increase when the emission from swept-up material dominates the light curve [17], [19]. We test this hypothesis through our MHD simulation (appendix A.2). Although the presence of a dense shell produces a break in the temporal evolution of flux, we find no evidence of rebrightening in the light curve due to the impact of the magnetic cloud on the shell. Interestingly, the late-time light curve with only magnetic field compression ($\sim t^{-1}$) does better at accounting for observations, if the shell scenario were to be accepted.

Acknowledgements

The numerical simulations were carried out in the CFCA cluster of National Astronomical Observatory of Japan. We thank the *PLUTO* team for the possibility to use the *PLUTO* code and for technical support. Visualization of results was performed in the VisIt package and using Python. This work had been supported by NASA grants 80NSSC17K0757 and 80NSSC20K0910, NSF grants 10001562 and 10001521.

3. TILTING INSTABILITY OF MAGNETICALLY CONFINED SPHEROMAKS

A version of this chapter was previously published by the *Journal of Plasma Physics*: **Mehta, R., Barkov, M., Sironi, L., & Lyutikov, M. (2020).** "Tilting instability of magnetically confined spheromaks". *Journal of Plasma Physics, 86(4), 905860407. DOI: 10.1017/S0022377820000768*. This article was **selected as one of the "Featured Articles"** by JPP.

This work had been supported by **NASA grant 80NSSC17K0757 and NSF grants 1903332 and 1908590**. L.S. acknowledges support from the **Sloan Fellowship, the Cottrell Scholars Award, and NSF PHY-1903412**.

We consider the tilting instability of a magnetically confined spheromak using three-dimensional magnetohydrodynamic and relativistic particle-in-cell calculations with an application to astrophysical plasmas, specifically those occurring in magnetar magnetospheres. The instability is driven by the counter-alignment of the spheromak's intrinsic magnetic dipole with the external magnetic field. Initially, the spheromak rotates – tilts – trying to lower its magnetic potential energy. As a result, a current sheet forms between the internal magnetic field of a spheromak and the confining field. Magnetic reconnection sets in; this leads to the annihilation of the newly counter-aligned magnetic flux of the spheromak. This occurs on a few Alfvén time scales. In the case of a higher-order (second-order) spheromak, the internal core is first pushed out of the envelope, resulting in formation of two nearly independent tilting spheromaks. Thus, the magnetically twisted outer shell cannot stabilize the inner core. During dissipation, helicity of the initial spheromak is carried away by torsional Alfvén waves, violating the assumptions of the Taylor relaxation theorem. In applications to magnetar giant flares, fast development of tilting instabilities and no stabilization of the higher-order spheromaks make it unlikely that trapped spheromaks are responsible for the tail emission lasting hundreds of seconds.

Key words: plasma confinement

3.1 Introduction

Relaxation of magnetized plasma is a fundamental problem in laboratory and space plasma physics [57]–[59]. In this work we are particularly interested in the relaxation processes in highly magnetized astrophysical plasmas, where the magnetic field controls the overall dynamics of the plasma, and the dissipation of magnetic energy may power the observed high-energy emission. The most relevant astrophysical settings include magnetars (strongly magnetized neutron stars possessing super-strong magnetic fields [5], [13]), pulsars and pulsar wind nebulae [60], jets of active galactic nuclei and γ-ray bursters [22]. All these objects are efficient emitters of X-rays and γ -rays, and in the past two decades they have been subjects of intensive observational study via a number of successful high-energy satellites. These objects seem to share one important property – they include relativistic magnetized plasmas, and often the plasma is magnetically dominated, *i.e.*, the energy density of this plasma is mostly contributed not by the rest mass energy of matter, but by the energy of the magnetic field. This is dramatically different from laboratory plasmas, magnetospheres of planets and interplanetary plasma. This extreme regime can only be probed (although, indirectly) via observations of relativistic astrophysical sources, by unveiling the imprint left by the magnetic field dissipation on the observed emission.

In addition to high (relativistic) magnetization, astrophysical plasmas differ from laboratory ones by the absence of pre-arranged conducting walls. This has important implications for stability and the applicability of the Taylor relaxation principle as we discuss below.

3.2 Spheromaks and magnetohydrodynamic relaxation

Particularly important are static equilibria when magnetohydrodynamic (MHD) equations demand

$$\nabla p = \boldsymbol{J} \times \boldsymbol{B} \tag{3.1}$$

where p is plasma pressure, and $\boldsymbol{J}$ and $\boldsymbol{B}$ are current density and magnetic field. For magnetically dominated regimes, the pressure gradient is negligible, and plasma equilibrium becomes a force-free equilibrium [61]

$$\boldsymbol{J} \times \boldsymbol{B} \approx 0 \tag{3.2}$$

Of particular importance is the Taylor state, where $\boldsymbol{J} \propto \boldsymbol{\nabla} \times \boldsymbol{B} = \lambda \boldsymbol{B}$ with spatially constant λ. An initially turbulent plasma is expected to spontaneously relax (or self-organize) to a simple, well-defined Taylor state. In a finite volume the system reaches a state with the smallest possible λ (largest scale configurations). In cylindrical geometry the corresponding configurations - Lundquist states [62] - are indeed the endpoints of relaxation [63]. Importantly, Lundquist states are, in a sense, connected to walls - they extend infinitely along the symmetry axis.

In spherical geometry the force-free configurations with constant λ are called spheromaks [64], [65]. Spheromaks have a number of features that make them useful as basic plasma structures, building blocks of plasma models. First, spheromaks are not connected to any confining wall such as that of a laboratory vessel or to coils and hence represent a 'pure' kind of plasma configuration that could be achieved by internal plasma relaxation. Internally spheromaks are simply connected (not topological tori). Second, they represent a relaxed (Taylor) state - one might expect that a turbulent plasma would spontaneously relax (or self-organize) to a simple state resembling a spheromak.

Astrophysical plasmas like those found in magnetar magnetospheres [13], [66]–[68] are likely to evolve into a force-free configuration, effectively confined through the creation of a system of nested poloidal flux surfaces. Given the appropriate initial conditions, spheromaks can form spontaneously due to plasma instabilities and hence can be hypothesized to form in an astrophysical environment. For example, it was suggested that spontaneous instabilities arising in plasmas can lead to a spheromak configuration which suggests that such configurations should occur in nature. Indeed, the magnetically confined fireball picture has been invoked to explain coronal mass ejections arising in solar flares [26], [66], [69] and high-energy flaring/bursting activity of magnetars [13], [67], [70].

In this paper we are mostly interested in astrophysical applications, particularly in the high magnetization regime. First, in that case the effects of finite gyro-radius are not important. For example, in the magnetospheres of magnetars the magnetic field is of the order of the quantum field, so that even at relativistic temperatures the gyro-radius is only $\sim 10^{-11}$ cm, many orders of magnitude smaller than the expected overall size of $\sim 10^6$ cm. Thus, astrophysical configurations we are interested in are well in the MHD regime. Secondly, stability of spheromaks and field-reversed configurations (FRC) in laboratory setting depends on the arrangement of confining conducting walls [64], [71]–[73]. In contrast, astrophysical configurations are generally expected to be less affected by the presence of conducting walls. Spheromaks also present a simple, analytically tractable configuration, as opposed to FRC configurations where initial state has to be calculated numerically.

In contrast to the cylindrical Lundquist case, the three-dimensional (3-D) magnetically confined basic spheromaks are unstable in the absence of conducting walls [64], [71]. The basic reason for instability is that the magnetic dipole moment of a trapped spheromak is anti-aligned with an external magnetic field. As a result, a magnetically confined spheromak is intrinsically unstable and would prefer to tilt to lower its magnetic potential energy. A number of authors considered stabilizing effects of conducting magnets on the evolution of the spheromak [74]–[76]; see [77] for review of spheromak research.

In this paper, we reanalyse the structure and time evolution of magnetically confined spheromaks using 3-D MHD and particle-in-cell (PIC) simulations with an application to astrophysical plasmas occurring in magnetar magnetospheres. Previously, reconnection and particle acceleration due to current-driven instabilities in Newtonian, initially force-free plasmas in 2.5-D and 3-D scenarios using high-resolution simulations both with a fixed grid and with adaptive mesh refinement is studied extensively in [78]. In 2.5-dimensions, the two parallel repelling current channels in an initially force-free equilibrium are first subject to a linear instability consisting of an antiparallel displacement and thereafter undergo a rotation and twisting motion. They quantify the growth rate of this tilting instability by a linear growth phase in the bulk kinetic energy during which reconnection of magnetic field lines causes the formation of nearly singular current sheets and secondary islands leading to particle acceleration. Our 3-D MHD simulation (§ 3.3.3 and figures 3.1 and 3.2) of the force-free

spheromak clearly displays the onset of a similar tilt instability and twisting motion which leads to magnetic reconnection at the boundaries between the spheromak and the external field, causing the spheromak to eventually dissipate.

3.3 Spheromak in external magnetic field

3.3.1 Basic spheromak

Let us first briefly recall the structure of magnetically confined spheromaks. In the Grad-Shafranov formalism [79], [80] the magnetic field can be represented by a scalar flux function ψ in spherical coordinates

$$\boldsymbol{B} = \nabla\psi \times \nabla\phi + \lambda\psi\nabla\phi \tag{3.3}$$

where ϕ is the toroidal coordinate. An axisymmetric solution of (3.3) within a sphere of radius r_0 and constant λ is a spheromak [64], [65].

Using (3.3) and condition for the Taylor state, the Grad-Shafranov equation of axisymmetric force-free toroidal plasma equilibrium can be represented in spherical coordinates [81]

$$r^2\frac{\partial^2\psi}{\partial r^2} + \sin\theta\frac{\partial}{\partial\theta}\left(\frac{1}{\sin\theta}\frac{\partial\psi}{\partial\theta}\right) + (\lambda r)^2\psi = 0 \tag{3.4}$$

Equation (3.4) can be solved using separation of variables inside and outside the spheromak.

Inside the spheromak, the magnetic field components are

$$\left.\begin{aligned} B_r &= 2A_0\frac{\lambda}{r}\mathrm{j}_1(\lambda r)\cos\theta \\ B_\theta &= -A_0\frac{\lambda}{r}\frac{\partial}{\partial r}(r\mathrm{j}_1(\lambda r))\sin\theta \\ B_\phi &= A_0\lambda^2\mathrm{j}_1(\lambda r)\sin\theta \end{aligned}\right\} \tag{3.5}$$

where, $\mathrm{j}_1(\lambda r)$ is spherical Bessel function of the first kind.

The radial and toroidal components of magnetic field vanish on the surface of spheromak which corresponds to $j_1(\lambda r) = 0$ at $r = r_0$. This gives the smallest allowed λ corresponding to the lowest energy Taylor state

$$\lambda \approx 4.493/r_0 \tag{3.6}$$

Outside the spheromak, magnetic field is

$$\boldsymbol{B_{ex}} = \left(B_0 \cos\theta - B_0 \cos\theta \frac{r_0^3}{r^3}, -B_0 \sin\theta - B_0 \sin\theta \frac{r_0^3}{2r^3}, 0 \right) \tag{3.7}$$

where the magnetic field at very large distances asymptotes to a uniform field $B_0\hat{z}$. Since, magnetic field at the surface of the spheromak is continuous, the constant A_0 can be related to the external magnetic field B_0

$$A_0 \approx -0.342 B_0 r_0^2. \tag{3.8}$$

3.3.2 Tilt instability of a spheromak in an external magnetic field

The basic magnetically confined spheromak is unstable. The easiest way to see this is to note that a spheromak can be approximated as a magnetic dipole $\boldsymbol{\mu}$ embedded in an external magnetic field

$$\boldsymbol{\mu} = \frac{-B_0 r_0^3}{2} \hat{z}. \tag{3.9}$$

Equation (3.9) shows that the magnetic moment of a spheromak is anti-aligned with the external magnetic field and hence subject to tilt. Tilt instability of spheromak has been explored extensively by [65] and [82], both of which serve to validate the arguments made in this paper.

In [65] the spheromak is described as a small magnet between two large magnets oriented anti-parallel to large external magnets, hence unstable to tilting. The flipping of a spheromak by 180° to lower its potential energy, however, causes the external field to be such as to enhance rather than balance the spheromak hoop force. Equilibrium is quickly lost and the spheromak will explode outwards at Alfvén velocity. Our 3-D MHD simulations of § 3.3.3

show this dissipation of spheromak after undergoing tilt instability and aid us to estimate the dissipation timescale in units of Alfvénic crossing time.

In [82], a spheromak is described simply as a rigid current carrying ring and its various rigid instabilities like tilting, shifting, and vertical motions are discussed as modes which get activated depending on the value of the magnetic field index $n = -(r/B_0)(\partial B_0/\partial r)$ where B_0 is the magnitude of the external vertical magnetic field. The tilting mode is unstable for $n < 1$. For laboratory spheromak experiments, the growth rate of these instabilities which would eventually cause the spheromak to dissipate, is estimated to be $1 - 10\mu$s. We estimate such a timescale for astrophysical plasmas using results of our 3-D MHD simulations.

3.3.3 Three-dimensional MHD simulations of tilting instability

Numerical set-up

We perform 3-D MHD simulations of the lowest energy Taylor state as described by (3.5) and (3.6) as well as the 2-root spheromak with constant-density uniformly magnetized plasma to explore their time evolution and test their stability. The simulations were performed using a 3-D geometry in Cartesian coordinates using the *PLUTO* code[1] [30]. *PLUTO* is a modular Godunov-type code entirely written in C, intended mainly for astrophysical applications and high Mach number flows in multiple spatial dimensions and designed to integrate a general system of conservation laws

$$\frac{\partial \boldsymbol{U}}{\partial t} = -\nabla.\mathbf{T}(\boldsymbol{U}) + \boldsymbol{S}(\boldsymbol{U}), \tag{3.10}$$

where $\boldsymbol{U}$ is the vector of conservative variables and $\mathbf{T}(\boldsymbol{U})$ is the matrix of fluxes associated with those variables. For our ideal MHD set-up, no source terms are used and $\boldsymbol{U}$ and $\mathbf{T}$ are

$$\boldsymbol{U} = \begin{pmatrix} \rho \\ \boldsymbol{m} \\ \boldsymbol{B} \\ E \end{pmatrix}, \mathbf{T}(\boldsymbol{U}) = \begin{bmatrix} \rho\boldsymbol{v} \\ \boldsymbol{m}\boldsymbol{v} - \boldsymbol{B}\boldsymbol{B} + p_t\mathbf{I} \\ \boldsymbol{v}\boldsymbol{B} - \boldsymbol{B}\boldsymbol{v} \\ (E + p_t)\boldsymbol{v} - (\boldsymbol{v}.\boldsymbol{B})\boldsymbol{B} \end{bmatrix}^T, \tag{3.11}$$

[1] ↑http://plutocode.ph.unito.it/index.html

where $\rho, \boldsymbol{v}$ and p are density, velocity and thermal pressure. $\boldsymbol{m} = \rho\boldsymbol{v}$, $\boldsymbol{B}$ is the magnetic field and $p_t = p + |\boldsymbol{B}|^2/2$ is the total (thermal + magnetic) pressure, respectively. Magnetic field evolution is complemented by the additional constraint $\nabla.\boldsymbol{B} = 0$. Total energy density E

$$E = \frac{p}{\Gamma - 1} + \frac{1}{2}\left(\frac{|\boldsymbol{m}|^2}{\rho} + |\boldsymbol{B}|^2\right), \tag{3.12}$$

along with an isothermal equation of state $p = c_s^2\rho$ provides the closure; Γ and c_s are the polytropic index and isothermal sound speed, respectively. *MP5_FD* interpolation, a third-order Runge-Kutta approximation in time, and an Harten–Lax–Van Leer approximate Riemann solver [31] are used to solve the above ideal MHD equations.

The plasma has been approximated as an ideal, non-relativistic adiabatic gas, one particle species with polytropic index of 5/3. The size of the domain is $x \in [-2, 2]$ and $y \in [-2, 2]$, $z \in [-3.3, 3.3]$. To better resolve the evolution of spheromak, non-uniform resolution is used in the computational domain with total number of cells $N_{\mathrm{X}} = N_{\mathrm{Y}} = 312$ and $N_{\mathrm{Z}} = 520$. We also check that decreasing the resolution by a factor of two, that is, $N_{\mathrm{X}} = N_{\mathrm{Y}} = 156$ and $N_{\mathrm{Z}} = 260$, does not affect the simulation results. Convergence will be evident later in figures 3.4 and 3.5. Outflow boundary conditions are applied in all three directions.

In the simulation, values for constant external magnetic field B_0, radius of spheromak r_0 and plasma density ρ were set to 0.3, 0.75 and 1 respectively. With a magnetization $\sigma = B_0^2/\rho = 0.09$, Alfvén speed v_A is only mildly relativistic given by $v_A = B_0/\sqrt{\rho} = 0.3$. Our motive here is to stress more on astrophysical applications, in particular magnetar's magnetospheres, where the Alfvén velocity is expected to be relativistic. B_0, r_0 and ρ are used to estimate a time scale of propagation of magnetic oscillations within the spheromak in terms of Alfvénic crossing time $t_A = r_0/v_A = 2.5$. The timescale over which the spheromak disrupts is estimated later in units of t_A. Projections of total magnetic field and current density in the xz plane are denoted by $\boldsymbol{B3D}$ and $\boldsymbol{J}$ respectively. All quantities are given in code units which are normalized *cgs* values

$$\rho = \frac{\rho_{cgs}}{\rho_n}, v = \frac{v_{cgs}}{v_n}, p = \frac{p_{cgs}}{\rho_n v_n^2}, B = \frac{B_{cgs}}{\sqrt{4\pi\rho_n v_n^2}}, \tag{3.13}$$

where ρ, v, p and B are density, velocity, pressure and magnetic field. Time is given in units of $t_n = L_n/v_n$. The normalization values used are $\rho_n = 1.67 \times 10^{-24}$gr cm^{-3}, $L_n = 1.5 \times 10^{13}$ cm and $v_n = 10^5$cm s^{-1}.

Tilting instability of basic spheromak

We perform two types of simulations: one with resolution $312 \times 312 \times 520$ (I) and another with resolution $156 \times 156 \times 260$ (II). The following discussion describes results for simulation (I). Figures 3.1, 3.2 and 3.3 display time evolution of a basic magnetically confined spheromak. Shown are the 2D (xz plane) slices of a 3-D simulation. Vectors in figures 3.1 and 3.2 denote total magnetic field projected in the xz plane and those in figure 3.3 depict total current density projected in the xz plane. Color bars in figure 3.1 show plasma density, those in figure 3.2 show toroidal magnetic field B_y and those in figure 3.3 show toroidal current density J_y. Starting from $t = 0$, the spheromak is captured at subsequent time instants where significant changes to its morphology can be observed.

Initially at $t = 0$, the constant density plasma is in the relaxed lowest energy state - a spheromak composed of magnetic islands shown by red and blue blobs in figure 3.2 symmetrical on either side of the $x = 0$ (z) axis, depicting poloidal and toroidal components of magnetic field. Magnetic field at the center of spheromak is $-B_0\hat{z}$, that is, the spheromak's magnetic moment is anti-aligned with the external magnetic field. A basic spheromak is thus unstable against tilt.

Spheromak begins to tilt immediately after $t = 0$. At $t \sim 14.4t_A$, the plasma density inside the spheromak decreases slightly. This is because once dissipation starts, some of the trapped magnetic energy is converted into heat and at the same time magnetic tension within the spheromak decreases. As a result, the spheromak expands and plasma density decreases. At $t \sim 22.4t_A$, tilting is clearly visible; spheromak starts to rotate about the center and tries to align its magnetic moment with the external field to lower its energy. As the spheromak tilts, the matching of internal and external magnetic fields no longer holds, resulting in a current sheet formation on its surface and the onset of magnetic reconnection. The third panel of figure 3.3 clearly shows the formation of this current sheet on the surface of

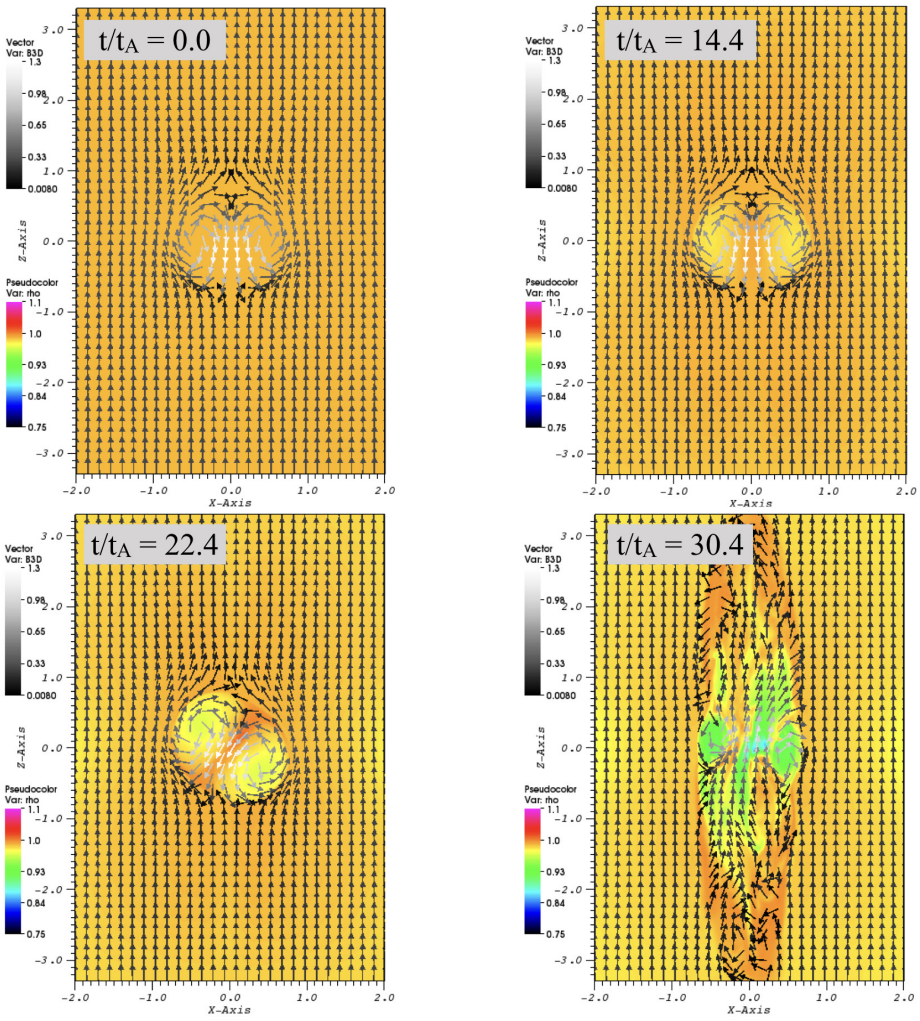

Figure 3.1. Slice in the xz plane of MHD simulation of lowest energy Taylor state. Times indicated in the panels are in units of the Alfvénic crossing time $t_A = r_0/v_A$. Colors indicate plasma density while vectors depict $\boldsymbol{B3D}$.

spheromak. It should be noted that while there is no resistivity in ideal MHD, the processes responsible for dissipation, current sheet formation and magnetic reconnection, are due to numerical resistivity caused by errors introduced by spatial and temporal discretization.

The simulation terminates at $t \sim 30.4 t_A$, when plasma hits the walls of the simulation domain. In this quasi-final state, which marks the partial disruption of the spheromak, plasma becomes less dense, magnetic islands rotate fully and magnetic field lines near the center are aligned with the z-axis. In figure 3.1, smaller magnetic islands are still seen

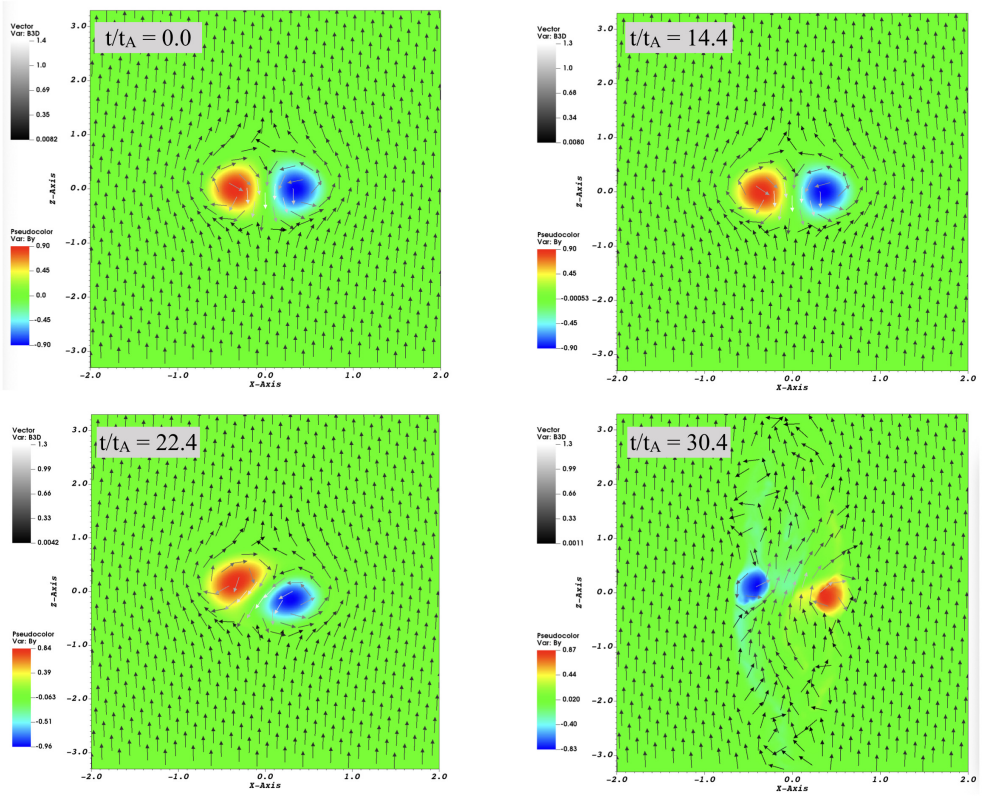

Figure 3.2. Same as figure 3.1 but showing the value of toroidal magnetic field B_y (color scheme); vectors depict ***B3D***.

about the center and magnetic field at their edges is opposite to the external field. Current sheets are still visible around these residual magnetic islands, as seen in the fourth panel of figure 3.3. If the simulation is made to run longer, these magnetic islands will also reconnect at the edges and dissipate. The 3-D MHD simulation of the lowest energy Taylor state is concurrent with the argument made in § 3.3.2 that a spheromak confined in external magnetic field is intrinsically unstable; it first tries to tilt to lower its energy and eventually dissipates.

Tilt instability growth rate and magnetic energy dissipation

Figure 3.4 depicts the time evolution of θ, $\langle E_{tot}^2 \rangle / \langle E_m^2 \rangle$ and E_{tot} for the two different resolutions (I) and (II) and also shows convergence. Here, θ is the tilt angle defined as the angle between the total magnetic field at the origin and z-axis, $\langle E_{tot}^2 \rangle$ is the box-averaged

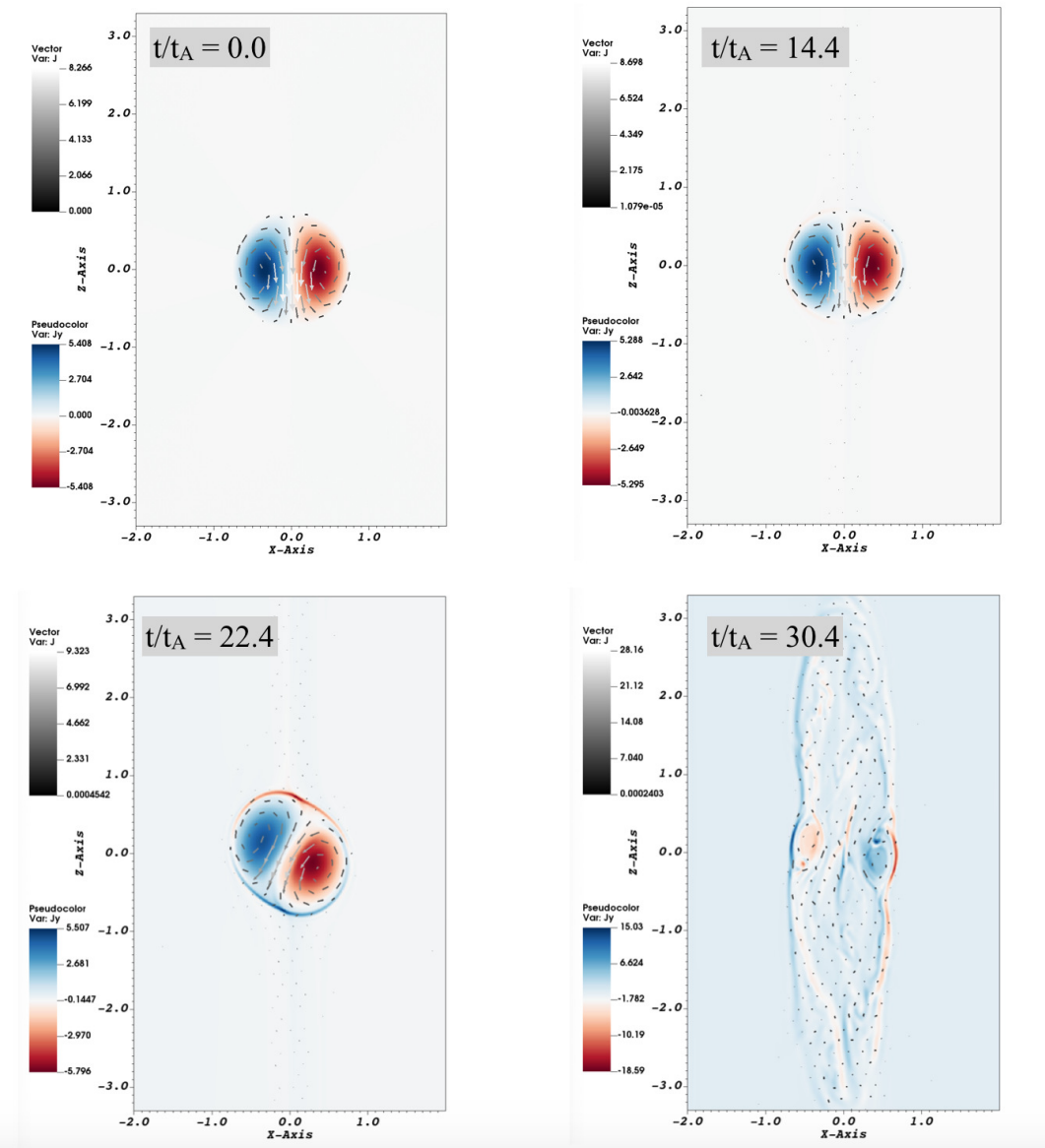

Figure 3.3. Same as figure 3.1 showing the value of the toroidal current density J_y (color) and vectors $\boldsymbol{J}$. The third panel clearly shows the formation of a surface current sheet as the spheromak rotates.

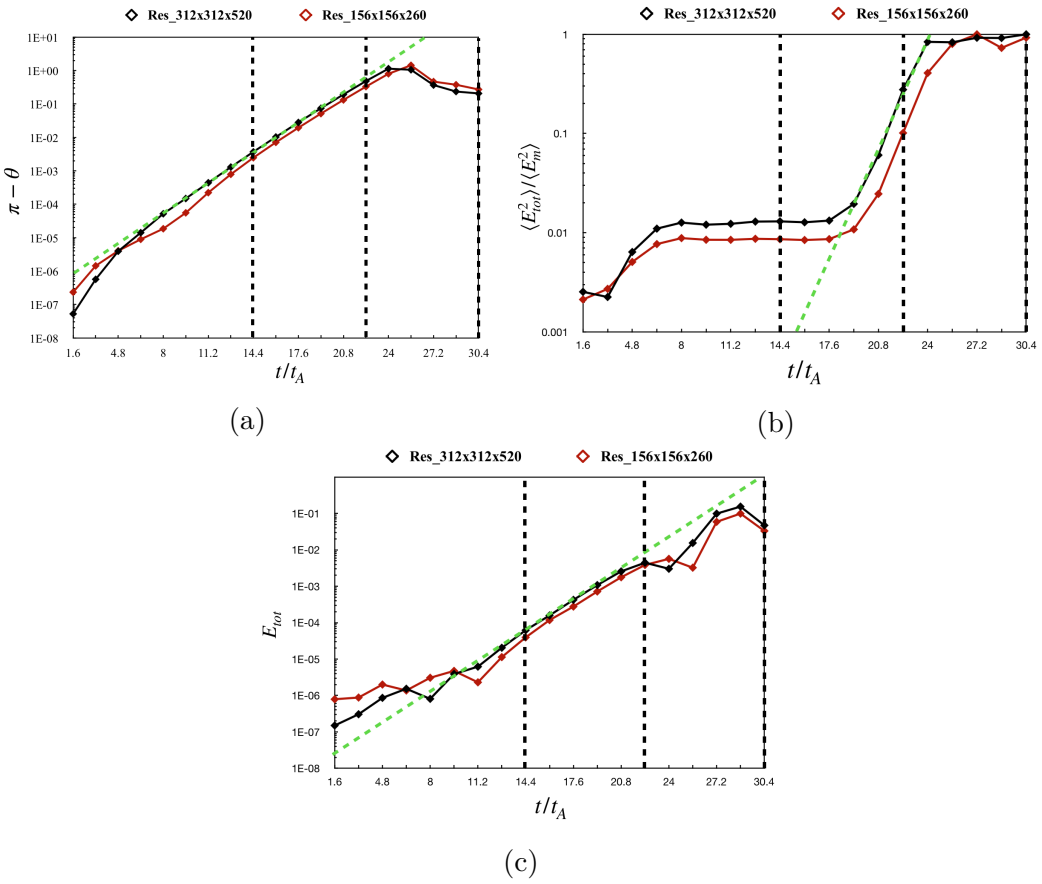

Figure 3.4. (a) Time evolution of the tilt angle θ in log-linear scale. (b) Time evolution of $\langle E_{tot}^2 \rangle / \langle E_m^2 \rangle$ in log-linear scale. (c) Time evolution of E_{tot} at the center of spheromak in log-linear scale. In all three, a clear phase of exponential growth can be seen (green dotted line). From the plots, $(\boldsymbol{\pi} - \theta) \propto \exp(0.64 v_A t/r_0)$, $\langle E_{tot}^2 \rangle / \langle E_m^2 \rangle \propto \exp(0.8 v_A t/r_0)$ and $E_{tot} \propto \exp(0.6 v_A t/r_0)$. The spheromak dissipates in $\sim 20 t_A$ over which instability grows linearly with a growth rate of $0.64/t_A$. Vertical dashed lines indicate the time snapshots used for figures 3.1 and 3.2.

squared of total electric field, $\langle E_m^2 \rangle$ is the maximum value of $\langle E_{tot}^2 \rangle$ and E_{tot} is the total electric field at the center of the spheromak. We choose to normalize the box-averaged squared of the total electric field by its maximum value in the box assuming the maximum value to remain constant for the duration of the simulation. This helps to visualize the behavior of electric field for both resolutions simultaneously. We also checked the behavior of the y component of electric field E_y at the spheromak's center and box-averaged $\langle E_y^2 \rangle$ and they show the same trend as E_{tot} at the center and box-averaged $\langle E_{tot}^2 \rangle$ respectively.

Panel 3.4a shows an initially anti-aligned spheromak with $\theta \approx \pi$ radians. For simulation (I), a straight line fit to the linear phase of the plot clearly depicts an exponential growth of instability within the spheromak from $t \simeq 5t_A$ to $t \simeq 24t_A$ where $\theta^{'} = (\pi - \theta) \propto \exp(0.64 v_A t/r_0)$. We can quantify the growth rate of tilting through an angle θ' by

$$\gamma_t = \frac{1}{\theta'}\frac{d\theta'}{dt} \tag{3.14}$$

giving $\gamma_t = 0.64/t_A$.

The timescale of dissipation of the spheromak is $\sim 20t_A$. Similar fits to the linear phase of panels 3.4b and 3.4c give $\langle E_{tot}^2 \rangle / \langle E_m^2 \rangle \propto \exp(0.8 v_A t/r_0)$ and $E_{tot} \propto \exp(0.6 v_A t/r_0)$. Here, we use three distinct measures to estimate the instability growth rate and it is seen that they are slightly different but consistent with each other. These results are also in good agreement with the analysis using PIC simulation, which will be shown in §3.3.6.

We also plot the time evolution of box-averaged total magnetic energy in terms of $\langle B_{tot}^2 \rangle / \langle B_m^2 \rangle$ and time evolution of rate of magnetic energy release for the two different resolutions. Here, $\langle B_{tot}^2 \rangle$ is the box-averaged squared of total magnetic field, $\langle B_m^2 \rangle$ is the maximum value of $\langle B_{tot}^2 \rangle$ and E_B is the magnetic energy in the box. Figure 3.5 shows that the results are independent of resolution. Panel 3.5a shows that about 30% of the total magnetic energy is dissipated from the box during the entire evolution of the spheromak from $t = 0$ to $t = 30.4t_A$. Interestingly, as shown in panel 3.5b, the rate of magnetic energy release stays almost constant during the exponential growth of instability.

For simulation (I), we can also estimate an initial magnetic flux in the xy plane by summing the value of the z component of magnetic field over an xy slice at $t = 0$; we find that it is smaller than the value of $B_0 \times N_x \times N_y$, the total magnetic flux in the box without an embedded spheromak. This is due to the fact that magnetic field lines effectively get pushed out of the simulation box once a spheromak is introduced. Thus, it is not very physical to track the time evolution of excess energy in the box (*e.g.* the difference between the total magnetic energy within the box in the presence of spheromak and energy in the constant magnetic field).

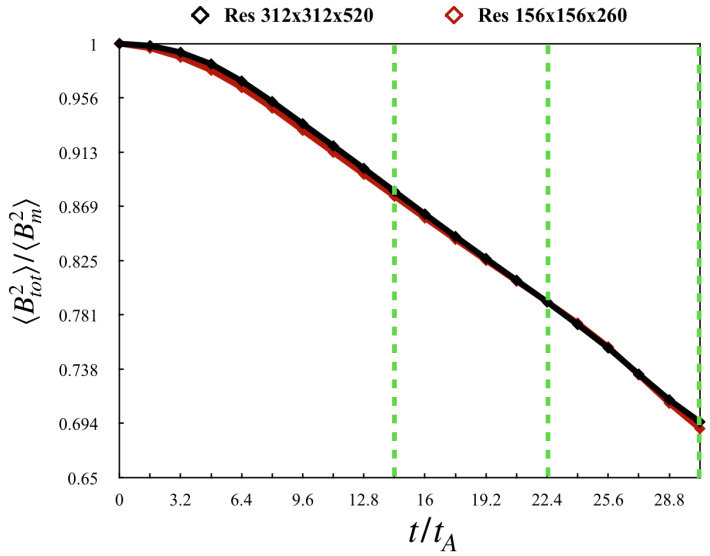

(a)

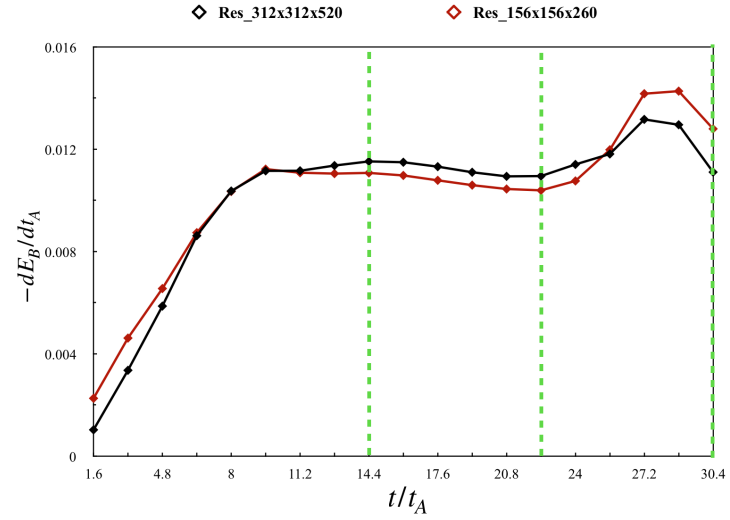

(b)

Figure 3.5. (a) Time evolution of box-averaged total magnetic energy for the two different resolutions. Total magnetic energy is plotted in terms of $\langle B_{tot}^2 \rangle / \langle B_m^2 \rangle$. About 30% of the initial magnetic energy in the simulation box is dissipated when the spheromak tilts and starts dissipating, eventually hitting the walls. (b) Time evolution of rate of magnetic energy release. Initially, there is a steady increase in the rate until $\simeq 8t_A$ after which magnetic energy is released at a constant rate throughout the duration of tilt instability growth. Green dashed lines indicate the time snapshots used for figures 3.1 and 3.2.

3.3.4 Qualitative picture of spheromak instability

The time evolution of lowest-energy Taylor state depicted through 3-D MHD simulations can be described qualitatively, see figure 3.6. Approximately, the spheromak first flips by 180°, and then reconnects the part of the magnetic flux counter to the external magnetic field.

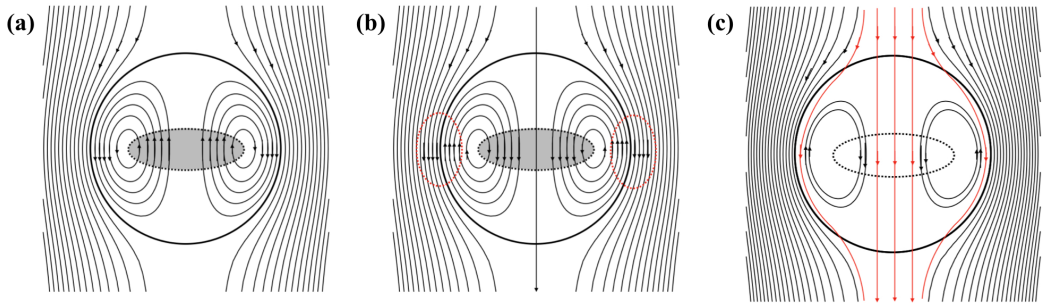

Figure 3.6. Qualitative evolution of tilting instability. Plotted are poloidal magnetic field lines in the xz plane. Initial spheromak (a) is unstable to tilting, so that the spheromak flips over (b), creating current sheets on the surfaces (highlighted in red-dashed lines). At the core the field inside the spheromak is aligned with the external field (grey circle in the center). Reconnection at the surface connects the internal field lines to the external field (c) - newly reconnected field lines are highlighted in red. At the same time the external field connects to the fields close to the center. At this stage there is a donut-shaped toroidal configuration with still counter aligned fields - this is clearly seen in simulations, last panels in figures 3.1 and 3.2.

Let us discuss the properties of the configuration after the spheromak flips, but before any substantial dissipation sets in. In the equatorial plane $\theta = \pi/2$, there exists a disk of radius $r_* = 2.74/\lambda$, defined by the condition $B_\theta = 0$ (it is depicted by the gray circle in the center of panels a, b in figure 3.6) within which all field lines point along the external field and whose boundary separates it from the region where the field lines are opposite to the external field. This poloidal magnetic field which is directed opposite to the external field constitutes a poloidal flux ψ_{opp} in the equatorial plane that would eventually reconnect with the external field. We estimate this flux using (3.5) in the following discussion.

The total poloidal flux through the spheromak is zero, $\int_0^{r_0} B_\theta 2\pi r dr = 0$, composed of two counter-aligned contributions at $r < r_*$ and $r > r_*$, each of value

$$\psi_{opp} = \int_0^{r_*} B_\theta 2\pi r dr = 2.26 B_0 r_0^2 \tag{3.15}$$

This is the amount of poloidal flux in the equatorial plane that reconnects and eventually dissipates. Panel (c) in figure 3.6 shows partial dissipation of spheromak where newly connected field lines are highlighted in red. At the same time external field connects to the fields close to the center. At this stage there is a donut-shaped toroidal configuration with still counter aligned fields. This is clearly seen in the last panels of 3-D MHD simulations of figures 3.1 and 3.2.

3.3.5 Evolution of the second-order spheromak

In addition to the lowest-energy Taylor state, we also simulated the second-order spheromak, corresponding to the second zero of the spherical Bessel function, $\lambda \approx 7.725/r_0$, see figure 3.7. This case can be thought of as an example of a twisted magnetic configuration (the inner core), confined by another twisted configuration (the outer shell).

In these simulations the size of the domain is $x \in [-2, 2]$, $y \in [-2, 2]$ and $z \in [-2, 2]$. Uniform resolution is used in the computational domain with total number of cells $N_{\rm X} = N_{\rm Y} = N_{\rm Z} = 520$. At time $\sim 7t_A$, the inner spheromak starts to get expelled from the outer one. By the time $\sim 9.6t_A$, the smaller inner spheromak almost totally disconnects from the outer spheromak; the density within it decreases considerably due to magnetic dissipation. After the expulsion of the inner core the two spheromaks evolve nearly independently, similar to the basic spheromak case.

Similar to the basic spheromak, we show the time evolution of box-averaged total magnetic energy in terms of $\langle B_{tot}^2 \rangle / \langle B_m^2 \rangle$ and time evolution of rate of magnetic energy release in figure 3.8. Panel 3.8a shows that about 23% of the total magnetic energy is dissipated from the box during the entire evolution of the 2-root spheromak from $t = 0$ to $t = 9.6t_A$. Panel 3.8b depicts that magnetic energy is released at an increasing rate throughout the evo-

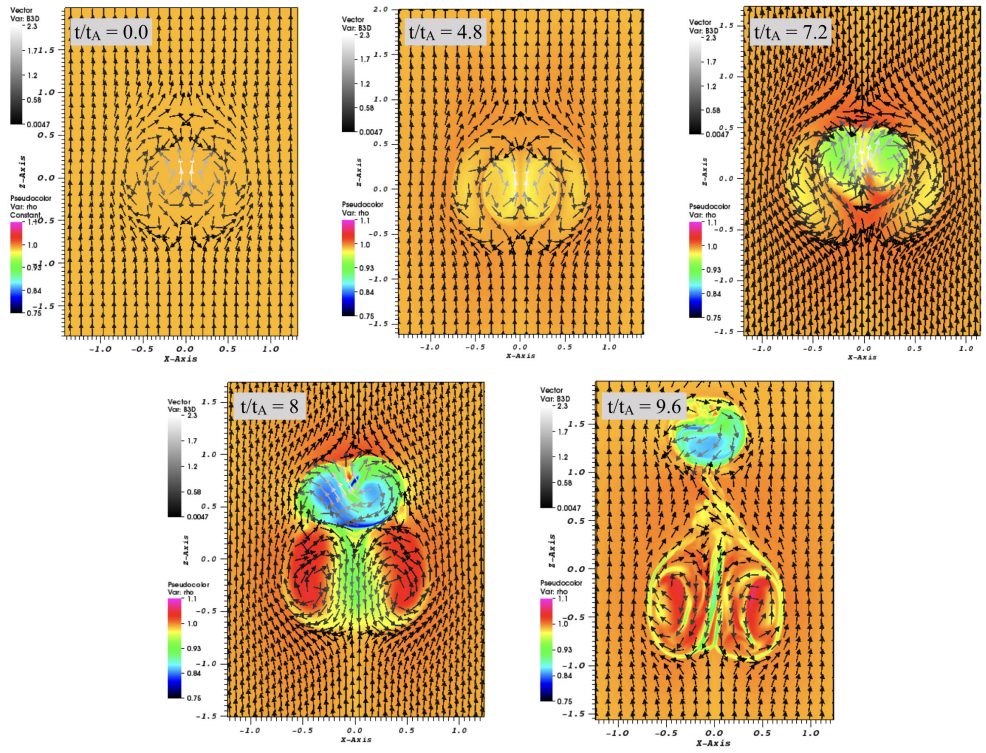

Figure 3.7. Slice in the xz plane of MHD simulation of 2-root spheromak with $\lambda \approx 7.725/r_0$. Times are indicated in the panels in units of the Alfvénic crossing time $t_A = r_0/v_A$. Colors indicate plasma density while vectors depict $\boldsymbol{B3D}$. The 2-root spheromak goes from being symmetrical to the inner spheromak almost totally detaching from the outer one in $\sim 9.6t_A$.

lution unlike the basic spheromak where there was a nearly flat phase during the instability growth.

3.3.6 PIC simulation of basic spheromak

We have supplemented our MHD simulations with PIC simulations performed with the 3-D electromagnetic PIC code TRISTAN-MP [83], [84]. We employ a 3-D cube with 1440 cells on each side, and periodic boundary conditions in all directions. The domain is initialized with a uniform density of cold electron-positron plasma, with 2 computational particles per cell. The skin depth $c/\omega_{\rm p}$ is resolved with 2.5 cells. The radius r_0 of the spheromak is $50\,c/\omega_{\rm p} = 125$ cells. The strength of the magnetic field B_0 is calibrated such that the

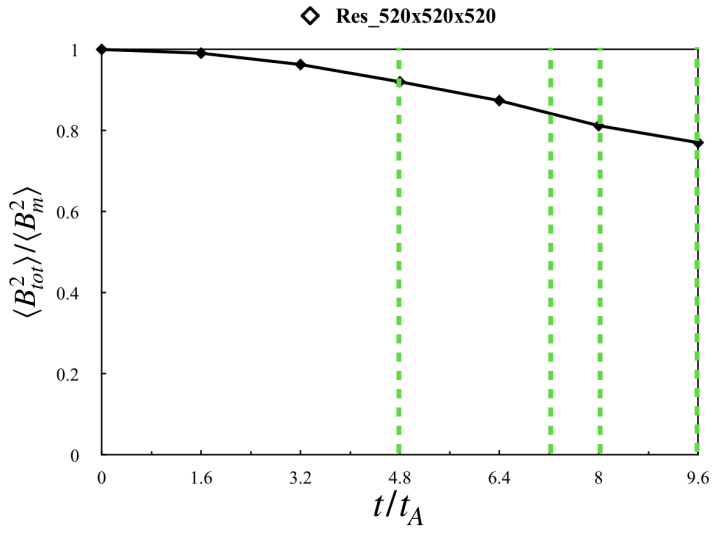

(a)

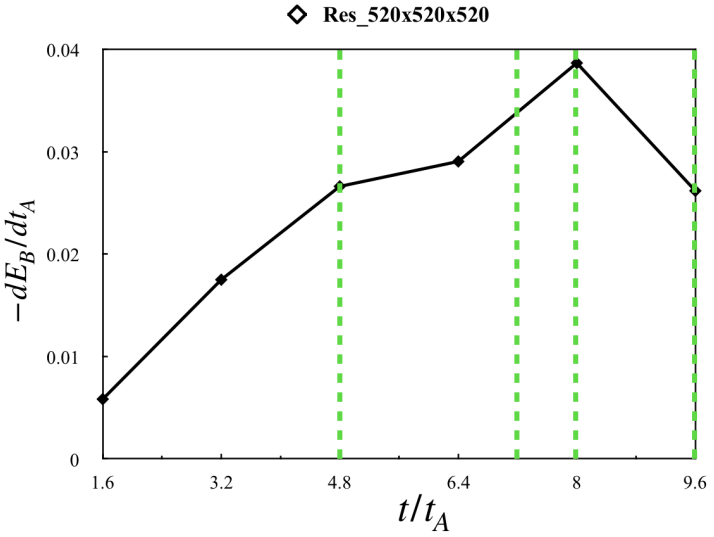

(b)

Figure 3.8. (a) Time evolution of box-averaged total magnetic energy in terms of $\langle B_{tot}^2 \rangle / \langle B_m^2 \rangle$. About 23% of the initial magnetic energy in the simulation box is dissipated when the 2-root spheromak goes from being symmetrical to the inner spheromak almost totally separating from the outer one. (b) Time evolution of rate of magnetic energy release. There is a gradual increase in the rate throughout the entire evolution. Green dashed lines indicate the time snapshots used for figure 3.7.

magnetization $\sigma = B_0^2/(4\pi n_0 mc^2) = 10$, where n_0 is the total particle density, m the electron (or positron) mass and c the speed of light. This implies that the Alfvén speed $v_A = c\sqrt{\sigma/(1+\sigma)} \simeq 0.95\,c$.

Figure 3.9 shows the evolution of the magnetic field B_y/B_0 in the xz plane passing through the center of the spheromak. Arrows represent the B_x and B_z components in that plane. The top left panel presents the initial state of the system. At early times (top right panel), the configuration is still close to the initial conditions, while at later times (bottom left panel) the spheromak starts to tilt, in analogy with the MHD simulations presented above. The final state of the system (bottom right panel) is also similar to the MHD results.

Further insight into the growth of the tilt instability is presented in figure 3.10, where we show the evolution of box-averaged $\langle E_y^2\rangle/B_0^2$, where E_y is the y-component of electric field. Vertical dashed lines indicate the time snapshots used for figure 3.9. A clear phase of exponential growth can be seen from $t/t_A \simeq 3$ to $t/t_A \simeq 6$, with an $\langle E_y^2\rangle$ growth rate $\simeq v_A/r_0$ (dotted line). We have checked that the growth rate scales as r_0^{-1} by performing a similar simulation with $r_0 = 75\,c/\omega_{\rm p}$. The measured growth rate of the instability is in agreement with that estimated from MHD simulations.

3.4 Discussion and conclusions

In this paper we consider the tilting instability of magnetically confined spheromaks using 3-D MHD and PIC simulations. We consider astrophysically important mildly relativistic regime, when the Alfvén velocity approaches the velocity of light. In addition to basic spheromak [78] we also consider a second-order spheromak, as an example of a magnetically twisted configuration (the inner core) confined by the magnetically twisted shell.

We find that in all cases confined spheromaks are highly unstable to tilting instabilities. The instability is driven by the fact that initially the magnetic moment of the spheromak is counter-aligned with the confining magnetic field. As a result the spheromak flips, indicative of a tilt instability. This creates current layers at the boundary. The resulting reconnection between internal and confining magnetic field leads to partial annihilation of the spheromak's poloidal magnetic flux with the external magnetic field. At the same time the toroidal

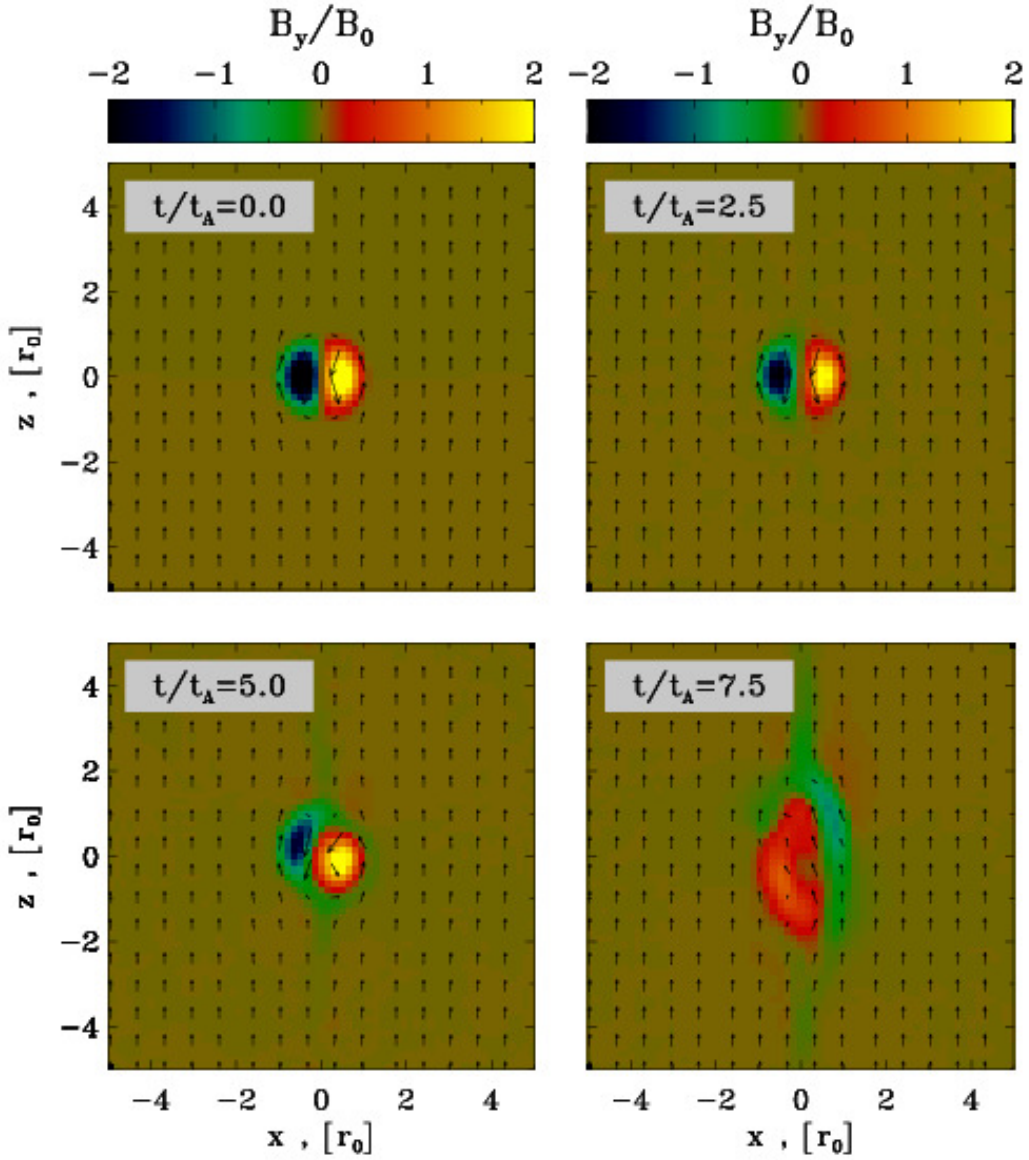

Figure 3.9. PIC simulation of the time evolution of the lowest-order Taylor state. Times are indicated in the panels in units of the Alfvènic crossing time $t_A = r_0/v_A$. Colors indicate the value of B_y/B_0 in the xz plane going through the center of the spheromak, while arrows indicate the B_x and B_z components.

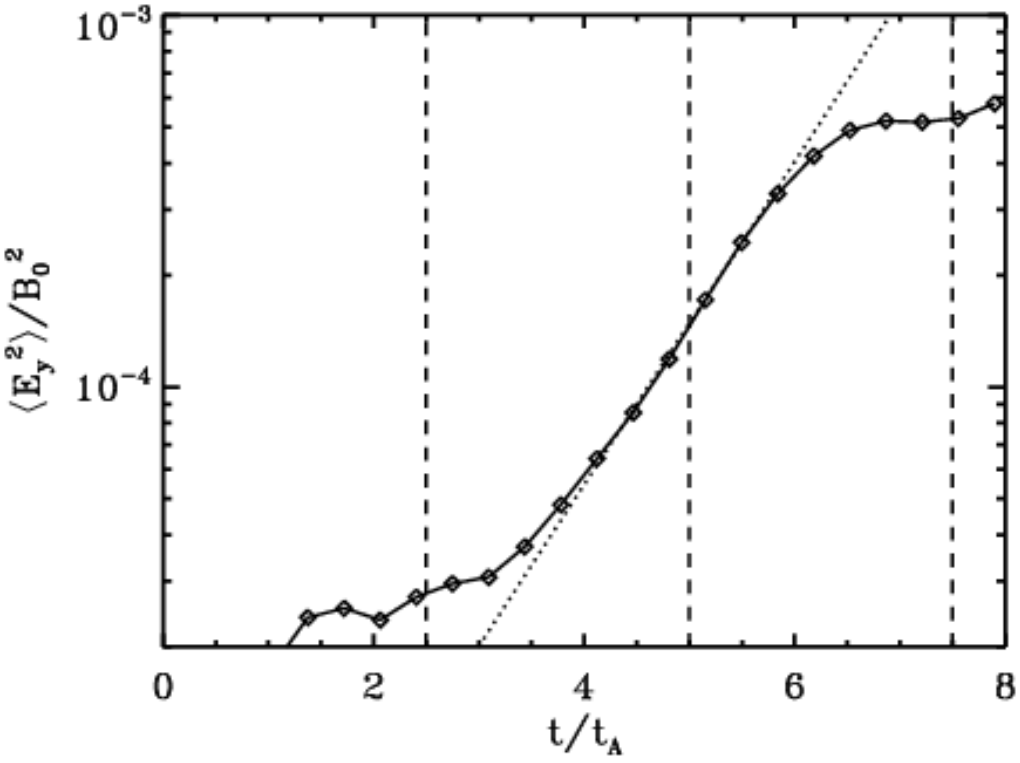

Figure 3.10. From the PIC simulation of the lowest order Taylor state, we show the time evolution of box-averaged $\langle E_y^2 \rangle / B_0^2$ in log-linear scale, where E_y is the y-component of electric field. Vertical dashed lines indicate the time snapshots used for figure 3.9. A clear phase of exponential growth can be seen from $t/t_A \simeq 3$ to $t/t_A \simeq 6$, with $\langle E_y^2 \rangle \propto \exp(v_A t/r_0)$ (dotted line).

magnetic field and the associated helicity (or relative helicity [28], [77]) of the initial configuration is carried away by torsional Alfvén waves (in a sense that initial configuration had finite helicity, while the eventual final configuration - just straight magnetic field lines - has zero helicity).

The evolution of the basic spheromak is generally consistent with previous results. The tilting instability of spheromak in cylindrical geometry has been explored by [74] and [75] where they analyze growth rate of tilting as a function of elongation L/R (see figure 4 in both) and derive a threshold value $L/R \approx 1.67$. For our case, $L/R = 2$ and growth rate of $0.64/t_A$ is consistent with the growth rates implied from their figure 4, namely $\sim 0.1/t_A$ [74] and $\sim 10/t_A$ [75]. An experimental identification of tilting mode of a spheromak plasma and its control is discussed in [85]. A clear exponential growth rate of tilting is visible in their figure 1 and is strikingly similar to our panel 3.4a.

A characteristic timescale of tilting instability is $\simeq 20t_A$ during which the spheromak dissipates after losing a significant fraction of its energy which is in good agreement with [71] where they study spheromak dynamics for a force-free plasma by a 3-D MHD code and estimate a growth rate of the order of $10t_A$. Interestingly, their results also show that the tilting angle saturates at 90° unlike our results where the spheromak almost entirely undergoes a 180° rotation - it flips. The 90° tilt stabilization of [71] is facilitated by a cylindrical vacuum vessel - a toroidal flux core having a small enough aspect ratio so that further tilting is energetically unfavorable [28]. A similar characteristic growth time of tilt around the magnetic axis and use of a flux conserver to stabilize the tilt mode is suggested in [77] which also provides an excellent review on formation and stability of spheromaks.

We have also studied the evolution of second-order magnetically confined spheromak as an example of a configuration (the inner core) confined by the twisted magnetic field (the outer shell). Very quickly ($\sim 10t_A$) the inner core separates from the outer shell and completely detaches. As a result two nearly independent dissipative structures are formed. No stabilization occurs.

Our results disfavor models of magnetically confined structures for the origin of tail oscillations in magnetar flares [67], [70], as we discuss next. Magnetars are young ($\sim 10^3 - 10^4$ years) and highly magnetized (surface magnetic fields $\sim 10^{14} - 10^{15}$ G) neutron stars

exhibiting X-ray and γ-ray activity. The most dramatic giant flare to date was exhibited by SGR 1806-20 on December 27, 2004 [9], [10] in which the main spike that lasted ~ 0.5 seconds was followed by a $\sim$ 380 s pulsating tail. This is $\sim$ 50 cycles of high-amplitude pulsations at the SGR's known rotation period of 7.56 s. The long pulsating tails of giant flares originate in a 'trapped fireball' that remains confined to the star's closed magnetic field lines.

In magnetar magnetospheres, the Alfvén speed through a plasma of density ρ is nearly relativistic [86]:

$$\frac{v_A}{c} = \left(\frac{B^2/4\pi}{\epsilon + P + B^2/4\pi} \right)^{1/2} \approx 1 \tag{3.16}$$

c is the speed of light, $\epsilon = \rho c^2$ is the total energy density of plasma particles and P is the total plasma pressure. For a magnetically dominated plasma, $P, \epsilon << B^2/4\pi$. Thus, the Alfvén time within the magnetar's magnetosphere

$$t_A = \frac{R_{NS}}{v_A} \approx 3 \times 10^{-5}\text{s} \tag{3.17}$$

where $R_{NS} = 10$ km is the radius of a neutron star. Our results demonstrate that stabilization even of higher order spheromaks does not occur, so that the timescale over which a spheromak confined in the magnetar's magnetosphere would dissipate is too short to explain the tail duration

$$t_{\text{diss}} \sim 20 t_A \approx \times 10^{-3}\text{s} \tag{3.18}$$

Finally, let us comment on the applicability of the Taylor relaxation principle to astrophysical plasmas. It was suggested in [65] that a spheromak is a Taylor state, so that the evolution of the system will lead to the largest possible spheromak. The Taylor relaxation principle assumes that the plasma is surrounded by a wall impenetrable to helicity escape. This can be achieved in a laboratory, with arrangements of conducting walls. This is not possible in astrophysical surrounding as we argue next.

First, according to Shafranov's virial theorem (*e.g.,* [87]) it is not possible to have an isolated self-contained MHD equilibrium - there must always be some external confining structure. It is possible to have purely unmagnetized external confining structures - one can construct spheromak-type configurations confined by external pressure [29]. The configurations considered by [29] are not force-free, but they look very similar to spheromaks. They are stable to current-driven instabilities. It seems the case considered by [29] is the only case when Taylor relaxation principle would be applicable to astrophysical plasmas - if there is non-zero magnetic field in the confining medium the spheromak will try to flip and will reconnect. This will generally happen very fast, on few Alfvén time scales. The helicity will then be emitted as Alfven shear waves; this then violates the Taylor principle of conserved helicity.

Thus, astrophysical magnetic configurations belong more naturally to a class called 'driven magnetic configurations' by [28] - they are generally magnetically connected to some outside medium. As a result of this connection helicity will leave the system in the form of torsional Alfven waves. This will violate the assumptions of Taylor relaxation scheme.

We explore a possible astrophysical application of our numerical results. Using the energetics of SGR 1806-20, the estimated dissipation timescale of a magnetically confined spheromak is of the order of a milli second, whereas the quasi-periodic oscillations in the SGR's giant flare release energy for ~ 400 s. The formation and spontaneous dissipation of a spheromak in a magnetar's magnetosphere doesn't allow for such prolonged energy release. It would be worthwhile to explore coalescence instability in turbulent plasmas. It has been suggested by [88] that by Taylor's theory, repeated coalescence of n spheromaks of equal size increases the radius of the spheromak by a factor of $n^{1/4}$ whereas the total magnetic energy of the final spheromak will be $n^{-1/4}$ times the sum of the energies of the initial spheromaks. We speculate that such a mechanism might stabilize the spheromak over longer timescales. Another important investigation would be to look for effects of plasma rotation on the tilt mode stability in the context of a spheromak using arguments similar to those made by [89]–[91] who show that plasma rotation in the θ direction can help stabilize the tilt mode, but in field-reversed configurations (FRCs). Finally, it would serve useful to explore if both,

coalescence and rotation together could have stabilizing effects to sustain a spheromak over longer timescales.

Acknowledgements

We thank the anonymous referee for their constructive comments which greatly improved the manuscript. The numerical simulations were carried out in the CFCA cluster of National Astronomical Observatory of Japan. We thank the *PLUTO* team for the possibility to use the *PLUTO* code and for technical support. Visualization of results was performed in the VisIt package. We would like to thank P. Bellan, E. Blackman and O. Porth for discussions and comments on the manuscript. This work had been supported by NASA grant 80NSSC17K0757 and NSF grants 1903332 and 1908590. L.S. acknowledges support from the Sloan Fellowship, the Cottrell Scholars Award, and NSF PHY-1903412.

4. SUMMARY and CONCLUSIONS

This dissertation presents the work on two astrophysical problems that I investigated over the course of three years. The focus of my research was to study high-energy and radio emissions from magnetar GFs, specifically those associated with the GF from SGR 1806-20, and hypothesize their causes using numerical analysis facilitated by the *PLUTO* code. In this chapter, I summarize the main results and conclusions of my research and describe future prospects.

To investigate the radio afterglow from the 27 December, 2004 giant flare from SGR 1806-20, I considered the interaction of light, magnetically dominated cloud (CME) ejected during the magnetar flare, with the surrounding ISM. I identified the observed emission features with the forward shock created by the impact. The magnetic blob is first advected with the magnetar wind, and later impacts on the ISM. The impact creates a forward shock, and a complicated backward flow. The overall dynamics has intermediate self-similarity, that is, between energy conserving and momentum conserving regimes. I identified a number of magnetohydrodynamic features of the interaction that can contribute to particle acceleration and the production of radio emission: (i) reconnection between the CME's and ISM's magnetic field; (ii) forward shock generated in the ISM; (iii) reverse shock in the CME, and (iv) shocks in the exhaust flow of the ISM. Relative importance of these contributions is expected to depend mostly on the parameters of the CME.

To compare with observations, I employed two prescriptions to connect MHD properties with radio emissivity: pure compression of magnetic field, as well as turbulent amplification. Observations are complicated, showing somewhat different evolution at different frequencies and changing temporal behavior. However, considering the simplicity of the MHD model and the complications involved in quantifying radio synchrotron emission, the analysis with field amplification produces a light curve ($\sim t^{-0.7}$) closer to the observed temporal evolution of the GF's radio emission ($\sim t^{-1.1}$) in the self-similar phase, as well as consistent with observations of radio emission from other SNRs. This, in turn, could mean that field amplification might indeed play a significant role in radio afterglow from magnetar GFs. An interesting feature of the observed radio light curve is rebrightening at ~ 25 days when the radio flux increases

by a factor of ~ 2. A scenario with a pre-existing shell around the SGR has been previously invoked to explain this flux increase when the emission from swept-up material dominates the light curve. We test this hypothesis through our MHD simulation. Although the presence of a dense shell produces a break in the temporal evolution of flux, there was no evidence of rebrightening in the light curve due to the impact of the magnetic cloud on the shell. Interestingly, the late-time light curve with only magnetic field compression ($\sim t^{-1}$) does better at accounting for observations, if the shell scenario were to be accepted.

Several prospects can be explored in the future. In this study, interaction of the magnetic blob with a constant-density ISM/shell was considered. It would be worthwhile to explore a broader parameter space for the blob and ISM. For example, interaction between the blob and an ISM with varying density profiles such as a $\rho \propto r^{-2}$ or an exponential profile can be analyzed. In addition, effects of a denser or a larger/smaller blob can be tested. Emissivity maps and light curves can be calculated for both prescriptions, and compared with theoretical estimates for Sedov remnants as discussed by [40] as well as with the observed light curve. This exercise can provide a better understanding about the nature of the outflow ejected by the SGR flare and its astrophysical environment.

Secondly, a better investigation of the effect of a pre-existing shell around the SGR can be performed by testing the MHD code in different regimes with multiple combinations of relative shell thickness and density. It is expected that rebrightening might be observed in some regimes over and above the break in the light curve. Lastly, implications of synchrotron self-absorption on the integrated emissivity maps and light curves, an important consideration in radio, should be explored carefully to gain a more accurate understanding of the nature of the radio nebula.

To investigate the QPOs in the tail of the 27 December, 2004 giant flare from SGR 1806-20, I considered the tilting instability of magnetically confined spheromaks using 3-D MHD and PIC simulations, with an application to astrophysically important mildly relativistic regime, when the Alfvén velocity approaches the velocity of light. In addition to basic spheromak, I also considered a second-order spheromak, as an example of a magnetically twisted configuration (the inner core) confined by the magnetically twisted shell. It was seen that in all cases, confined spheromaks are highly unstable to tilting instabilities.

The instability, driven by the fact that initially the magnetic moment of the spheromak is counter-aligned with the confining magnetic field, causes the spheromak to flip, indicative of a tilt instability. This creates current layers at the boundary. The resulting reconnection between internal and confining magnetic field leads to partial annihilation of the spheromak's poloidal magnetic flux with the external magnetic field. Evolution of the basic spheromak was found to be generally consistent with previous results and a characteristic timescale of tilting instability was estimated to be $\simeq 20t_A$ during which the spheromak dissipates after losing a significant fraction of its energy. Furthermore, analysis of the evolution of second-order magnetically confined spheromak as an example of a configuration (the inner core) confined by the twisted magnetic field (the outer shell) reveals that very quickly ($\sim 10t_A$) the inner core separates from the outer shell and completely detaches. As a result two nearly independent dissipative structures are formed without stabilization.

Application of the results of numerical analysis of tilting instability of magnetically confined spheromaks to the specific case of the SGR 1806-20 GF, led to the conclusion that such structures, having a dissipative timescale of $\sim 20t_A \sim 1$ ms in the magnetar magnetosphere, cannot be the origin of the $\sim$ 400 s long QPOs in the tail of the GF. The formation and spontaneous dissipation of a spheromak in a magnetar's magnetosphere doesn't allow for such prolonged energy release. It would be worthwhile to explore coalescence instability in turbulent plasmas. It has been suggested that by Taylor's theory, repeated coalescence of n spheromaks of equal size increases the radius of the spheromak by a factor of $n^{1/4}$ whereas the total magnetic energy of the final spheromak will be $n^{-1/4}$ times the sum of the energies of the initial spheromaks. I speculate that such a mechanism might stabilize the spheromak over longer timescales. Another important investigation would be to look for effects of plasma rotation on the tilt mode stability in the context of a spheromak because it is known that plasma rotation in the θ direction can help stabilize the tilt mode in field-reversed configurations (FRCs). Finally, it would serve useful to explore if both, coalescence and rotation together could have stabilizing effects to sustain a spheromak over longer timescales.

A. RADIO AFTERGLOW OF MAGNETARS' GIANT FLARES

A.1 Analytical Model: The Grad-Shafranov equation and its solution

In MHD equilibria, the Lorentz force is balanced by the pressure gradient hence demanding

$$\nabla p = \boldsymbol{J} \times \boldsymbol{B} \tag{A.1}$$

where p is plasma pressure, and $\boldsymbol{J}$ and $\boldsymbol{B}$ are current density and magnetic field.
In the Grad–Shafranov framework [79], [80] the magnetic field can be represented by a scalar flux function ψ in spherical coordinates

$$\boldsymbol{B} = \nabla\psi \times \nabla\phi + \lambda\psi\nabla\phi \tag{A.2}$$

Force balance A.1 gives the Grad-Shafranov equation

$$\frac{\partial^2\psi}{\partial r^2} + \frac{\sin\theta}{r^2}\frac{\partial}{\partial\theta}\left(\frac{1}{\sin\theta}\frac{\partial\psi}{\partial\theta}\right) + F(\psi)r^2\sin^2\theta + G(\psi) = 0 \tag{A.3}$$

where $F(\psi) = 4\pi dp/d\psi$.

We model the radio emission as a CME, using the magnetic field structure of [29], namely a structure demanding vanishing magnetic field on the surface due to unmagnetized external plasma. We will call this the 'magnetic blob' henceforth. This mathematical problem requires both Dirichlet and Neumann boundary conditions to be satisfied, meaning both the flux function ψ and its normal derivative $\partial_r\psi$ should be continuous at the boundary. Following [29], for solutions of A.3 of desired properties, $F(\psi) = 4\pi dp/d\psi = F_0$ and $G(\psi) = \lambda^2\psi$ are chosen. This choice along with $\psi = \sin^2\theta f(r)$ leads to the analytical solution for the radial part of ψ

$$f(r) = A_0\lambda r \mathrm{j}_1(\lambda r) - \frac{F_0}{\lambda^2}r^2 \tag{A.4}$$

where $\mathrm{j}_1(\lambda r) = \frac{\sin(\lambda r)}{\lambda^2 r^2} - \frac{\cos(\lambda r)}{\lambda r}$ is the spherical Bessel function.

Thus, it is observed that the solution is simply a force-free spheromak superposed with a uniformly twisted magnetic field

$$\psi = \sin^2\theta \left(A_0 \lambda r \mathrm{j}_1(\lambda r) - \frac{F_0}{\lambda^2} r^2 \right) \tag{A.5}$$

Next, we determine the normalizing constant A_0. We consider the flux to be confined within a structure of radius r_0 which can take several values unlike [29] where they consider a unit radius. This enables us to write all following equations in terms of r_0, giving the flexibility of testing the code for radius dependence, if desired. The first boundary condition of zero magnetic field on the surface $f(r_0) = 0$ gives

$$F_0 = \frac{A_0 \lambda^3}{r_0} \mathrm{j}_1(\lambda r_0) \tag{A.6}$$

The second boundary condition of zero surface currents $f'(r_0) = 0$ gives

$$\tan(\lambda r_0) = \frac{3\lambda r_0}{3 - \lambda^2 r_0^2} \tag{A.7}$$

The smallest positive root of this equation is $\lambda \approx 5.763/r_0$ giving $F_0 = -31.7 A_0 / r_0^4$. Magnetic field components are

$$B_r = \frac{2\cos\theta}{r^2} f(r) \tag{A.8}$$

$$B_\theta = -\frac{\sin\theta}{r} f'(r) \tag{A.9}$$

$$B_\phi = \frac{\lambda \sin\theta}{r} f(r) \tag{A.10}$$

Since the blob is held together by magnetic field, pressure profile within the sphere in pressure balance with the ambient medium having pressure p_0 can be given as

$$p = p_0 + \frac{F_0 \psi}{4\pi} = p_0 - \frac{B_{\max}^2}{8\pi} \tag{A.11}$$

where $B_{\rm max}$ is the maximum pressure at the center of the sphere. Defining a plasma-β as $\beta = p_0/B^2_{\rm max}$ along with maximizing $f(r)$ and using the value of F_0, gives the normalizing constant

$$A_0 = 0.11\sqrt{\frac{p_0}{\beta}}r_0^2 \tag{A.12}$$

As seen from A.11, there is a dip in pressure at the center of the blob. This dip is determined by $B_{\rm max}$ and hence β. To prevent negative pressure at the center, $\beta > 0.5$. Thus, initial magnetic field within the blob used to model the radio emission is completely defined by its initial radius, initial plasma-β and pressure of the ambient medium.

A.2 Effect of a pre-existing shell around SGR 1806-20

As a neutron star moves through the ISM with supersonic velocity, the interaction of the wind with the ISM creates a bow shock [27], [60]. Post-shock ISM can be approximated as a dense shell. [16], [17], [19] suggested the interaction of the material ejected during the GF with this pre-existing shell at $\sim 10^{16}$ cm as a possible cause for the rebrightening at ~ 25 days. To test this suggestion we run a long, low-resolution simulation with the dense shell added to the ISM as shown in figure A.1.

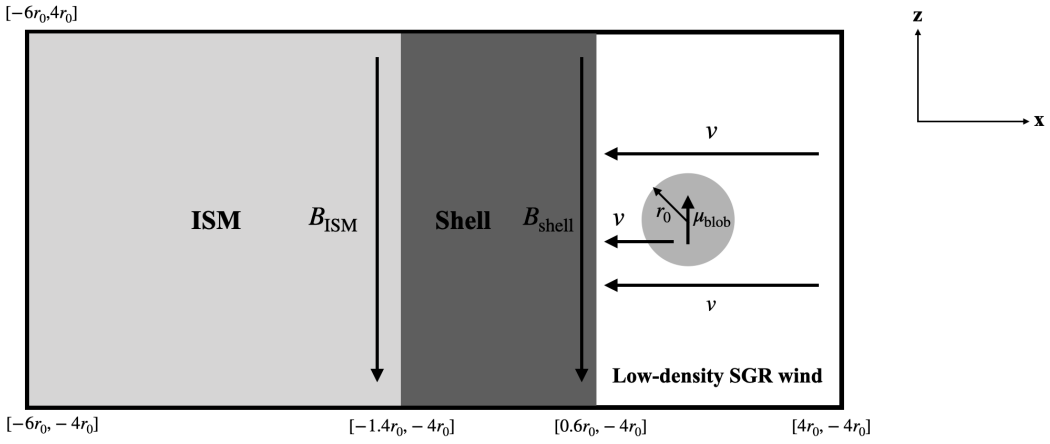

Figure A.1. A schematic of the anti-parallel set-up used to assess the effect of a pre-existing shell around the SGR on the shock dynamics.

The initial parameters of the blob, ISM, SGR wind, and the normalizing values are the same as described in section 2.3.2 along with shell pressure $p_{\rm shell} = p_{\rm ISM}$, shell density $\rho_{\rm shell} = 4\rho_{\rm ISM}$, and shell magnetic field $\boldsymbol{B}_{\rm shell} = 4\boldsymbol{B}_{\rm ISM}$. The size of the domain is $x \in [-6r_0, 4r_0]$, $y \in [-4r_0, 4r_0]$ and $z \in [-4r_0, 4r_0]$ where r_0 is the radius of the blob. Uniform resolution is used throughout the computational domain with total number of cells $N_{\rm X} = N_{\rm Y} = N_{\rm Z} = 128$. The ISM extends from $-6r_0$ to $-1.4r_0$, shell size $= 2r_0$ extending from $-1.4r_0$ to $0.6r_0$, and low-density cavity extends from $0.6r_0$ to $4r_0$ along the x direction. We capture the dynamics of the interaction of the magnetic blob with the thick, dense shell and then the ISM from $t = 0$ to $t = 30$. Results of the simulation - synthetic synchrotron emissivity maps and light curves are depicted in figure A.2.

Following our procedure outlined in section 2.5, we employ the two models of [40] to create synthetic synchrotron emissivity maps in the presence of a pre-existing shell. The left and right panels of panel A.2a are 2-D (xz plane) projections of map1 and map2 of synchrotron emissivity scaled as $p^{1.875}$ and $pB^{1.75}$, respectively, at $t = 30$. The dependence of emissivity on magnetic field in the right panel (no magnetic field amplification, only compression) causes the shock to be significantly weaker than the left panel scaling only with pressure (magnetic field amplification) as it emerges out of the shell, indicating that the shell might play an important role at times much longer than the shock's shell-crossing time.

We show synthetic light curves for both models in panel A.2b from $t = 5$ to $t = 30$ in steps of 0.5 in log-log scale - red dots are numerical results for the box-summed normalized $p^{1.875}$ model and blue squares are numerical results for the box-summed normalized $pB^{1.75}$ model. It is clear that the late-time evolution of emissivities undergoes a break compared to early times as we show by fitting broken power laws to both light curves.

The light curve for the case of magnetic field amplification, $L_{\nu,\rm map1} \propto p^{1.875}$ can be fit with three power laws: at early times $\sim 2 < t < 8.5$, the blob's interaction with the dense shell is characterized by a steep decay in emissivity $\sim t^{-1.2}$, followed by an even steeper decay $\sim t^{-1.7}$ between $t = 9$ to $t = 20.5$ as the shock propagates through the shell and finally breaks out. At late times $t > 20$, as effects of the shell weaken after the shock crosses the shell, emissivity undergoes a shallow decay, approaching a steady time evolution $\sim t^{-0.3}$.

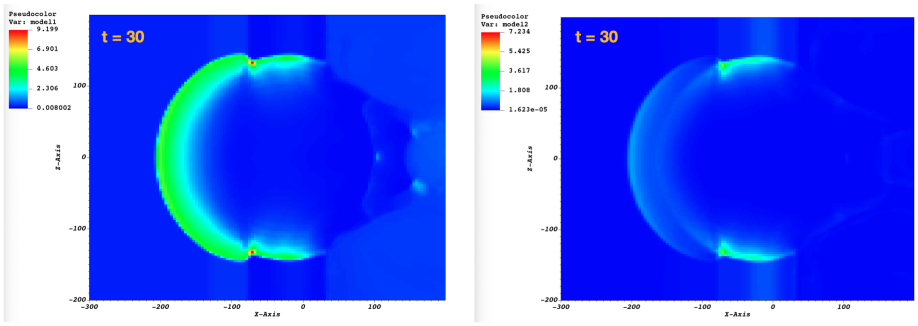

(a)

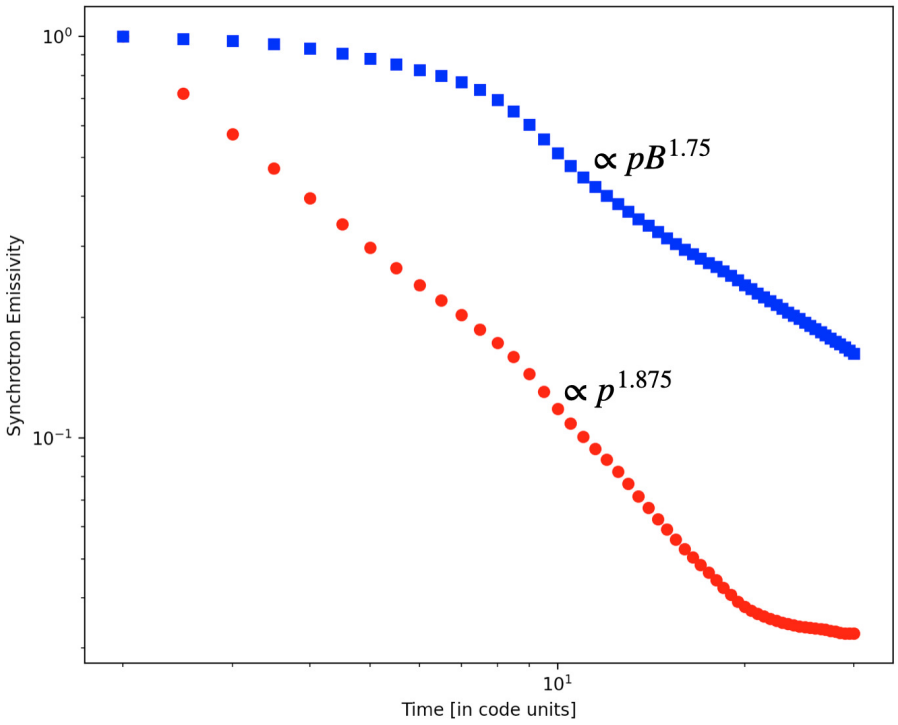

(b)

Figure A.2. Interaction of a magnetic blob with the shell in the ISM. (a) Slices in the xz plane of the low-resolution MHD simulation of the interaction of radio blob with a dense shell and then ISM at $t = 30$. Colors in the left panel indicate map1 of synchrotron emissivity defined as $\propto p^{1.875}$ and those in the right panel indicate map2 of synchrotron emissivity defined as $\propto pB^{1.75}$. (b) Normalized synthetic light curves for the two maps in log-log scale. The light curve with magnetic field amplification (red dots) undergoes two breaks and can be fit with three power laws, whereas the light curve with only magnetic field compression and no amplification (blue squares) undergoes a single break and can be fit with two power laws (see appendix A.2 for details).

The light curve for the case of magnetic field compression and no amplification, $L_{\nu,\mathrm{map2}} \propto pB^{1.75}$ undergoes only a single break and can be fit with two power laws: at early times $\sim 2 < t < 7$, the blob's interaction with the magnetic field of the dense shell is characterized by a shallow decay in emissivity $\sim t^{-0.2}$, followed by a steep decay $\sim t^{-1}$ at late times $t > 7$ as the shock breaks out after crossing the shell and becomes significantly weaker. It is clear that effect of magnetic field is important and causes the shell to play a dominant role in the evolution of synchrotron emission.

Our analysis of the shock dynamics in the presence of a pre-existing shell indicates that although the shell might produce a break in the radio synchrotron emission at the shock's shell crossing time, it does not account for rebrightening as reported in observations. At very late times, we expect the effects of shell to taper down significantly, thus causing the light curves to evolve similarly as the case without a shell. The shell might cause rebrightening in some regime with the appropriate shell thickness, density, and magnetic field. Hence, we are unable to conclusively eliminate this possibility. Investigation of appropriate regimes and shell parameters that might cause a flux increase can be a subject for future work.

B. STRUCTURE OF SPHEROMAKS

B.1 Spheromak: A magnetically confined force-free configuration

Astrophysical plasmas like those found in magnetar magnetospheres filled with highly relativistic electron-positron pairs, are likely to evolve in to a force-free configuration, effectively confined through the creation of a system of nested poloidal flux surfaces. Such a configuration arising from plasma self-organization and representing a minimum energy state is a spheromak as shown in figure B.1, described by [64]. The formation of spheromaks can be explained from the MHD viewpoint wherein confinement of plasma involves balancing the

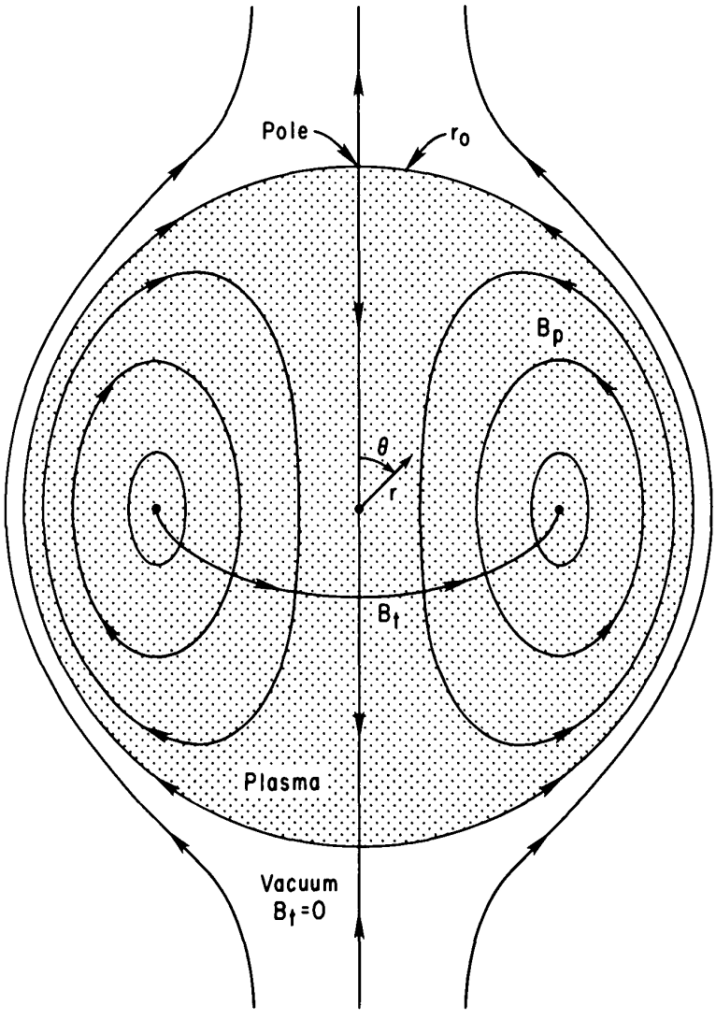

Figure B.1. A classical spheromak as described in [64]

outward force of hydrodynamic pressure called the hoop force arising due to the repulsion between oppositely directed currents on a toroidal current loop against the inward force due to interaction between magnetic fields and electric currents in plasma. Given the appropriate initial conditions, spheromaks can form spontaneously due to plasma instabilities and hence can be hypothesized to form in magnetar magnetospheres.

Consider a plasma with given boundaries and a given value for the integral $K = \int \boldsymbol{A}.\boldsymbol{B}dV$ within a given volume dV. $\boldsymbol{A}$ is the vector potential associated with the magnetic field $\boldsymbol{B}$ as $\boldsymbol{B} = \nabla \times \boldsymbol{A}$. K is called the magnetic helicity. It describes the degree of twistedness of magnetic field lines. The minimum energy state for a magnetic field can then be shown to conserve K and can be described by the force-free configuration [65]

$$\begin{aligned} \boldsymbol{J} \times \boldsymbol{B} &\approx 0 \\ \nabla \times \boldsymbol{B} &= \lambda \boldsymbol{B} \end{aligned} \tag{B.1}$$

where, λ is a spatially invariant constant.

The spheromak [64] is an axisymmetric solution of B.1 within a sphere of radius r_0. For such a configuration the magnetic field can be represented by a scalar flux function ψ in spherical coordinates [65]

$$\boldsymbol{B} = \nabla\psi \times \nabla\phi + \lambda\psi\nabla\phi \tag{B.2}$$

Using B.1 and B.2, the Grad-Shafranov equation (GSE) of axisymmetric force-free toroidal plasma equilibrium can be represented in spherical coordinates [81] as

$$r^2 \frac{\partial^2\psi}{\partial r^2} + \sin\theta \frac{\partial}{\partial\theta}\left(\frac{1}{\sin\theta}\frac{\partial\psi}{\partial\theta}\right) + (\lambda r)^2\psi = 0 \tag{B.3}$$

Equation B.3 can be solved using variable separation such that $\psi(r,\theta) = R(r)\Theta(\theta)$ and letting $x = \cos\theta$ and $n(n+1)$ as the separation variable. This gives

$$(1-x^2)\frac{\partial^2\Theta(x)}{\partial x^2} + n(n+1)\Theta(x) = 0 \tag{B.4}$$

$$r^2\frac{\partial^2 R(r)}{\partial r^2} + ((\lambda r)^2 - n(n+1))R(r) = 0 \tag{B.5}$$

With n = 1, $\Theta(x) = (1-x^2) = \sin^2\theta$ and $R(r) = A_0\lambda r \mathrm{j}_1(\lambda r)$. Thus,

$$\psi(r,\theta) = (A_0\lambda r \mathrm{j}_1(\lambda r))\sin^2\theta \tag{B.6}$$

where, $\mathrm{j}_1(\lambda r)$ is the spherical Bessel function of first order.
Using B.2 and B.6, the components of magnetic field are therefore

$$\left.\begin{aligned} B_r &= 2A_0\frac{\lambda}{r}\mathrm{j}_1(\lambda r)\cos\theta \\ B_\theta &= -A_0\frac{\lambda}{r}\frac{\partial}{\partial r}(r\mathrm{j}_1(\lambda r))\sin\theta \\ B_\phi &= A_0\lambda^2\mathrm{j}_1(\lambda r)\sin\theta \end{aligned}\right\} \tag{B.7}$$

Figure B.2 depicts B_r, B_θ and B_ϕ as functions of λr. Defining $x \equiv \lambda r$, B_r varies as $\frac{\mathrm{j}_1(x)}{x}$, B_θ varies as $\frac{1}{x}\frac{\partial}{\partial x}(x\mathrm{j}_1(x)) = \mathrm{j}_0(x) - \frac{\mathrm{j}_1(x)}{x}$ and B_ϕ varies as $\mathrm{j}_1(x)$.

The radial and toroidal components of magnetic field vanish on the surface of the spheromak which corresponds to $\mathrm{j}_1(\lambda r) = 0$ at $r = r_0$. Thus, λr_0 must be a root of j_1. The smallest allowed λ corresponds to the lowest energy state and since the smallest finite root of j_1 is 4.493, the Taylor state has

$$\lambda \approx 4.493/r_0 \tag{B.8}$$

Outside the spheromak, B_ϕ=0. Hence, the GSE becomes

$$r^2\frac{\partial^2\psi}{\partial r^2} + \sin\theta\frac{\partial}{\partial\theta}\left(\frac{1}{\sin\theta}\frac{\partial\psi}{\partial\theta}\right) = 0 \tag{B.9}$$

Solving by variable separation,

$$\psi(r,\theta) = \left(\frac{C_1}{r} + C_2 r^2\right)\sin^2\theta \tag{B.10}$$

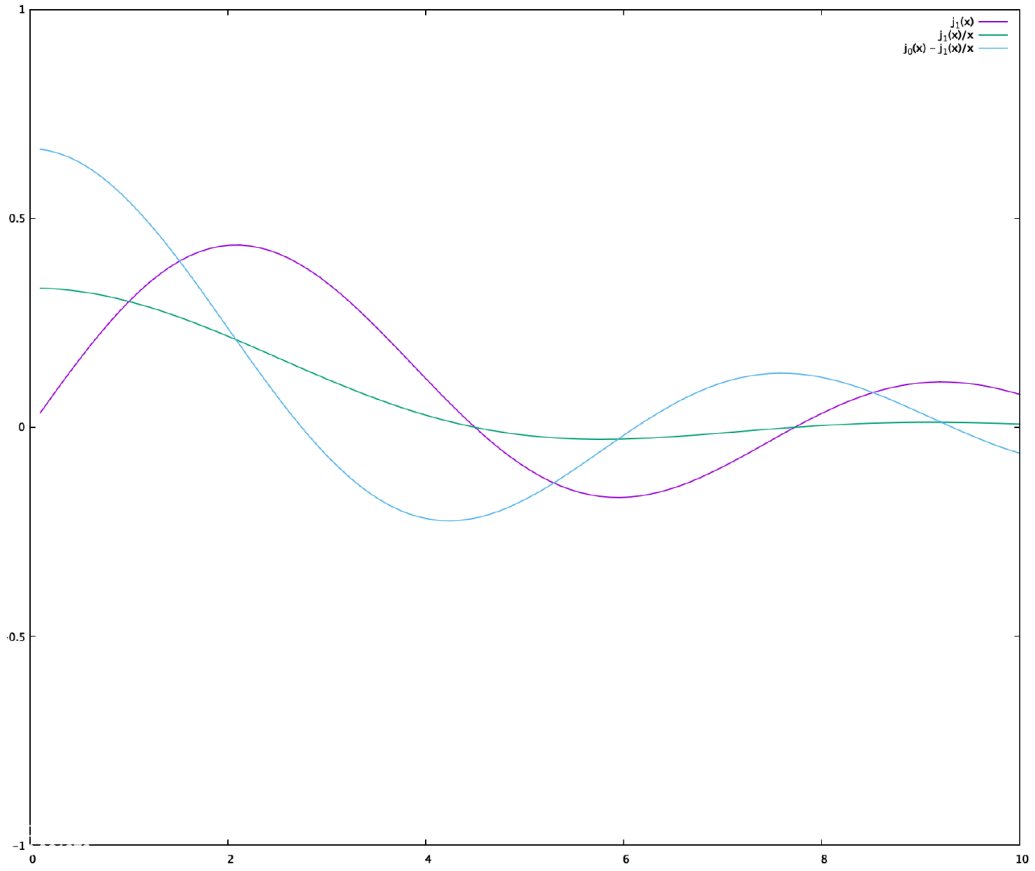

Figure B.2. Plots depicting B_r (green curve), B_θ (blue curve), and B_ϕ (purple curve) varying as $[\mathrm{j}_1(x)/x], [\mathrm{j}_0(x) - (\mathrm{j}_1(x)/x)]$, and $[\mathrm{j}_1(x)]$, respectively. Here, $x \equiv \lambda r$.

where, C_1 and C_2 are constants which set the dimensions of ψ and will be determined through boundary conditions.

Using B.2 and B.10, and imposing the boundary condition that at $r = r_0$, $B_\phi = \lambda\psi = 0$ and approximating the magnetic field at very large distances as a uniform field $B_0\hat{z}$, external magnetic field in the presence of spheromak is

$$\boldsymbol{B}_{\mathbf{ex}} = \left(B_0\cos\theta - B_0\cos\theta\frac{r_0^3}{r^3}, -B_0\sin\theta - B_0\sin\theta\frac{r_0^3}{2r^3}, 0\right) \tag{B.11}$$

Magnetic field at the surface of the spheromak is continuous. Hence, the constant A_0 in B.7 can be related to the constant magnetic field B_0 as

$$A_0\lambda^2 = \frac{3B_0}{2\mathrm{j_1}'(\lambda r_0)} \approx -6.9B_0$$

or,

$$A_0 \approx -0.342B_0 r_0^2 \tag{B.12}$$

Furthermore, we approximate the spheromak as a magnetic dipole embedded in an external dipole magnetic field and analyze its stability against tilt by deriving a vector equation for its magnetic moment. Since the external magnetic field is a superposition of the uniform magnetic field $B_0\hat{z}$ at large distances and the magnetic field of spheromak (a magnetic dipole) such that $\boldsymbol{B}_{\mathrm{sp}} = \boldsymbol{B}_{\mathbf{ex}} - B_0\hat{z}$, the dipole moment of spheromak can be determined. From B.11,

$$\boldsymbol{B}_{\mathrm{sp}} = \left(-B_0\frac{{r_0}^3}{r^3}\cos\theta, -B_0\frac{{r_0}^3}{2r^3}\sin\theta, 0\right) \tag{B.13}$$

Comparing B.13 with the dipole magnetic field with dipole moment $\boldsymbol{\mu}$ in spherical coordinates,

$$\boldsymbol{B}_{\mathrm{d}} = \left(\frac{2\mu_0\mu}{r^3}\cos\theta, \frac{\mu_0\mu}{r^3}\sin\theta, 0\right) \tag{B.14}$$

gives the magnetic moment of the spheromak

$$\boldsymbol{\mu} = \frac{-B_0 r_0^3}{2}(\cos\theta\hat{r} - \sin\theta\hat{\theta}) \tag{B.15}$$

or equivalently in Cartesian coordinates

$$\boldsymbol{\mu} = \frac{-B_0 r_0^3}{2}\hat{z} \tag{B.16}$$

in code units.

Equation B.16 shows that the spheromak is anti-aligned with the external magnetic field $B_0\hat{z}$ and hence subject to tilt.

REFERENCES

[1] G. Taylor and J. Granot, "Review article: THE GIANT FLARE FROM SGR 1806-20 AND ITS RADIO AFTERGLOW," *Modern Physics Letters A*, vol. 21, pp. 2171–2188, 2006.

[2] P. Woods and C. Thompson, "Soft Gamma Repeaters and Anomalous X-ray Pulsars: Magnetar Candidates," in *Compact Stellar X-ray Sources*, W. Lewin and M. Klis, Eds., Cambridge, UK: Cambridge University Press, 2006, pp. 547–586.

[3] S. Mereghetti, "Review article: The strongest cosmic magnets: Soft gamma-ray repeaters and anomalous X-ray pulsars," *Astron. Astrophys. Rev*, vol. 15, pp. 225–287, 2008.

[4] R. Turolla, S. Zane, and A. L. Watts, "Review article: Magnetars: The physics behind observations. A review," *Rep. Prog. Phys.*, vol. 78, p. 116 901, 2015.

[5] V. Kaspi and A. Beloborodov, "Magnetars," *Annual Review of Astronomy and Astrophysics*, vol. 55, pp. 261–301, 2017.

[6] R. Duncan and C. Thompson, "FORMATION OF VERY STRONGLY MAGNETIZED NEUTRON STARS: IMPLICATIONS FOR GAMMA-RAY BURSTS," *The Astrophysical Journal*, vol. 392, pp. L9–L13, 1992.

[7] C. Thompson and R. Duncan, "The soft gamma repeaters as very strongly magnetized neutron stars - I. Radiative mechanism for outbursts," *Monthly Notices of the Royal Astronomical Society*, vol. 275, pp. 255–300, 1995.

[8] C. Thompson and R. C. Duncan, "THE SOFT GAMMA REPEATERS AS VERY STRONGLY MAGNETIZED NEUTRON STARS. II. QUIESCENT NEUTRINO, X-RAY, AND ALFVÉN WAVE EMISSION," *The Astrophysical Journal*, vol. 473, pp. 322–342, 1996.

[9] D. M. Palmer, S. Barthelmy, N. Gehrels, R. M. Kippen, T. Cayton, C. Kouveliotou, D. Eichler, R. A. M. J. Wijers, P. M. Woods, J. Granot, Y. E. Lyubarsky, E. Ramirez-Ruiz, L. Barbier, M. Chester, J. Cummings, E. E. Fenimore, M. H. Finger, B. M. Gaensler, D. Hullinger, H. Krimm, C. B. Markwardt, J. A. Nousek, A. Parsons, S. Patel, T. Sakamoto, G. Sato, M. Suzuki, and J. Tueller, "A giant γ-ray flare from the magnetar SGR 1806 - 20," *Nature*, vol. 434, no. 7037, pp. 1107–1109, 2005.

[10] S. Mereghetti, D. Götz, A. von Kienlin, A. Rau, G. Lichti, G. Weidenspointner, and P. Jean, "THE FIRST GIANT FLARE FROM SGR 1806 - 20: OBSERVATIONS USING THE ANTICOINCIDENCE SHIELD OF THE SPECTROMETER ON *INTEGRAL*," *The Astrophysical Journal*, vol. 624, pp. L105–L108, 2005.

[11] G. L. Israel and et al., "THE DISCOVERY OF RAPID X-RAY OSCILLATIONS IN THE TAIL OF THE SGR 1806-20 HYPERFLARE," *The Astrophysical Journal*, vol. 628, pp. L53–L56, 2005.

[12] K. Hurley, S. E. Boggs, D. M. Smith, R. C. Duncan, R. Lin, A. Zoglauer, S. Krucker, G. Hurford, H. Hudson, C. Wigger, W. Hajdas, C. Thompson, I. Mitrofanov, A. Sanin, W. Boynton, C. Fellows, A. von Kienlin, G. Lichti, A. Rau, and T. Cline, "An exceptionally bright flare from SGR 1806-20 and the origins of short-duration γ-ray bursts," *Nature*, vol. 434, pp. 1098–1103, 2005.

[13] C. Thompson and R. Duncan, "THE GIANT FLARE OF 1998 AUGUST 27 FROM SGR 1900+14. II. RADIATIVE MECHANISM AND PHYSICAL CONSTRAINTS ON THE SOURCE," *The Astrophysical Journal*, vol. 561, pp. 980–1005, 2001.

[14] B. Link and C. A. van Eysden, "TORSIONAL OSCILLATIONS OF A MAGNETAR WITH A TANGLED MAGNETIC FIELD," *The Astrophysical Journal Letters*, vol. 823, no. 1, p. L1, 2016.

[15] P. B. Cameron, P. Chandra, A. Ray, S. R. Kulkarni, D. A. Frail, M. H. Wieringa, E. Nakar, E. S. Phinney, A. Miyazaki, M. Tsuboi, S. Okumura, N. Kawai, K. M. Menten, and F. Bertoldi, "Detection of a radio counterpart to the 27 December 2004 giant flare from SGR 1806 - 20," *Nature*, vol. 434, pp. 1112–1115, 2005.

[16] B. M. Gaensler, C. Kouveliotou, J. D. Gelfand, G. B. Taylor, D. Eichler, R. A. M. J. Wijers, J. Granot, E. Ramirez-Ruiz, Y. E. Lyubarsky, R. W. Hunstead, D. Campbell-Wilson, A. J. van der Horst, M. A. McLaughlin, R. P. Fender, M. A. Garrett, K. J. Newton-McGee, D. M. Palmer, N. Gehrels, and P. M. Woods, "An expanding radio nebula produced by a giant flare from the magnetar SGR 1806-20," *Nature*, vol. 434, pp. 1104–1106, 2005.

[17] J. D. Gelfand, "The radio nebula produced by the 27 December 2004 giant flare from SGR 1806-20," *Astrophys Space Sci*, vol. 308, pp. 39–42, 2007.

[18] J. D. Gelfand, Y. E. Lyubarsky, D. Eichler, B. M. Gaensler, G. B. Taylor, J. Granot, K. J. Newton-McGee, E. Ramirez-Ruiz, C. Kouveliotou, and R. A. M. J. Wijers, "A Rebrightening of the Radio Nebula Associated with the 2004 December 27 Giant Flare from SGR 1806-20," *The Astrophysical Journal*, vol. 634, pp. L89–L92, 2005.

[19] J. Granot, E. Ramirez-Ruiz, G. B. Taylor, D. Eichler, Y. E. Lyubarsky, R. A. M. J. Wijers, B. M. Gaensler, J. D. Gelfand, and C. Kouveliotou, "Diagnosing the Outflow from the SGR 1806-20 Giant Flare with Radio Observations," *The Astrophysical Journal*, vol. 638, pp. 391–396, 2006.

[20] C. Thompson and R. C. Duncan, "The soft gamma repeaters as very strongly magnetized neutron stars - I. Radiative mechanism for outbursts," *Monthly Notices of the Royal Astronomical Society*, vol. 275, pp. 255–300, 1995. DOI: 10.1093/mnras/275.2.255.

[21] G. B. Taylor, J. D. Gelfand, B. M. Gaensler, J. Granot, C. Kouveliotou, R. P. Fender, E. Ramirez-Ruiz, D. Eichler, Y. E. Lyubarsky, M. Garrett, and R. A. M. J. Wijers, "The Growth, Polarization, and Motion of the Radio Afterglow from the Giant Flare from SGR 1806-20," *The Astrophysical Journal*, vol. 634, pp. L93–L96, 2005. DOI: 10.1086/491648. arXiv: astro-ph/0504363 [astro-ph].

[22] M. Lyutikov, "The electromagnetic model of gamma-ray bursts," *New Journal of Physics*, vol. 8, p. 119, 2006.

[23] M. Lyutikov, "Magnetar activity mediated by plastic deformations of neutron star crust," *Monthly Notices of the Royal Astronomical Society*, vol. 447, pp. 1407–1417, 2015. DOI: 10.1093/mnras/stu2413. arXiv: 1407.5881 [astro-ph.HE].

[24] Y. Levin and M. Lyutikov, "On the dynamics of mechanical failures in magnetized neutron star crusts," *Monthly Notices of the Royal Astronomical Society*, vol. 427, pp. 1574–1579, 2012. DOI: 10.1111/j.1365-2966.2012.22016.x. arXiv: 1204.2605 [astro-ph.HE].

[25] B. Paczynski, "Gamma-ray bursters at cosmological distances," *The Astrophysical Journal*, vol. 308, pp. L43–L46, 1986. DOI: 10.1086/184740.

[26] M. Lyutikov and K. Gourgouliatos, "Coronal mass ejections as expanding force-free structures," *Solar Physics*, vol. 270, no. 2, pp. 537–549, 2011.

[27] M. V. Barkov, M. Lyutikov, and D. Khangulyan, "3D dynamics and morphology of bow-shock pulsar wind nebulae," *Monthly Notices of the Royal Astronomical Society*, vol. 484, pp. 4760–4784, 2019. DOI: 10.1093/mnras/stz213. arXiv: 1804.07327 [astro-ph.HE].

[28] P. Bellan, *Magnetic Helicity, Spheromaks, Solar Corona Loops, and Astrophysical Jets.* California Institute of Technology: World Scientific Publishing Europe Ltd, 2018.

[29] K. Gourgouliatos, J. Braithwaite, and M. Lyutikov, "Structure of magnetic fields in intracluster cavities," *Monthly Notices of the Royal Astronomical Society*, vol. 409, no. 4, pp. 1660–1668, 2010.

[30] A. Mignone, G. Bodo, S. Massaglia, T. Matsakos, O. Tesileanu, C. Zanni, and A. Ferrari, "PLUTO: A NUMERICAL CODE FOR COMPUTATIONAL ASTROPHYSICS," *The Astrophysical Journal Supplement Series*, vol. 170, pp. 228–242, 2007.

[31] T. Miyoshi and K. Kusano, "A multi-state HLL approximate Riemann solver for ideal magnetohydrodynamics," *Journal of Computational Physics*, vol. 208, no. 1, pp. 315–344, 2005. DOI: 10.1016/j.jcp.2005.02.017.

[32] Y. B. Zel'dovich and Y. P. Raizer, *Physics of Shock Waves and High Temperature Hydrodynamic Phenomena Volume II*. New York and London: Academic Press, 1967.

[33] G. B. Whitham, *Linear and Nonlinear Waves*. John Wiley and Sons, Inc, 1974.

[34] L. I. Sedov, *Similarity and Dimensional Methods in Mechanics,* Academic Press, New York, Sedov, L. I., Ed. 1959, p. 244.

[35] A. S. Kompaneets, "A Point Explosion in an Inhomogeneous Atmosphere," *Soviet Physics Doklady*, vol. 5, pp. 46–+, 1960.

[36] H. J. Melosh, *Impact cratering : a geologic process*. 1989.

[37] F. H. Shu, *The Physics of Astrophysics Volume II Gas Dynamics*. Mill Valley, California: University Science Books, 1992.

[38] R. A. Chevalier, "The radio and X-ray emission from type II supernovae.," *The Astrophysical Journal*, vol. 259, pp. 302–310, 1982. DOI: 10.1086/160167.

[39] R. A. Chevalier, "The Circumstellar Interaction Model for Radio Supernovae," in *Radio Emission from the Stars and the Sun*, A. R. Taylor and J. M. Paredes, Eds., ser. Astronomical Society of the Pacific Conference Series, vol. 93, 1996, p. 125.

[40] S. P. Reynolds, "Dynamical Evolution and Radiative Processes of Supernova Remnants," in *Handbook of Supernovae*, A. W. Alsabti and P. Murdin, Eds., Cham: Springer International Publishing, 2017, pp. 1981–2004.

[41] S. P. Reynolds and R. A. Chevalier, "Nonthermal radiation from supernova remnants in the adiabatic stage of evolution.," *The Astrophysical Journal*, vol. 245, pp. 912–919, 1981. DOI: 10.1086/158868.

[42] N. Duric and E. R. Seaquist, "A Theoretical Interpretation of the Sigma –D Relation for Supernova Remnants," *The Astrophysical Journal*, vol. 301, p. 308, 1986. DOI: 10.1086/163900.

[43] Z. P. Huang, T. X. Thuan, R. A. Chevalier, J. J. Condon, and Q. F. Yin, "Compact Radio Sources in the Starburst Galaxy M82 and the Sigma -D Relation for Supernova Remnants," *The Astrophysical Journal*, vol. 424, p. 114, 1994. DOI: 10.1086/173876.

[44] S. F. Gull, "A numerical model of the structure and evolution of young supernovaremnants," *Monthly Notices of the Royal Astronomical Society*, vol. 161, pp. 47–69, 1973. DOI: 10.1093/mnras/161.1.47.

[45] V. N. Fedorenko, "Particle acceleration and radio emission of the supernovae remnants at different stages of their evolution.," in *Supernova Remnants and their X-ray Emission*, J. Danziger and P. Gorenstein, Eds., vol. 101, 1983, pp. 183–186.

[46] S. G. Lucek and A. R. Bell, "Non-linear amplification of a magnetic field driven by cosmic ray streaming," *Monthly Notices of the Royal Astronomical Society*, vol. 314, no. 1, pp. 65–74, 2000. DOI: 10.1046/j.1365-8711.2000.03363.x.

[47] E. G. Berezhko, L. T. Ksenofontov, and H. J. Völk, "Emission of SN 1006 produced by accelerated cosmic rays," *AA*, vol. 395, pp. 943–953, 2002. DOI: 10.1051/0004-6361:20021219. arXiv: astro-ph/0204085 [astro-ph].

[48] E. G. Berezhko and H. J. Völk, "Direct evidence of efficient cosmic ray acceleration and magnetic field amplification in Cassiopeia A," *AA*, vol. 419, pp. L27–L30, 2004. DOI: 10.1051/0004-6361:20040130. arXiv: astro-ph/0404203 [astro-ph].

[49] H. J. Völk, E. G. Berezhko, and L. T. Ksenofontov, "Magnetic field amplification in Tycho and other shell-type supernova remnants," *AA*, vol. 433, no. 1, pp. 229–240, 2005. DOI: 10.1051/0004-6361:20042015. arXiv: astro-ph/0409453 [astro-ph].

[50] A. R. Bell and S. G. Lucek, "Cosmic ray acceleration to very high energy through the non-linear amplification by cosmic rays of the seed magnetic field," *Monthly Notices of the Royal Astronomical Society*, vol. 321, no. 3, pp. 433–438, 2001. DOI: 10.1046/j.1365-8711.2001.04063.x.

[51] E. N. Vinyajkin, "On the Evolution of Radio Emission of the Tycho Brahe's Supernova Remnant (3C10)," *Odessa Astronomical Publications*, vol. 12, p. 148, 1999.

[52] E. N. Vinyaikin, "Frequency dependence of the evolution of the radio emission of the supernova remnant Cas A," *Astronomy Reports*, vol. 58, no. 9, pp. 626–639, 2014. DOI: 10.1134/S1063772914090078.

[53] K. S. Stankevich, A. M. Aslanyan, V. P. Ivanov, R. M. Martirosyan, and Y. Terzian, "Evolution of the Radio Luminosities of the Tycho and Kepler Supernovae Remnants," *Astrophysics*, vol. 46, no. 4, pp. 429–433, 2003. DOI: 10.1023/B:ASYS.0000003258.04439.f3.

[54] K. W. Weiler, N. Panagia, R. A. Sramek, S. D. Van Dyk, C. J. Stockdale, and C. L. Williams, "Radio emission from supernovae.," *Mem. Soc. Astron. Italiana*, vol. 81, p. 374, 2010.

[55] C. F. Kennel and F. V. Coroniti, "Magnetohydrodynamic model of Crab nebula radiation," *The Astrophysical Journal*, vol. 283, pp. 710–730, 1984. DOI: 10.1086/162357.

[56] A. M. Atoyan, "Radio spectrum of the Crab nebula as an evidence for fast initial spin of its pulsar," *AA*, vol. 346, pp. L49–L52, 1999. eprint: astro-ph/9905204.

[57] L. Woltjer, "A THEOREM ON FORCE-FREE MAGNETIC FIELDS," *Proceedings of the National Academy of Sciences*, vol. 44, pp. 489–491, 1958.

[58] J. Taylor, "Relaxation of toroidal plasma and generation of reverse magnetic fields," *Phys. Rev. Lett.*, vol. 33, pp. 1139–1141, 1974.

[59] E. Priest and T. Forbes, *Magnetic Reconnection.* Cambridge, UK: Cambridge University Press, 2000.

[60] B. Gaensler and P. Slane, "The Evolution and Structure of Pulsar Wind Nebulae," *Annual Review of Astronomy and Astrophysics*, vol. 44, pp. 17–47, 2006.

[61] S. Chandrasekhar and P. Kendall, "On force-free magnetic fields," *The Astrophysical Journal*, vol. 126, p. 457, 1957.

[62] S. Lundquist, "On the stability of magneto-hydrostatic fields," *Phys. Rev.*, vol. 83, pp. 307–311, 1951.

[63] B. Kadomtsev, "Review article: Magnetic field line reconnection," *Reports on Progress in Physics*, vol. 50, no. 2, pp. 115–143, 1987.

[64] M. Rosenbluth and M. Bussac, "MHD stability of Spheromak," *Nuclear Fusion*, vol. 19, no. 4, pp. 489–498, 1979.

[65] P. Bellan, *Spheromaks: A Practical Application of Magnetohydrodynamic Dynamos and Plasma Self-Organization.* California Institute of Technology: Imperial College Press, 2000.

[66] Y. Masada, S. Nagataki, K. Shibata, and T. Terasawa, "Solar-Type Magnetic Reconnection Model for Magnetar Giant Flares," *Publications of the Astronomical Society of Japan*, vol. 62, pp. 1093–1102, 2010.

[67] M. Lyutikov, "Explosive reconnection in magnetars," *Monthly Notices of the Royal Astronomical Society*, vol. 346, pp. 540–554, 2003.

[68] S. Komissarov, M. Barkov, and M. Lyutikov, "Tearing instability in relativistic magnetically dominated plasmas," *Monthly Notices of the Royal Astronomical Society*, vol. 374, pp. 415–426, 2006.

[69] K. Ivanov and A. Harshiladze, "Interplanetary hydromagnetic clouds as flare-generated spheromaks," *Solar Physics*, vol. 98, pp. 379–386, 1985.

[70] A. Mastrano and A. Melatos, "Non-ideal evolution of non-axisymmetric, force-free magnetic fields in a magnetar," *Monthly Notices of the Royal Astronomical Society*, vol. 387, no. 4, pp. 1735–1744, 2008.

[71] T. Sato and T. Hayashi, "Three-Dimensional Simulation of Spheromak Creation and Tilting Disruption," *Physical Review Letters*, vol. 50, pp. 38–40, 1983.

[72] E. V. Belova, S. C. Jardin, H. Ji, M. Yamada, and R. Kulsrud, "Numerical study of tilt stability of prolate field-reversed configurations," *Physics of Plasmas*, vol. 7, pp. 4996–5006, 2000.

[73] E. V. Belova, R. C. Davidson, H. Ji, and M. Yamada, "Advances in the numerical modeling of field-reversed configurations," *Physics of Plasmas*, vol. 13, p. 056 115, 2006.

[74] A. Bondeson, G. Marklin, Z. G. An, H. H. Chen, Y. C. Lee, and C. S. Liu, "Tilting instability of a cylindrical spheromak," *The Physics of Fluids*, vol. 24, pp. 1682–1688, 1981.

[75] J. M. Finn, W. M. Manheimer, and E. Ott, "Spheromak tilting instability in cylindrical geometry," *The Physics of Fluids*, vol. 24, pp. 1336–1341, 1981.

[76] E. V. Belova, S. C. Jardin, H. Ji, M. Yamada, and R. Kulsrud, "Numerical study of global stability of oblate field-reversed configurations," *Physics of Plasmas*, vol. 8, pp. 1267–1277, 2001.

[77] T. Jarboe, "Review of spheromak research," *Plasma Phys. Control. Fusion*, vol. 36, pp. 945–990, 1994.

[78] B. Ripperda, O. Porth, C. Xia, and R. Keppens, "Reconnection and particle acceleration in interacting flux ropes – i. Magnetohydrodynamics and test particles in 2.5D," *Monthly Notices of the Royal Astronomical Society*, vol. 467, pp. 3279–3298, 2017.

[79] V. Shafranov, "Plasma equilibrium in a magnetic field," *Reviews of Plasma Physics*, vol. 2, p. 103, 1966.

[80] H. Grad, "Toroidal containment of a plasma," *Physics of Fluids*, vol. 10, no. 1, pp. 137–154, 1967.

[81] K. Tsui, "Toroidal equilibria in spherical coordinates.," *Physics of Plasmas*, vol. 15, no. 11, pp. 112 506–1 125 067, 2008.

[82] S. Jardin, "The Spheromak," *Europhysics News*, vol. 17, pp. 73–76, 1986.

[83] O. Buneman, "TRISTAN," *In: Matsumoto H., and Omura Y. (eds.): Computer Space Plasma Physics: Simulation Techniques and Software. Terra Scientific, Tokyo*, pp. 67–84, 1993.

[84] A. Spitkovsky, "Simulations of relativistic collisionless shocks: Shock structure and particle acceleration," *AIP Conference Proceedings*, vol. 801, p. 345, 2005.

[85] C. Munson, A. Janos, F. Wysocki, and M. Yamada, "Experimental control of the spheromak tilting instability," *The Physics of Fluids*, vol. 28, pp. 1525–1527, 1985.

[86] M. Gedalin, "Linear waves in relativistic anisotropic magnetohydrodynamics," *Physical review. E, Statistical physics, plasmas, fluids, and related interdisciplinary topics*, vol. 47, no. 6, pp. 4354–4357, Jul. 1993.

[87] P. Bellan, *Fundamentals of Plasma Physics.* Cambridge, UK: Cambridge University Press, 2006.

[88] A. Reiman, "Coalescence of spheromaks," *The Physics of Fluids*, vol. 25, pp. 1885–1893, 1982.

[89] A. Mohri, "Spinning plasma ring stable to tilting mode," *Japanese Journal of Applied Physics*, vol. 19, pp. L686–L688, 1980.

[90] A. Ishida, H. Momota, and L. C. Steinhauer, "Variational formulation for a multifluid flowing plasma with application to the internal tilt mode of a field-reversed configuration," *The Physics of Fluids*, vol. 31, p. 3024, 1988.

[91] H. Ji, M. Yamada, R. Kulsrud, N. Pomphrey, and H. Himuraa, "Studies of global stability of field-reversed configuration plasmas using a rigid body model," *Physics of Plasmas*, vol. 5, pp. 3685–3693, 1998.

VITA

EDUCATION

1. **Purdue University** West Lafayette, IN, USA

- **Ph.D., Physics and Astronomy** *Expected Graduation: May 2021*

  Dissertation: *An investigation of the mechanisms behind magnetars' high-energy and radio emissions through magnetohydrodynamic simulations*: The purpose of my research is to gain a theoretical understanding of the physical mechanisms that cause some of the most energetic emissions in the universe, namely, giant flares from magnetars. As a graduate research assistant, I accomplish this through building analytical models and running high resolution simulations in C using the *PLUTO* code to predict and reproduce astrophysical observations as closely as possible.

  Advisor: Dr. Maxim Lyutikov

- **M.Sc., Physics and Astronomy** *May 2017*

2. **The Maharaja Sayajirao University of Baroda** Gujarat, India

- **B.E., Electronics and Communication** *April 2014*

  Final Year Project: *Cortex M3 and TFT LCD SCREEN based Wireless Ordering Kiosk*: The purpose of this project was to introduce a wireless-based ordering system for restaurants using a TFT (thin film transistor) LCD screen interfaced with a CORTEX M3 processor, wherein customers would be able to order via their android-based smartphone as soon as they get connected with the hotel WiFi network.

RESEARCH EXPERIENCE — Purdue University

Graduate Research Assistant — January 2019 – Present

- Presented a poster titled "Tilting instability of magnetically confined spheromaks" in the Physics and Astronomy Department's Annual Poster Presentation, November 2018, 2019
- Participated in the Midwest Workshop on Supernovae and Transients at Ohio State University to meet collaborators and receive feedback to integrate in my research, September 2019
- Participated in the Workshop on Relativistic Plasma Astrophysics, Department of Physics and Astronomy, Purdue University to acquire training and meet collaborators in my research field, May 2018
- Conducted supervised observations of galaxies to collect their spectral information over two nights at the Kitt Peak National Observatory, Tucson AZ, as part of a winter research course, December 2016
- Led and participated in discussions on latest research articles in the weekly Astrophysics Journal Club of the department

RESEARCH AREAS AND INTERESTS

My research experience and interests are in the application of plasma physics in astrophysical settings, in particular, studying astrophysical shocks and magnetically confined spheromaks. I am also interested in exploring the physical mechanisms behind high-energy and radio emissions from one class of rotating neutron stars called magnetars, in particular, those associated with their giant flares, using the astrophysical code *PLUTO*.

1. ***Plasma Physics***

   I apply fundamentals of plasma physics to study magnetically confined equilibrium structures called spheromaks, particularly their tilting instabilities. I analyze their

instability and dissipation timescales to explain the origin of quasi-periodic oscillations seen in magnetar giant flares (see publication [2]).

2. ***High Energy Theoretical Astrophysics***

   I study high-energy, namely X-ray and γ-ray emissions and radio emissions from one class of rotating neutron stars called magnetars possessing extreme surface magnetic fields. In particular, I am interested in analyzing magnetar giant flares and their afterglow radio emissions. I build analytical models to hypothesize physical mechanisms causing these emissions and simulate them in a three-dimensional high-resolution grid to reproduce astrophysical observations using the astrophysical code called *PLUTO* written entirely in the C programming language.

TEACHING EXPERIENCE — Purdue University

Graduate Teaching Assistant — August 2015 – December 2018

1. **Undergraduate courses taught:**

   - ***Modern Mechanics PHYS 172****: Introductory calculus-based physics course to explain Newtonian Mechanics*

     Taught laboratory to a class of 40+ students, held help center hours, used simple equipment to explicate Newtonian concepts which can otherwise be difficult to visualize, employed 3-D graphical simulations and numerical problem solving by computer using software like vPython to facilitate visual learning

   - ***Electric And Magnetic Interactions PHYS 272 and PHYS 272 Honors****: Calculus-based physics course to explain Electrostatics and Magnetostatics - continuation of PHYS 172*

     Taught laboratory and recitations to a class of 25+ students, held help center hours, used simple equipment interfaced with PASCO capstone to explicate electric and magnetic interactions which can otherwise be difficult to visualize, employed 3-D graphical simulations and numerical problem solving by computer using software like vPython and Matlab to facilitate visual learning

- ***Descriptive Astronomy: The Solar System ASTR 263***
  Descriptive Astronomy: Stars and Galaxies ASTR 264:
  Descriptive courses in astronomy focussing on topics about the solar system, stars and galaxies intended for non-physics majors
  Taught laboratory to a class of 25+ students, designed examinations, held office hours, used simple props and scientific equipment to explicate basic concepts of astronomy, utilized interactive software like Starry Night, Stellarium and CLEA to quantify astrophysical concepts and enable visualization of movement of astronomical objects, organized trips to nearby dark sites and observatories and operated telescopes for students to observe the Sun, constellations, planets, galaxies and nebula, employed SKYNET to remotely capture images of different parts of an astronomical object to be later synthesized into a mosaic image

2. **Positions of responsibility:**

- ***Head Teaching Assistant/Coordinator for PHYS 272 and PHYS 272H***, August 2017 - December 2018:
  Singularly responsible for making laboratory and recitation content available online on Blackboard, developed new laboratory manuals and updated existing ones, organized weekly meetings with course instructor and teaching assistants, mentored graduate and undergraduate teaching assistants, designed and improved course examinations along with the course instructor, resolved issues with laboratory equipment, and procured a grant of $8430 under ***Instructional Equipment for a New Laboratory*** to purchase new equipment for laboratory, November 2017
- ***Lecturer for PHYS 272***, June - July 2018:
  Singularly responsible for making lecture, laboratory and recitation content available online on Blackboard, structuring and teaching course content supplemented with live demonstrations to a class of 30 students, coordinating laboratory and recitations, conducting examinations, and providing end-of-semester grades

- ***Substitute Lecturer for PHYS 272***, August 2018:
  Delivered two lectures on course content to a class of 200+ students
- ***Head Teaching Assistant/Coordinator for ASTR 263 and 264***, August 2016 - May 2017:
  Singularly responsible for making laboratory content available online on Blackboard, developed new lab manuals and updated existing ones to reflect up-to-date laboratory methods, resolved issues with laboratory equipment, organized weekly meetings with teaching assistants and trained them in telescope use along with the course instructor, designed laboratory exams, and provided end-of-semester grades for laboratory

ACADEMIC SERVICE

Served in the Physics Graduate Student Association (PGSA) of the Physics and Astronomy Department at Purdue University as:

1. ***Teaching and Professional Development Chair***, May 2020 - present
   - Acted as a point of contact for any PGSA member or Physics faculty member regarding issues related to PGSA members as teaching assistants or professional development
2. ***President***, May 2018 - April 2020
   - Acted as a liaison between graduate students and department administration to voice student concerns
   - Applied for and received a grant of $1500 from the ***Graduate Student Organization Grant Allocation*** for running various PGSA activities
   - Organized a ***PGSA fundraiser*** and raised $1000 in collaboration with the undergraduate Society of Physics Students (SPS)
   - Organized a free-to-all astronomy observing night at the local Cumberland Elementary School of West Lafayette, IN

- Co-organized various social and cultural events in collaboration with SPS and the Electrical Engineering Department
- Organized ***Adopt-A-Road***, a road clean-up event as part of PGSA's community service

3. ***Treasurer***, May 2017 - April 2018

- Kept track of all income and expenses of the PGSA
- Kept accounts, deposited the organization's funds, and made expenditures in a manner approved by Purdue's Business Office for Student Organizations
- Approved and sanctioned financial expenditures in consultation with the President

OUTREACH, COMMUNITY AND EXTRA-CURRICULAR ACTIVITIES

- Volunteered for Purdue NanoDays designed for K-12 students, Girl Scouts, teachers and parents
- Volunteered for Saturday Morning Astrophysics offered by Purdue University ***Physics and Astronomy Outreach*** designed for high school and upper level middle school students
- Headed and co-organized public-speaking and adventure events over two years as part of Paramarsh - a non-technical festival of The Maharaja Sayajirao University of Baroda, Gujarat, India

AWARDS, HONORS AND CERTIFICATES

- Received certificate with ***Excellent*** performance from Centre for Continuing Education, IIT Kanpur, India on completion of a 4-month online course on Classical Electromagnetism - 1 (Electrostatics), December 2020

- Publication **Mehta, R.,** et al. 2020. "Tilting instability of magnetically confined spheromaks" selected as one of the ***Featured Articles*** by Journal of Plasma Physics, November 2020

- Received ***Graduate Teacher Certificate*** from Purdue's Center for Instructional Excellence in the 19th Annual Celebration of Graduate Student Teaching Excellence on completion of assigned teaching and professional development activities, April 2017

- Awarded ***four gold medals*** at the Annual Convocation of The Maharaja Sayajirao University of Baroda, Gujarat, India on completion of Bachelor of Engineering degree, April 2014

TECHNICAL SKILLS

- **Software**: Latex, Word, Powerpoint, Excel, Pages, Keynote, Numbers

- **Communication software**: Skype, Zoom, WebEx, Google Meet

- **Course-specific software**: Blackboard Learn, PASCO capstone, Stellarium, Starry Night, CLEA, SKYNET

- **Operating systems**: Linux, Windows, iOS

- **Languages**: Python, C, PLUTO

- **Libraries**: pandas, SciPy, NumPy, Matplotlib

PUBLICATIONS

[1] **Mehta, R., Barkov, M., & Lyutikov, M.** "Radio afterglow of magnetars' giant flares". - *in preparation, to be submitted to the Monthly Notices of the Royal Astronomical Society.*

[2] **Mehta, R., Barkov, M., Sironi, L., & Lyutikov, M. (2020).** "Tilting instability of magnetically confined spheromaks". *Journal of Plasma Physics, 86(4), 905860407. DOI: 10.1017/S0022377820000768*